Doctoral Dissertation

Plasma etching mechanisms
in the fabrication of high-aspect-ratio microstructures
in stacked layers of different materials

異種積層膜高アスペクト比微細構造
プラズマエッチング機構の解明

Taku Iwase

July 2019

Graduate School of Engineering,
Osaka University

Contents

1. Introduction

1.1 Background

The semiconductor device industry is a fast-growing fundamental industry; its market size in 2017 totaled approximately $420 billion [1]. At present, dry processing technologies are indispensable for its development. In fact, most steps in device fabrication use dry processing technologies based on plasma-enhanced or -assisted physicochemical reactions. This means that further research on plasma technologies is a driving force for further advancement and innovation [2].

Ten years ago, Abe et al. reviewed the development of plasma etching technologies for fabricating semiconductor devices [3]. Since then, much progress has been made in this research field. This review covers plasma etching technologies for conventional semiconductor fabrication involving high-aspect-ratio (HAR) contacts and reliable Cu/low-dielectric constant dielectrics (Cu/low-k) interconnects. It points out the demand for reduced plasma-induced damage and for more precise control of the critical dimensions (CDs) and etching feature profiles. The concerns about damage [4] and CD control [5,6] were recently extensively reviewed. To consider the wider capabilities of plasma processes, the historical background of dry processing is reviewed again here.

In particular, the period during which semiconductor manufacturing introduced plasma technology, including non-thermal processes such as reactive ion etching (RIE) and plasma-enhanced thin film deposition, witnessed epoch-making inventions and discoveries, equivalent to those that ushered in the nanotechnology era. Plasma-enhanced or -assisted physicochemical reactions are characterized by a lack of directional thermodynamic minima to reach the state of thermal equilibrium. Energetic particles, such as electrons, ions, radicals, neutrals, and photons, which are generated in the plasma state of precursor gases, assist the reactions independently of thermodynamic minima and thermal equilibrium states. Thus, one can call this “nonequilibrium dynamics.” The time evolution of the reaction behavior is nonlinear dynamics. The topics of ion-induced reactions and photochemistry are discussed in multidisciplinary scientific areas, requiring that in situ reactions be monitored and analyzed in real time using emerging analytical techniques.

1.2 Reactive ion etching

Dry etching evolved into an indispensable technique in semiconductor manufacturing for miniaturization, and the maturation of fast anisotropic dry etching techniques spawned the next wave of system miniaturization in a variety of commercial products [7]. At the dawn of the dry process age, many new technologies emerged in multidisciplinary approaches. Most importantly, plasma science and technology significantly contributed to the indispensable development of high-volume dry processing.

In the 1960s, the semiconductor industry emerged from the era of wet processing at minimum gate lengths of approximately 10 μm [8]. In the late 1960s, dry etching using photoresist strippers, i.e., "plasma ashing," began to appear in wafer fabrication lines [9]. In the mid 1970s, the industry moved to the large-scale integrated circuit (LSI) era. RIE techniques using directed ion beams of reactive plasmas with high-resolution and anisotropy emerged in processing [9]. In the early 1980s, advances in manufacturing technology dramatically increased manufacturing yield and factory efficiency, and thereafter quality became a major concern [8].

Advances in RIE emerged from using a combination of a chemical reaction and a physical action. Sputtering processing (and ion milling) began using a plasma of inert gases. Directed ions colliding more on the horizontal surface than on the sidewalls results in anisotropic etching in which the etching rate is higher in the vertical direction. The invention by Hosokawa et al. in 1973 of a technique using halogenated gases resulted in much high etch rates with a conventional sputtering apparatus (Fig. 1) [10,11]. Subsequently, these halogenated gas ions became known as "reactive ions."

The RIE mechanism has been widely studied. In 1979, Coburn and Winters reported that synergism of physically directed ions and chemically reactive species ("radicals") is the reason that the etching rate is substantially higher when reactive ions are used [12, 13]. They used ion beam experiments in which a halogenated silicon surface was bombarded with inert ions. They observed that the interaction of plasmas with surfaces is dominated by synergistic effects between the incident ions and radicals. Film growth is accelerated by the ions, providing adsorption sites for incoming radicals, and chemical etching is accelerated by incident ions when chemical etching products are removed from the surface by ion sputtering [14].

In addition to ions, the physical actions in chemical reactions have been considered. For instance, photolysis of organic molecules can be classified in terms of physical action. In 1968, Kumagawa et al. reported epitaxial Si growth with light irradiation from a mercury lamp [15]. They argued that precursors of $SiCl_4$ can be dissociated by ultraviolet light irradiation, reducing the activation energy for crystal growth. The dissociation was initially monitored by using spectroscopic analysis, such as infrared absorption [16]. Chemical reactions were assessed as thermal equilibrium reactions; today, nonequilibrium reactions are attracting research attention. Not only light but also electrons and ions had become the central focus of research on dry processing. Whenever dry processing is conducted, the synergism of physical collisions and chemical reactions must be kept in mind.

Ions can move with acceleration under electric fields. This property is useful for two purposes: (i) acceleration of bombardment energy and (ii) transport of reactants toward a desired place for reactions. Pressures determine the mean-free path lengths. Higher pressures result in shorter mean-free path lengths, creating gas-flow patterns with diffusion behaviors. Lower pressures result in greater length, and the group velocity is saturated by the thermal speed of atoms and molecules, instead of diffusion.

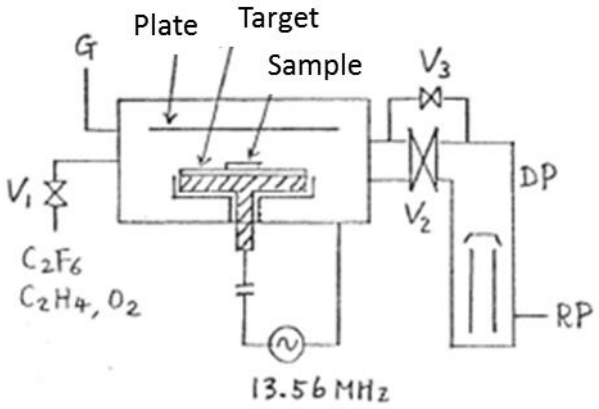

Fig. 1. First “reactive ion” sputtering, or etching, method as reported and patented [12]. G: gauge; V: valve; DP: diffusion pump; RP: rotary pump

1.2.1 Selected breakthroughs in RIE development

In the 1980s, high ion beam currents were required to obtain high etching rates, which created wafer temperature, mask deterioration, and by-product evacuation problems in industrial manufacturing. They were solved by the development of

electrostatic wafer chuck and turbo-molecular drag pump technologies.

Electrostatic chuck system is categorized as either (i) monopole or (ii) bipolar chucking. Briefly, a monopole system needs plasma for the chucking materials while a bipolar chucking (ii) system does not (Fig. 2). When a vacuum chamber shown in Fig. 2 is evacuated, the wafer cannot be transferred heat by simply placing it on the temperature-controlled stage. It must be chucked on the cooled stage prior to plasma ignition [17,18].

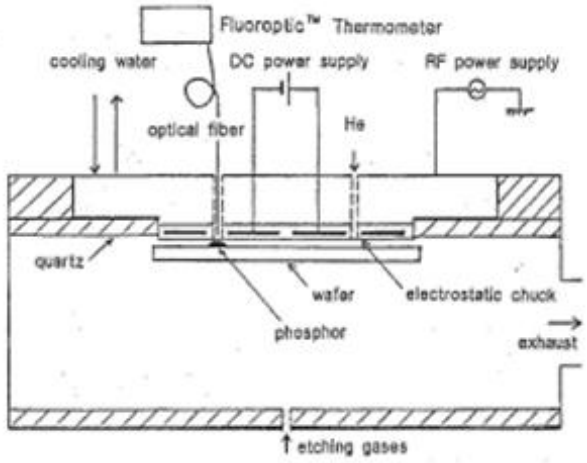

Fig. 2. Vacuum chamber with bipolar electrostatic wafer chuck system and wafer cooling system [18].

Another problem arose from the usage of halogen gases. Rotary oil pumps were still being used, and the oil used for lubricating them is degraded by the flow of halogen-containing gases. This problem was overcome by the interdisciplinary development of a turbo-molecular drag pump based on vacuum and aerospace technologies (Fig. 3). Its high pumping speed and low processing pressure enabled high-speed evacuation of halogenated by-products [19,20]. From the microscopic viewpoint of equipment-scale etching, precursor gases are introduced, and their gaseous reactions produce a variety of reactants, such as ions and radicals. These reactants are transported to the wafer surface, where synergistic reactions occur that form by-products. The by-products are also evacuated. These schemes have characteristic reaction time scales, meaning that the residence time of gases creating a reaction field in the chamber must be controlled. Tsujimoto et al. reported that high by-product evacuation speeds achieved high etching rates for poly-Si in Cl_2 plasma [21].

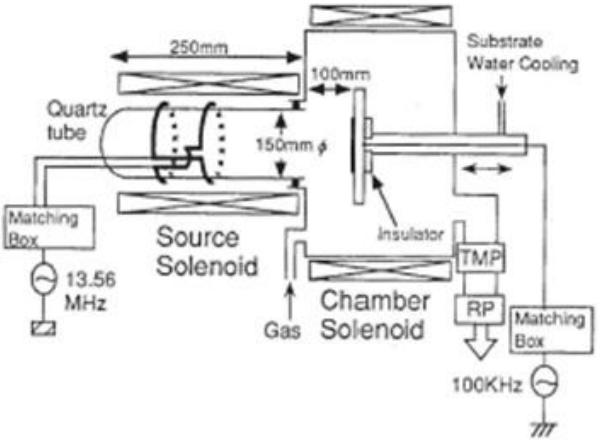

Fig. 3. Implementation of turbo-molecular drag pump (TMP) based on vacuum and aerospace technologies. RP: rotary pump

Starting in the 1980s, manufacturers needed to fabricate HAR holes in SiO_2 with a depth of more than 1 μm and a diameter of less than 0.1 μm. This led to the development of high-density plasma sources and functional separation of plasma generation and ion-energy control [22,23] (Fig. 4).

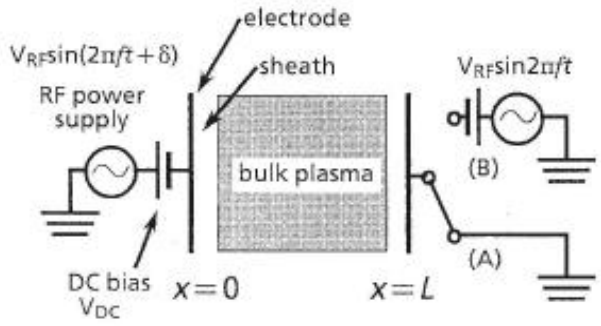

Fig. 4. Controllability of equipment was solved by new designs. Dual-frequency operation provided separate controllability of both (i) acceleration of bombardment energy and (ii) transport of reactants toward a desired location for reactions [22,23].

High-density plasma sources are categorized on the basis of their electron-excitation coupling mode: electrostatic (E), inductive (H), or electromagnetic surface wave. These modes were described by Sugai and Hikosaka in 1992 [24]. The three types of plasma coupling were simultaneously developed individually. An electron cyclotron

resonance (ECR) plasma apparatus design was developed by Okamoto and Tamagawa in 1972 [25,26]. A planar coupled ultra-high-frequency ECR plasma system was developed by Negishi et al. [27] and Yokogawa et al. [28]. An inductively coupled plasma (ICP) with a helical resonator and spiral- or transformer-coupled configurations was reviewed by Hopwood [29] (Fig. 5). For low-pressure operation, Sekine et al. developed a magnetic-enhanced RIE (MERIE) system [30]. A magnetic field parallel to the wafer plane in the reactor enhances the electron density.

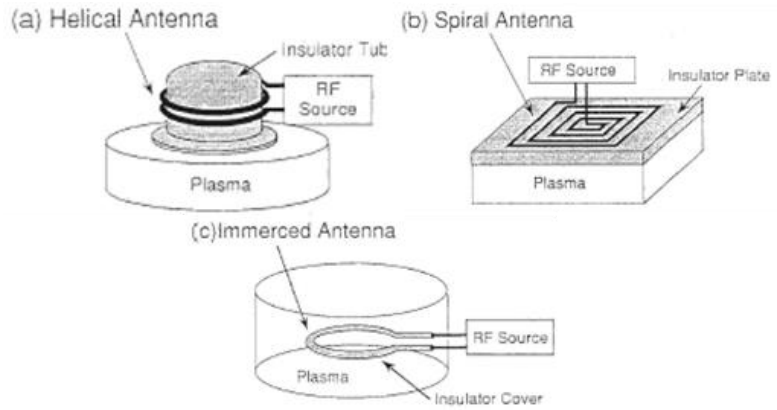

Fig. 5. Inductively coupled plasma (ICP) ion source with (a) helical antenna, (b) spiral antenna, or (c) immersed antenna [29].

For capacitively coupled plasmas at low pressures (~1 Pa), stochastic heating of electrons was identified as the dominant mechanism in radio frequency (RF) operations. Subsequently, the excitation frequency was increased from 13 MHz to higher levels [31–34], as detailed elsewhere [35,36]. Functional separation was achieved by the development of multiple-frequency operation. Concurrently with the shift to higher excitation frequencies, controlling the ion-bombardment energy received attention. This control was achieved by the introduction of a dual frequency capacitively coupled plasma etcher in the 1990s [22]. The simultaneous application of low-frequency power to the wafer electrode is used to separately control the energy of bombarded ions with an excited high-frequency power [37–44]. The functional separation of plasma excitation control and ion bombardment control has thus been achieved. Following the identification of serious issues in industrial manufacturing, technological processing was achieved through the combination of epoch-making ideas and multidisciplinary efforts.

1.2.2 Overview of semiconductor device technology nodes

In the 1970s, bipolar transistors were the main circuit components. In the 1980s, metal-on-silicon (MOS) structures were used for constructing transistors, and in the late 1980s, complementary MOS (CMOS) circuits were used for constructing LSI circuits. In the late 1990s, the CDs of circuit layouts became as small as 200 nm, enabling interconnect structures to transition into the Cu/low-k era. In the 2010s, gate materials as dielectrics were replaced by high-k and metal gate materials (high-k/metal gate). The "NOT-AND" (NAND) flash memory market expanded, and then its structure changed from 2D transistors to 3D stacked memory cells. Over the last few decades, transistor structures have changed from planar to damascene and then to the current fin-type. In the future, nanowires and nanosheets are promising channel materials that will extend the life of fin-type transistors. New device structures are continuing to be developed in, for example, 3D X-point and quantum computing elements. To bring a new idea or design to market, it is necessary to implement it in the real world. Dry processing technologies play a crucial role in this effort.

1.3 High-aspect-ratio etching

In the last decade, plasma etching technology has been used for more than just lithographic pattern transfer processing. This means that fin-type transistors and 3D flash memory were developed as solutions for the other structural construction schemes, rather than 2D pattern designs. Thus, functional evolution is involved in HAR feature etching, as reviewed separately here.

HAR etching technology has progressed in step with miniaturization technology, resulting in high-density integration in semiconductor devices. The number of reports related to HAR etching presented at dry process symposia since 1984 is plotted in Fig. 6 by application. Starting with silicon trench etching for fabricating shallow-trench isolation (STI) or trench capacitors for dynamic-random-access memory (DRAM), reports of HAR etching of silicon dioxide for DRAM contacts have been increasing since the 1990s. To increase device integration density, the self-aligning contact process was introduced and high selectivity etching of SiO_2 to SiN was reported by Enomoto et al. [45], Takahashi et al. [46], and Ito et al. [47]. Thereafter, low-k materials were used for

multi-level interconnects in logic devices. HAR etching received attention [48–50]. Meanwhile, highly resistive carbon masks deposited by chemical vapor deposition (CVD) attracted attention due to the increase in DRAM bit density [51,52]. Furthermore, system integration is continuing to demand densification using through silicon via (TSV) technology, which enables low-cost 3D integration of multiple chips [53]. The recent achievement of 3D flash memory enabled the development of stacked memory cells with HAR features, which have replaced 2D flash memory.

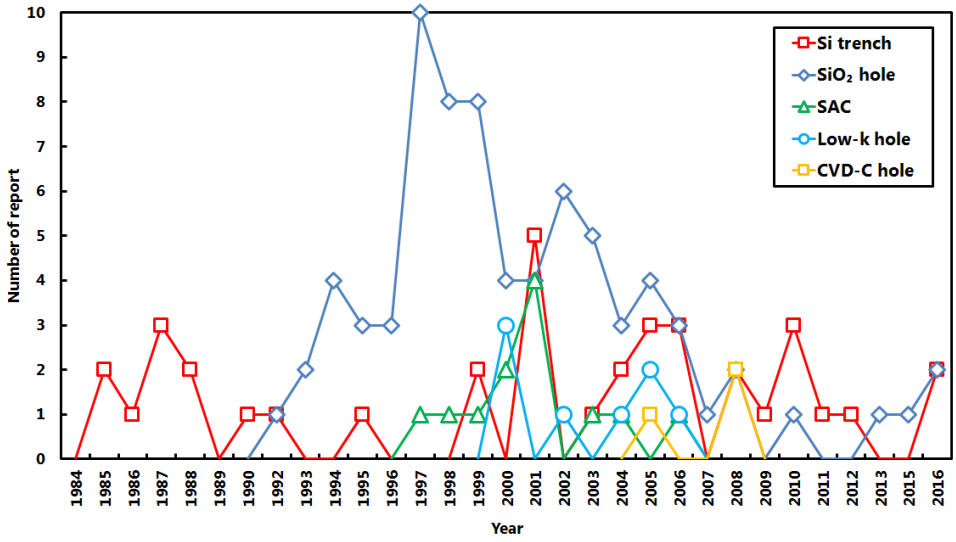

Fig. 6. Number of HAR etching-related reports presented at dry process symposia regarding Si trenches, SiO_2 holes, self-aligned contacts (SACs), low-dielectric constant (low-k) holes, and carbon CVD (CVD-C) holes.

Problems were encountered for the first time in the fabrication of cells with HAR features, including distorted hole shapes and twisted profiles [54]. Multiple stacks of films are necessary to finely control etching for creation of HAR holes for 3D flash memory [55–60] because measurements inside HAR features are not practically feasible due to technical difficulty. Furthermore, there is insufficient understanding of the phenomena in regard to the characteristics of HAR feature interiors, including a basic understanding of particle transport, such as ions and neutral species, of surface reactions on the sidewalls and bottom, and of electrical charging of the inner surface. Likewise, the increased mixing of gases makes the gas chemistry complex. For plasma generation, multiple frequencies

are applied, and their powers are pulsed and modulated temporarily. At present, this complexity is troublesome and highlights the difficulties of technological development. This section reviews selected reports since the 1990s. These reports are epoch-making, innovative, and full of originality. The basic experimental data are discussed in light of recent research, and future HAR etching technologies are considered.

1.3.1 Aspect-ratio-dependent etching (ARDE)

The most critical problem in ARDE is RIE lag. Several mechanisms possibly explain it, including ion shadowing, neutral shadowing, Knudsen neutral transport, electrical charging [61]. However, the explanation is still unclear. Evidence has not been shown that explains the difficulty of HAR hole analysis, and experimental conditions that enable control free from processing variations have not been reported. For example, individual experimental results for RIE lag at similar aspect ratios might not be suitably comparable and thus do not provide a unified simile mechanism for RIE lag. There has been much discussion of RIE lag and etch stop in HAR etching. They have been explained by geometrical shadowing of etching incidences [62, 63], passivation of fluorocarbon polymers over the hole bottom [64], and suppression of ion current flow [65,66]. The elevation of wafer temperature has been reported to reduce RIE lag [67], and high gas flow [68] by introduction of increase O_2 flow rates in fluorocarbon gases [65,69,70]. Subsequently, models were proposed for dealing with the effects of the mask aspect ratio [71,72] and with the causes of etch by-product deposition [73,74]. While broad themes were discussed, a consensus was not reached.

As an analytical approach, the ion flux at the hole bottom was investigated using orifices, which were used for a model of hole structures. A quadrupole mass spectrometer (QMS) was used for measuring the ions generated in the plasma. Although the ion fluxes were measured, the experimental data failed to explain the etching rates. An inconsistency is considered to arise from charge-neutralization at hole sidewalls. Experiments using a capillary plate (CP) demonstrated that ion-neutralized species contribute to etching reactions with similarly highly energetic bombardments onto the hole bottom (Fig. 7) [75,76]. The etch depth with an 80-μm space was shallower than that without a space (an aspect ratio of 10 was obtained using a CP with a 25-μm hole diameter and 250-μm depth). This indicates that even if the incident ions collide with a sidewall and are neutralized,

they still retain sufficient energy to etch the hole bottom. This clear contribution of highly energetic neutrals is supported by recent computational approaches using hot neutrals [77]. Further investigation is necessary.

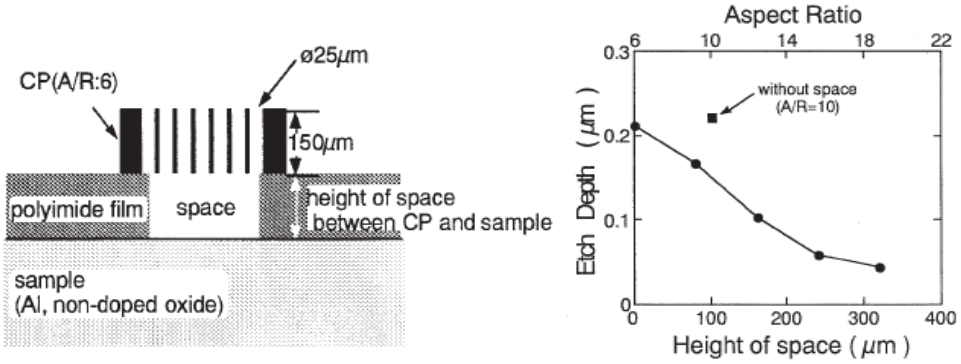

Fig. 7. (left) Experimental set up with CP above sample. (right) Al etch depth as a function of height of space between CP and sample [75,76].

1.3.2 Effects of IEDF/IADF on HAR etching

To fabricate HAR features, etching processes with high-energy ion bombardment are necessary to offer transport sufficient reactants toward the hole bottom. The real views of ion-energy distributions are broad due to RF oscillation of the potentials in the ion sheaths. As a result, the actual ion energy distribution function (IEDF) shows broad energy in common the bimodal distribution. However, the actual IEDF at the feature bottom is rarely measured.

Kurihara et al. reported an experimentally measured IED using a QMS equipped with orifices having an aspect ratio of 40 [78–80]. A bimodal distribution function was observed before the ions passed through the orifice while the high-energy peak was stronger in intensity than that of the low-energy one after they passed through it. This means that low-energy ions cannot be transported to the bottom of HAR features (Fig. 8) [78].

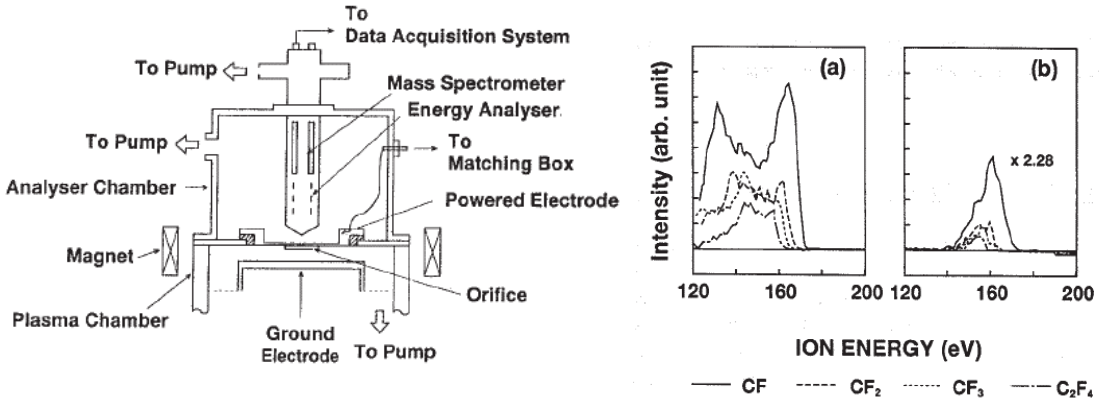

Fig. 8. (left) Schematic cross section of experimental setup. (right) Ion-energy distribution in 5-mTorr C_4F_8 (a) before ions passed through orifice (aspect ratio = 40) and (b) after they passed through it. Relative amount of CF^+ increased and low-energy IED region was truncated through orifice (aspect ratio = 40) [78].

A similar measurement of the ion velocity distribution function was recently reported in which a CP and a multi-grid retarding field analyzer were used [81]. Noda et al. prepared a CP having a hole size of 0.2 μm in diameter. In QMS measurements using the CP, they successfully obtained an experimental IEDF for ions reaching the bottom of a HAR hole with a diameter of 200 nm [82,83]. Further investigations are expected to be conducted aimed at comprehensively understanding the actual IEDF. In the pulsed operation of plasma excitation as used in industry, the temporal behaviors in the IEDF need to be investigated using a highly temporal resolution setup.

A setup with an overhang feature was used for measuring the ion angular distribution function (IADF), and the results were analyzed using computational prediction [84–86]. There have been few reports on the measurement of IADF. A new technique was recently reported for measuring the angular distribution of ions bombarding a substrate surface with a resolution as low as 3° [87], so there is hope for future progress in technologies needed for further understanding incident ion behavior.

1.3.3 Ion and neutral transport inside HAR holes

In plasma etching for fabricating HAR holes in dielectric films, the process conditions are commonly adjusted to obtain high selectivity of oxide against other materials. Under these conditions, fluorocarbon films are normally deposited on the

etched surface as well as on the sidewalls of the etched features. The deposited films affect the resulting etching rates and profiles. As a result, many research projects are underway with a focus on the sticking coefficients of deposited precursors and the reaction constants of incident ions. One approach is to observe a cross section of the etching features. Yabe et al. analyzed the sticking coefficients for CF_x radicals on the basis of observations of fluorocarbon films deposited on the surface and sidewalls of etched features [88,89]. Gotoh et al. argued for a mechanism of fluorocarbon deposition and analyzed the sticking coefficient of CF_x radicals by using overhanging structures on the wafer [90–93]. Kubota et al. used a QMS to measure the transport of radicals inside a thin quartz tube with a small inner diameter, which was regarded as having an aspect ratio of 20. The CF radical densities dropped rapidly with an increase in the aspect ratio while the CF_2 radical densities showed almost no decay (Fig. 9) [94,95].

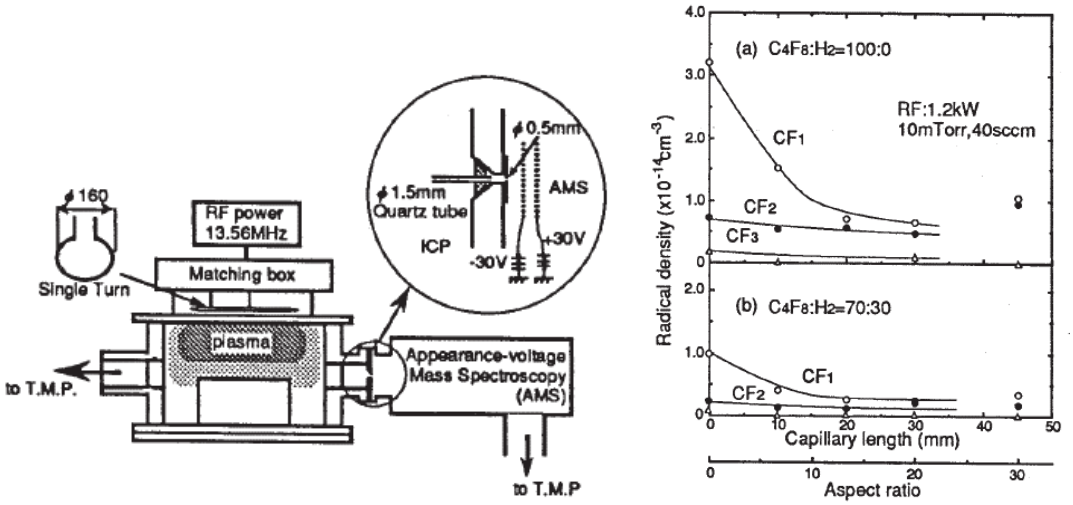

Fig. 9. (left) ICP experimental system combined with appearance-voltage mass spectrometer (AMS). (right) Densities of CF, CF_2, and CF_3 radicals vs. aspect ratio of capillary tube. TMP: turbo-molecular drag pump

Arai et al. reported that deposition rates at a small trench bottom decreased when the aspect ratio was increased and bias power was not applied. When bias power was applied, the deposition rate decreased at low aspect ratios and increased at high aspect ratios. They concluded that ion sputtering on the sidewall greatly affects the radicals and/or particles supplied to the bottom of HAR trenches. Their results were temperature

dependent and related to the SiO_2 etching rate. The decrease in the etch rate at high aspect ratios was suppressed by controlling deposition on the bottom in the high substrate temperature range [67,68].

Ono et al. reported that the deposition rates for fluorocarbon films on a hole bottom were larger when the hole diameter was smaller and the taper angles of the hole profiles were sharper, increasing the carbon content in the films, because ionic bombardment formed C-rich films [96–98]. In contrast, Hayashi et al. reported F-rich film deposition when they compared the compositions of fluorocarbons deposited on SiN films regardless of whether the CP was covered, which is consistent with radical measurements using an AMS with CPs [65,66]. This means that the deposition behaviors are determined by multiple parameters including the plasma source, whether ECR or capacitively coupled plasma is used, the gas chemistry, the bias power, and the substrate material. These reports revealed the complexity of the phenomena occurring inside HAR holes.

Subsequently, the compositional analysis of sidewalls and hole bottoms was analyzed using a secondary ion mass spectrometer (SIMS) with grazing incident ions [99,100] and using angle-resolved X-ray photoelectron spectroscopy (XPS) [101,102]. Recent reports revealed that the compositional ratio of fluorocarbon film at a hole bottom is inversely observed when bias power is turned on and off [103]. In accordance with these situations, it is difficult to reach a consensus on the complicated phenomena observed in the study of ion and neutral transport inside HAR holes. The step by step accumulation of a large amount of fundamental knowledge should one day resolve this difficulty. However, a comprehensive understanding is expected to be very challenging.

1.3.4 Charging and charge buildup

Imbalances between electrons and positive ions occur at the bottom of a HAR feature because anisotropic positive ions reach the bottom while isotropic electrons do not easily enter a HAR feature. This charging phenomenon is called the “electron shading effect.” This effect causes a self-bias voltage (Vdc) drop in a HAR feature. Hayashi et al. measured the Vdc at the bottom of contact holes formed on Si wafers as a function of the aspect ratio. A $|Vdc|$ of 515 V on a flat cathode surface (corresponding to an aspect

ratio of 0) decreased to 450 V (~10% lower) when the aspect ratio was increased to 7 (Fig. 10) [65,66].

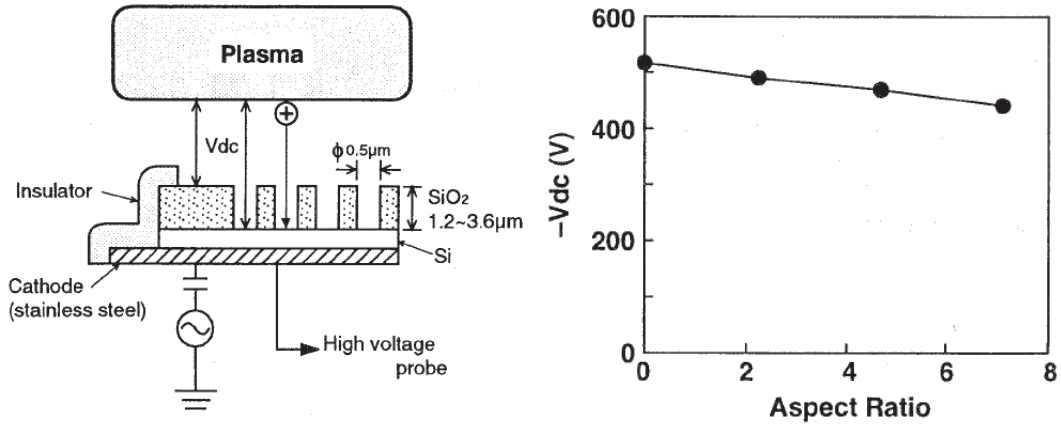

Fig. 10. (left) Schematic of Vdc measurement. (right) –Vdc as a function of aspect ratio. Vdc at hole bottom (aspect ratio = 7) was measured using high-voltage probe and patterned sample [65].

Yonekura et al. showed that the charging effects differ depending on whether the conductive materials at the hole bottom were connected with a wide-open space because a positive charge at the bottom of a contact hole is canceled by electrons supplied from a wide-open area. Without such a connection, the bottom of a hole is positively charged by the electron shading effect, preventing the low-energy ions from reaching the bottom. This makes bottom fluorocarbon films F-rich, which causes an increase in the etch rate of the conductive film underneath [104–107]. Other researchers clarified the relationship between Vdc reduction due to the electron shading effect and the conductivity of passivating films on the sidewall. The Vdc reduction and of the charging voltage difference were measured for various conditions of the electrical conductivity of fluorocarbon films and the deposition behaviors on the sidewalls (Fig. 11) [108–112]. The results indicated that deposited fluorocarbon film in contact holes may mitigate the electron shading effect [109].

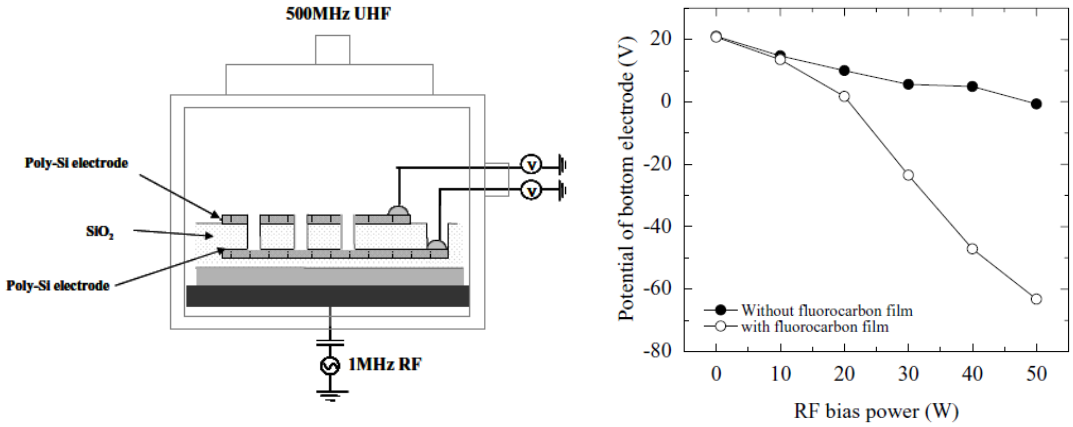

Fig. 11. (left) Schematic diagram of on-wafer monitoring for measurement of charging potential. (right) Electric potential of hole bottom poly-Si electrode with (○) and without (●) deposited fluorocarbon film as a function of RF bias power.

In the fabrication of 3D flash memory, the applied bias power continues to increase. These high voltages are beginning to increase the difficulty of the Vdc and charge measurements. This information, which reveals the ion energy, is the most important among a variety of parameters. New measurement techniques are necessary to make advances, and also a novel technique is expected to be developed.

1.3.5 Abnormal profiles (bowing, striation, distortion, twisting)

The most well-known challenge in HAR etching is bowing, which is enlargement of the hole diameter at the middle region of the hole. It has been the subject of many studies since the 1990s, Ikegami et al. reported that even if the hole sidewalls immediately under the mask were removed by wet etching, bowing always occurred in almost the same position, indicating that the first stage of bowing development is associated with ion trajectory bending at the poly-Si mask [71,72]. Izawa et al. showed that the sticking coefficient of each type of radical at the sidewall of a hole strongly affects the etching profile and that bowing can be suppressed by controlling the oxygen flux (Fig. 12) [113]. Negishi et al. reported that bowing could be suppressed by formation of a protective sidewall film, which was successfully formed by controlling the radical species and their sticking coefficients. The flux of CF_2 radicals was optimized by adjusting the Ar flow rate, and the sticking coefficients were controlled by raising the wafer

temperature [114]. Yonekura et al. also reported that increasing the wafer temperature improves the bowing profile [115]. Miyake et al. found that reducing the mask taper angle increases the bowing/necking ratio and decreases mask selectivity [116,117]. The effects of the inert gas type and flow rate on the bowing depth and size were investigated by Son et al. They reported that bowing was reduced by introducing He gas due to shallow passivation polymer formation and ion flux and that bowing decreased 22% when the Ar flow rate was reduced, probably due to the decreased ion flux [118].

Striation is a kind of vertical scratch on the sidewall of the pattern that degrades pattern fidelity. Negishi et al. reported that suppression of ArF resist degradation during fabrication of bottom anti-reflective coating (BARC) films and HAR contact holes is essential for reducing striation in the etched profile. Generation of a degradation trigger such as a carbon-rich micro-mask can be avoided by using argon-less or fluorine- and oxygen-rich chemistries in the BARC etching step. A striation-less and pitting-less etched-hole profile was obtained using an Ar-and-Xe mixture (20%) as a dilution gas or a fluorocarbon gas at a low flow rate under low pressure in the HAR contact (HARC) etching step (Fig. 13) [119,120].

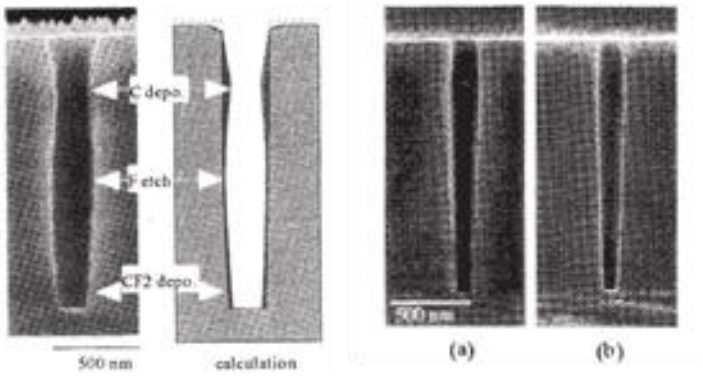

Fig. 12. (left) Deposition profile with RF bias at 100 ºC. Sticking coefficients of C, F, and CF_2 in calculation were respectively set to 0.5, 0.07, and 0.004. F was assumed to etch deposited film. (right) Etching profile (a) without and (b) with O_2 control. Hole diameter was 0.14 μm. Etching was carried out using UHF-ECR plasma with gas mixture of Ar, C_4F_8, CO, and O_2 [113].

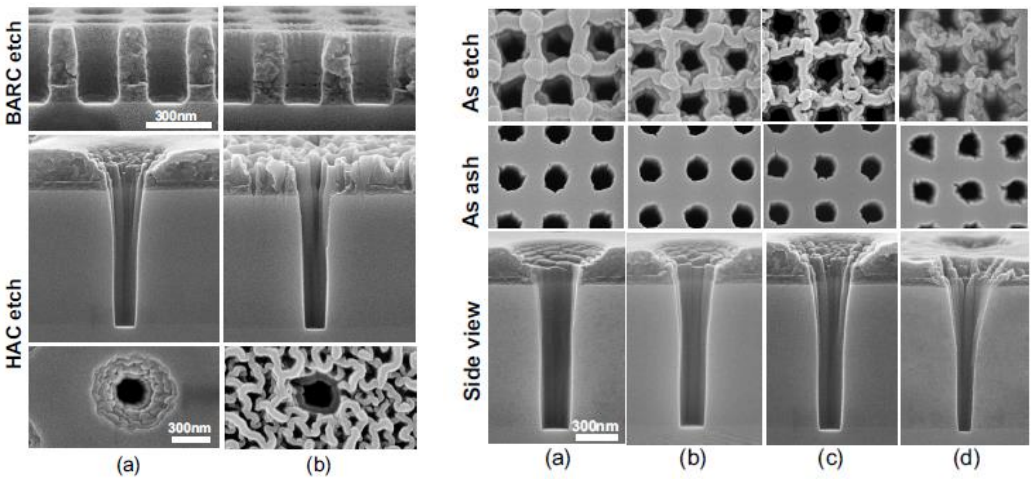

Fig. 13. (left) Scanning electron microscopy (SEM) images of BARC and HAC(HARC) profiles for different BARC processes: (a) pure CF_4; (b) Ar/CF_4. Typical HARC process uses Ar/C_4F_6/O_2/CO chemistry. (right) Top and side views of HARC etched profiles and ashed profiles for various dilution gases: (a) Xe, (b) Ar-and-Xe (20%), (c) Ar, and (d) He. ArF resist degradation during BARC and HARC etching step was reduced by controlling BARC etched surface roughness and fluorocarbon polymers during HARC process [119].

Hole shape distortion and HAR hole twisting have been gaining attention as serious problems. Huang et al. investigated profile distortion and shape twisting during HAR oval contact etching [54]. Miyake et al. reported that asymmetric mask deformation and asymmetric growth of the necking cause inequality of ion flux at the sidewalls, resulting in twisting (Fig. 14) [116,117].

These phenomena are not yet fully understood: therefore, elucidation of the root cause and research into controls are urgent issues. In addition, simulation technology has been used to analyze the HAR etching process. Excellent results for modeling of oval contact etching [121] and formation of facets and necking at masks [122,123] were reported more than ten years ago, and the reliance on simulation technology has since grown. This technology is expected to greatly contribute to the further development of HAR etching in the future.

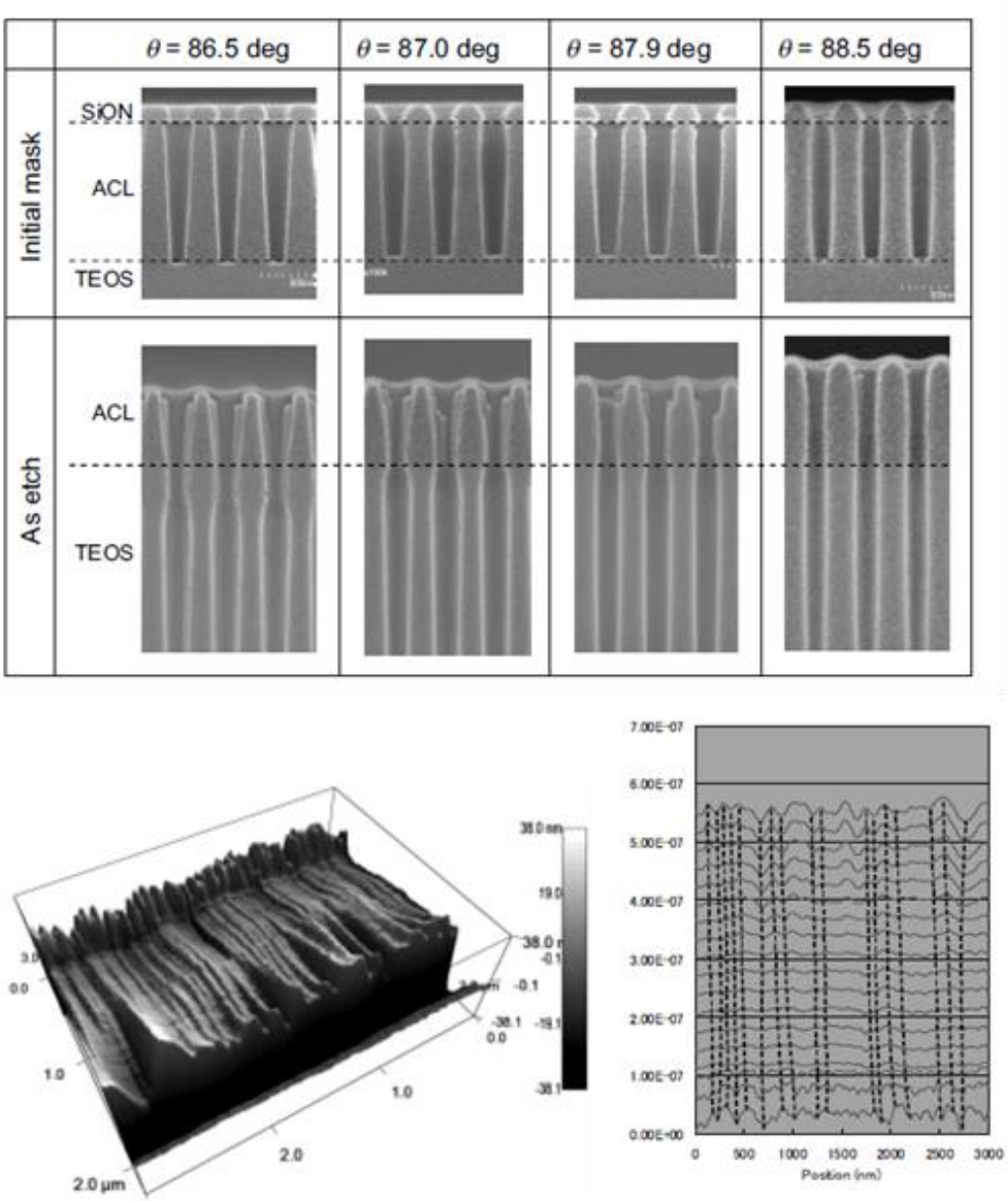

Fig. 14. (upper) Cross-sectional SEM images of initial tapered amorphous carbon layer mask profiles and HARC etched profiles with diameter of 100 nm. (left) Atomic force microscope image of 90-nm trench sidewall. Mask-edge roughness and non-uniformity of necking affected bottom part of sidewall. (right) Calculated incident ion flux at sidewall as a function of aspect ratio in hexagonal hole (tilt angle = 5 deg.).

1.4 Stacked multilayer etching

To overcome scaling limitations, the structure of NAND flash memories has evolved from planar to 3D. In the 3D NAND flash architecture, memory cells are stacked

perpendicularly in an integrated device. 3D NAND devices such as bit-cost scalable (BiCS) [124–126], vertical-gate NAND (VG-NAND) [127–129], and terabit-cell-array transistor (TCAT) [130] ones reduce production costs per memory bit due to using a single deep-etching process. These stacked devices are typically composed of alternating layers of SiN (or polycrystalline-Si) and SiO_2 [131–135].

In 3D NAND fabrication, it is difficult to form extremely HAR holes through over 30 stacked film layers with both a vertical profile and high throughput. By using, for example, a known technology, a cyclic process can be used in which etching SiO_2 with fluorocarbon-based gas is alternated with etching poly-Si with HBr gas [136–139]. However, this alternating process degrades throughput because additional time is needed for the residual gases to be exhausted and the pressure to stabilize before the next etching step. Thus, a single-step etching process under unique conditions could be a promising technology for obtaining high throughput although this requires developing a novel process and hardware. In a previous study, a one-piece etching reactor was developed that can etch both poly-Si and SiO_2 materials [140].

One of the problems with HAR etching of multiple layers is the decrease in the etching rate as the aspect ratio of the holes/trenches increases. A dominant factor in this "etch-rate drop" problem is the decrease in the density of the etchant, such as ions and radicals with an increase in the aspect ratio. Several approaches have been investigated to suppress the etch-rate drop [141]. One is to increase the ion energy to compensate for the decrease in the ion flux. Another is to increase the plasma density to increase the flux of the ions and radicals. A third is to reduce the sticking coefficient of the radicals to enhance the transport of the radicals to the bottom of the holes/trenches. A fourth is to control the deposition characteristics to increase the etching efficiency with ion bombardment.

1.5 Objectives of this study

This study focused on the development of an etching process for fabricating vertical holes through different-material stacked films for 3D-NAND fabrication. A critical goal was achieving both a vertical profile and high throughput for multiple-stack etching. While the conventional process consists of multiple steps for each stacked layer, this study investigated the use of HBr/fluorocarbon-based gas chemistry to achieve a single-

step etching process and thereby reduce processing time. The effects of wafer temperature on the etching rate and surface composition were investigated to clarify the surface reaction mechanism under HBr/N_2/fluorocarbon-based gas plasma. The deposition profile of a key material in the plasmas was investigated using macro cavities in order to develop a model of the deposition material which indicates a mechanism of the material to reach deeply.

1.6 Organization of this dissertation

This dissertation is organized as follows. Chapter 2 describes how a single-step etching process was achieved by using HBr/N_2/fluorocarbon-based gas plasma to create a vertical hole profile in a poly-Si/SiO_2 stack. Chapter 3 discusses the investigation of the effects of wafer temperature on the etching rate and surface composition that clarified the surface reaction mechanism under HBr/N_2/fluorocarbon-based gas plasma. Chapter 4 discusses the investigation of the reaction mechanism during etching to fabricate deep holes in SiN/SiO_2 stacks by using a HBr/N_2/fluorocarbon-based gas plasma. Chapter 5 describes the evaluation of the deposition profile of ammonium bromide in N_2/HBr plasmas as a function of the depth of a macro-cavity structure for HAR etching. Chapter 6 summarizes the key points of this dissertation.

References

[1] In Gartner report of "*Market share analysis: Semiconductor worldwide, 2017*", (2018).

[2] S. Tachi, J. Vac. Sci. Technol. A **21**, S131 (2003).

[3] H. Abe, M. Yoneda, and N. Fujiwara, Japan. J. Appl. Phys. **47**, 1435 (2008).

[4] K. Eriguchi, Japan. J. Appl. Phys. **56**, 06HA01 (2017).

[5] K. Ishikawa, K. Karahashi, T. Ichiki, J. P. Chang, S. M. George, W. M. M. Kessels, H. J. Lee, S. Tinck, J. H. Um, and K. Kinoshita, Japan. J. Appl. Phys. **56**, 06HA02 (2017).

[6] K. Ishikawa, K. Karahashi, T. Ishijima, S. I. Cho, S. Elliott, D. Hausmann, D. Mocuta, A. Wilson, and K. Kinoshita, Japan. J. Appl. Phys. **57**, 06JA01 (2018).

[7] M. J. Madou, "*Pattern transfer with dry etching techniquies*", in "*Fundamentals of microfabrication: The science of miniaturization, 2nd ed.*", (CRC Press, 2002), p. 77.

[8] J. R. Hauser, "Introduction to semiconductor devices", in "*Handbook of Semiconductor Manufacturing Technology, 2nd ed.*", ed. by Y. Nishi and R. Doering, (CRC Press, Florida USA, 2007), p. 1-2.

[9] R. A. Powell, "*Reactive ion beam etching*", in "*Dry etching for microelectronics"*, ed. by P. A. Powell (Elsevier, 1984), p. 115.

[10] N. Hosokawa, R. Matsuzaki, and T. Asamaki, Japan. J. Appl. Phys. 13, 435 (1974).

[11] S. Matsuo, *Proceedings of 1st Dry Process Symposium* (The Institute of Electrical Engineers of Japan, Tokyo, 1979), p. 13.

[12] J. Coburn and H. Winters, J. Appl. Phys. **50**, 3189 (1979).

[13] J. Coburn, *Proceedings of 2nd Dry Process Symposium* (The Institute of Electrical Engineers of Japan, Tokyo, 1980), p. 103.

[14] A. von Keudell, and C. Corbella, J. Vac. Sci. Technol. A **35**, 050801 (2017).

[15] M. Kumagawa, H. Sunami, T. Terasaki, and J. Nishizawa, Japan. J. Appl. Phys. **7**, 1332 (1968).

[16] J. Nishizawa and N. Hayasaka, *157th Electrochem. Soc. Meeting, the plasma etching and deposition symposium* (1980).

[17] N. Abe, "Method and Apparatus for Dry Etching and Electrostatic Chucking Device used therein", U.S. Pat. No. 4,384,918 May 24, 1983

[18] M. Nakamura, T. Kurimoto, H. Yano, and K. Yanagida, *Proceedings of 9th Dry Process Symposium* (The Electrochemical Society USA, Hawaii, 1987), p. 1042.

[19] E. Ikawa, S. Sugito, and Y. Kurogi, *Proceedings of 7th Dry Process Symposium* (The Institute of Electrical Engineers of Japan, Tokyo, 1985),

[20] N. Jiwari, H. Iwasawa, A. Nara, H. Sakaue, H. Sindo, T. Shoji, and Y. Horiike, *Proceedings of 14th Dry Process Symposium* (The Institute of Electrical Engineers of Japan, Tokyo, 1992), p. 23.

[21] K. Tsujimoto, T. Kumihashi, N. Kofuji, and S. Tachi, J. Vac. Sci. Technol. A **12**, 1209 (1994).

[22] K. Harahuji, A. Yamano, and M. Kubota, *Proceedings of 15th Dry Process Symposium* (The Institute of Electrical Engineers of Japan, Tokyo, 1993), p.11.

[23] K. Harafuji, A. Yamano, and M. Kubota, Japan. J. Appl. Phys. **33**, 2212 (1995).

[24] H. Sugai, and Y Hikosaka, *Proceedings of 14th Dry Process Symposium* (The Institute of Electrical Engineers of Japan, Tokyo, 1992) p.27.

[25] Y. Okamoto and H. Tamagawa, Japan. J. Appl. Phys. **11**, 726 (1972).

[26] Y. Okamoto and H. Tamagawa, Rev. Sci. Inst. **43**, 1193 (1972).

[27] N. Negishi, M. Izawa, K. Yokogawa, Y. Momonoi, T. Yoshida, K. Nakaune, H. Kawahara, M. Kojima, K. Tsujimoto, and S. Tachi, *Proceedings of 22nd Dry Process Symposium* (The Institute of Electrical Engineers of Japan, Tokyo, 2000), p. 31.

[28] K. Yokogawa, N. Itabashi, K. Suzuki, and S. Tachi, *Electrochemical Society Series 97*, *Proc. the symposium on silicon nitride and silicon dioxide thin insulating films*, (Montreal, Canada, 1997), p. 493.

[29] J. Hopwood, Plasma Sources Sci. Technol. **1**, 109 (1992).

[30] M. Sekine, M. Narita, S. Shimonishi, I. Sakai, K. Tomioka, K. Horioka, Y. Yoshida, and H. Okano, *Proceedings of 15th Dry Process Symposium* (The Institute of Electrical Engineers of Japan, Tokyo, 1993), p. 17.

[31] T. Kaminishizono, T. Akimoto, and E. Ikawa, *Proceedings of 17th Dry Process Symposium* (The Institute of Electrical Engineers of Japan, Tokyo, 1995), p. 213.

[32] T. Akimoto, E. Ikawa, T. Sango, K. Komachi, K. Kitayama, and T. Ebata, Japan. J. Appl. Phys. **33**, 7037 (1994).

[33] K. Yoshida, H. Miyamoto, E. Ikawa, and Y. Murao, Japan. J. Appl. Phys. **34**, 2089 (1995).

[34] W. Tsai, G. Mueller, R. Lindquist, B. Frazier, and V. Vahedi, J. Vac. Sci. Technol. B **14**, 3276 (1996).

[35] M. A. Liberman and A. J. Litchtenberg, "*Principles of plasma discharges and material processing, 2nd ed*." (Wiley-interscience, New Jersey USA, 2005)

[36] P. Chabert and N. Braithwaite, "*Physics of radio-frequency plasmas*", (Cambridge University Press, Cambridge UK, 2011).

[37] M. Sekine, Appl. Surf. Sci. **192**, 135 (2002).

[38] S. Morishita, H. Hayashi, T. Tatsumi, Y. Hikosaka, S. Noda, M. Okigawa, M. Matsui, M. Inoue, and M. Sekine, Japan. J. Appl. Phys. **37**, 6899 (1998)

[39] T. Tatsumi, Y. Hikosaka, S. Morishita, M. Matsui, and M. Sekine, J. Vac. Sci. Technol. A **17**, 1562 (1999).

[40] H. Hayashi, M. Okigawa, S. Morishita, and M. Sekine, J. Vac. Sci. Technol. A **17**, 2517 (1999).

[41] H. Hayashi, S. Morishita, T. Tatsumi, Y. Hikosaka, S. Noda, H. Nakagawa, S. Kobayashi, M. Inoue, and T. Hoshino, J. Vac. Sci. Technol. A **17**, 2557 (1999).

[42] T. Tatsumi, M. Matsui, M. Okigawa, and M. Sekine, J. Vac. Sci. Technol. B **18**, 1897 (2000).

[43] M. Matsui, T. Tatsumi, and M. Sekine, J. Vac. Sci. Technol. A **19**, 1282 (2001).

[44] M. Matsui, T. Tatsumi, and M. Sekine, J. Vac. Sci. Technol. A **19**, 2089 (2001).

[45] H. Enomoto, K. Tago, N. Ohashi, and T. Tokunaga, *Proceedings of 19th Dry Process Symposium* (The Institute of Electrical Engineers of Japan, Tokyo, 1997), p. 157.

[46] A. Takahashi, N. Ikegami, M. Kobayashi, and J. Kanamori, *Proceedings of 20th Dry Process Symposium* (The Institute of Electrical Engineers of Japan, Tokyo, 1998), p. 251.

[47] Y. Ito, A. Koshiishi, R. Shimizu, M. Hagiwara, K. Inazawa, and E. Nishimura, *Proceedings of 20th Dry Process Symposium* (The Institute of Electrical Engineers of Japan, Tokyo, 1998), p. 263.

[48] O. Joubert, L. Vallier, P. Czuprynski, F. Vinet, P. Berruyer, and C. Verove, *Proceedings of 20th Dry Process Symposium* (The Institute of Electrical Engineers of Japan, Tokyo, 1998), p. 241.

[49] H. Nakagawa, Y. Morikawa, E. Tamaoka, and T. Hayashi, *Proceedings of 22nd Dry Process Symposium* (The Institute of Electrical Engineers of Japan, Tokyo, 2000), p. 257.

[50] T. Sakata, S. Komagata, S. Noda, N. Ikegami, M. Kobayashi, and J. Kanamori, *Proceedings of 22nd Dry Process Symposium* (The Institute of Electrical Engineers of Japan, Tokyo, 2000), p. 275.

[51] J. R. Han, Y. H. Liao, M. Chen, I. Huang, M. Hsieh, E. Chen, and M. Hiroshi, *Proceedings of 30th Dry Process Symposium* (Japanese Society of Applied Physics, Tokyo, 2008), p. 159.

[52] J. K. Kim, Y. J. Choi, S. -I. Cho, S. S. Jeong, S. W. Nam, C. -J. Kang, and T. H. Ahn, *Proceedings of 30th Dry Process Symposium* (Japanese Society of Applied Physics, Tokyo, 2008), p. 271.

[53] C. G. Kim, D. S. Lee, B. H. Jeong, J. Yu, and W. J. Lee, *Proceedings of 30th Dry Process Symposium* (Japanese Society of Applied Physics, Tokyo, 2008), p. 99.

[54] A. J. J. Huang, C. C. Min, J. K. Ma, Y. M. Tseng, W. J. Wang, C. M. Wu, C. C. Lin, and T. Y. Huang, *Proceedings of 28th Dry Process Symposium* (Japanese Society of Applied Physics, Nagoya, 2006), p. 263.

[55] T. Iwase, M. Matsui, K. Yokogawa, T. Arase, and M. Mori, *Proceedings of 37th Dry Process Symposium* (Japanese Society of Applied Physics, Awaji island, 2015), p. 47.

[56] T. Iwase, M. Matsui, K. Yokogawa, T. Arase, and M. Mori, Japan. J. Appl. Phys. **55**, 06HB02 (2016).

[57] T. Iwase, K. Yokogawa, and M. Mori, *Proceedings of 38th Dry Process Symposium* (Japanese Society of Applied Physics, Hokkaido, 2016), p. 197.

[58] T. Iwase, K. Yokogawa, and M. Mori, Japan. J. Appl. Phys. **56**, 06HB04 (2017).

[59] T. Iwase, K. Yokogawa, and M. Mori, *Proceedings of 39th Dry Process Symposium* (Japanese Society of Applied Physics, Tokyo, 2017), p. 209.

[60] T. Iwase, K. Yokogawa, and M. Mori, Japan. J. Appl. Phys. **57**, 06JC03 (2018).

[61] R. A. Gottscho, C. W. Jurgensen, and D. J. Vitkavage, J. Vac. Sci. Technol. B **10**, 2133 (1992).

[62] M. Oda, H. Namatsu, S. Ohki, H. Akiya, and T. Shibata, *Proceedings of 6th Dry Process Symposium* (The Institute of Electrical Engineers of Japan, Tokyo, 1984), p. 115.

[63] S. Ohki, M. Oda, H. Akiya, and T. Shibata, J. Vac. Sci. Technol. B **5**, 1611 (1987).

[64] H. Hayashi, T. Ohiwa, H. Tamura, M. Matsushita, I. Hasegawa, K. Horioka, and H. Okano, *Proceedings of 14th Dry Process Symposium* (The Institute of Electrical Engineers of Japan, Tokyo, 1992), p. 205.

[65] H. Hayashi, K. Kurihara, and M. Sekine, *Proceedings of 17th Dry Process Symposium* (The Institute of Electrical Engineers of Japan, Tokyo, 1995), p. 225.

[66] H. Hayashi, K. Kurihara, and M. Sekine, Japan. J. Appl. Phys. **35**, 2488 (1996).

[67] S. Arai, N. Kofuji, K. Tsujimoto, and T. Mizutani, *Proceedings of 16th Dry Process Symposium* (The Institute of Electrical Engineers of Japan, Tokyo, 1994), p. 223.

[68] N. Kofuji, K. Tsujimoto, T. Kumihashi, and T. Mizutani, Japan. J. Appl. Phys. **34**, 2489 (1995).

[69] K. Shiozawa, K. Tabaru, T. Maruyama, N. Fujiwara, and M. Yoneda, *Proceedings of 17th Dry Process Symposium* (The Institute of Electrical Engineers of Japan, Tokyo, 1995), p. 255.

[70] H. Kimura, K. Shiozawa, K. Kawai, H. Miyatake, and M. Yoneda, Japan. J. Appl. Phys. **34**, 2114 (1995).

[71] N. Ikegami, A. Yabata, T. Matsui, J. Kanamori, and Y. Horiike, *Proceedings of 18th Dry Process Symposium* (The Institute of Electrical Engineers of Japan, Tokyo, 1996), p. 147.

[72] N. Ikegami, A. Yabata, T. Matsui, J. Kanamori, and Y. Horiike, Japan. J. Appl. Phys. **36**, 2470 (1997).

[73] K. Nishikawa, S. Tomohisa, H. Ootera, and T. Oomori, *Proceedings of 19th Dry Process Symposium* (The Institute of Electrical Engineers of Japan, Tokyo, 1997), p. 145.

[74] K. Nishikawa, T. Oomori, and K. Ono, J. Vac. Sci. Technol. B **17**, 127 (1999).

[75] A. Kojima, T. Ohiwa, M. Sekine, I. Sakai, S. Yonemoto, and Y. Watanabe, *Proceedings of 19th Dry Process Symposium* (The Institute of Electrical Engineers of Japan, Tokyo, 1997), p. 151.

[76] T. Ohiwa, A. Kojima, M. Sekine, I. Sakai, S. Yonemoto, and Y. Watanabe, Japan. J. Appl. Phys. **37**, 5060 (1998).

[77] M. Wang, A. Mosden, and M. J. Kushner, *Proceedings of the 65th International Symposium of the American Vacuum Society*, (Long Beach, CA, October, 2018) PS+EM+SE-TuM6.

[78] K. Kurihara, M. Sekine, K. Horioka, and H. Okano, *Proceedings of 16th Dry Process Symposium* (The Institute of Electrical Engineers of Japan, Tokyo, 1994), p. 217.

[79] K. Kurihara, and M. Sekine, Plasma Source, Sci. Technol. **5**, 121 (1996).

[80] K. Kurihara, and M. Sekine, Japan. J. Appl. Phys. **39**, 1369 (2000).

[81] G. Cunge, M. Darnon, J. Dubois, P. Bezard, O. Mourey, C. Petit-Etienne, L. Vallier, E. Despiau-Pujo, and N. Sadeghi, Appl. Phys. Lett. 108, 093109 (2016).

[82] S. Noda, T. Kinoshita, Y. Hikosaka, N. Ozawa, H. Tsuboi, K. Kinoshita, and M. Sekine, *Proceedings of 21st Dry Process Symposium* (The Institute of Electrical Engineers of Japan, Tokyo, 1999), p. 309.

[83] S. Noda, N. Ozawa, T. Kinoshita, H. Tsuboi, K. Kawashima, Y. Hikosaka, K. Kinoshita, and M. Sekine, Thin Solid Film **374**, 181 (2000).

[84] S. Kato, M, Sato, and Y. Arita, *Proceedings of 11st Dry Process Symposium* (The Institute of Electrical Engineers of Japan, Tokyo, 1989), p. 33.

[85] M, Sato, S. Kato, and Y. Arita, Japan. J. Appl. Phys. **30**, 1549 (1991).

[86] S. Kato, M, Sato, and Y. Arita, J. Vac. Sci. Technol. A **12**, 1204 (1994).

[87] S. Sharma, D. Gahan, P. Scullin, S. Daniels, and M. B. Hopkins, Rev. Sci. Instrum. **86**, 113501 (2015).

[88] H. Yabe, A. Yuuki, and Y. Matsui, *Proceedings of 12th Dry Process Symposium* (The Institute of Electrical Engineers of Japan, Tokyo, 1990), p. 23.

[89] H. Yabe, A. Yuuki, and Y. Matsui, Japan. J. Appl. Phys. **30**, 2873 (1991).

[90] Y. Gotoh, T. Kure, and S. Tachi, *Proceedings of 14th Dry Process Symposium* (The Institute of Electrical Engineers of Japan, Tokyo, 1992), p. 199.

[91] Y. Gotoh, T. Kure, and S. Tachi, Japan. J. Appl. Phys. **32**, 3035 (1993).

[92] Y. Gotoh, and T. Kure, *Proceedings of 16th Dry Process Symposium* (The Institute of Electrical Engineers of Japan, Tokyo, 1994), p. 211.

[93] Y. Gotoh, and T. Kure, Japan. J. Appl. Phys. **34**, 2132 (1995).

[94] K. Kubota, H. Matsumoto, H. Shindo, S. Shingubara, and Y. Horiike, *Proceedings of 16th Dry Process Symposium* (The Institute of Electrical Engineers of Japan, Tokyo, 1994), p. 205.

[95] K. Kubota, H. Matsumoto, H. Shindo, S. Shingubara, and Y. Horiike, Japan. J. Appl. Phys. **34**, 2119 (1995).

[96] T. Ono, R. Hamasaki, and T. Mizutani, *Proceedings of 17th Dry Process Symposium* (The Institute of Electrical Engineers of Japan, Tokyo, 1995), p. 219.

[97] T. Ono, R. Hamasaki, and T. Mizutani, Japan. J. Appl. Phys. **33**, L1717 (1994).

[98] T. Ono, R. Hamasaki, and T. Mizutani, Japan. J. Appl. Phys. **35**, 2468 (1996).

[99] G-L. Liu, I. Aikawa, T. Koseki, N. Ikegami, H. Uchida, N. Hirashita, and J. Kanamori, *Proceedings of 19th Dry Process Symposium* (The Institute of Electrical Engineers of Japan, Tokyo, 1997), p. 373.

[100] N. Ikegami, A. Yabata, G-L. Liu, H. Uchida, N. Hirashita, and J. Kanamori, Japan. J. Appl. Phys. **37**, 2337 (1998).

[101] Y. Feurprier, M. Ogata, M. Ozawa, T. Kikuchi, Y. Chinzei, H. Shindo, T. Ichiki, and Y. Horiike, *Proceedings of 20th Dry Process Symposium* (The Institute of Electrical Engineers of Japan, Tokyo, 1998), p. 9.

[102] Y. Feurprier, Y. Chinzei, M. Ogata, T. Kikuchi, M. Ozawa, T. Ichiki, and Y. Horiike, J. Vac. Sci. Technol. A **17**, 1556 (1999).

[103] N. Negishi, M. Miyake, K. Yokogawa, M. Oyama, T. Kanekiyo, and M. Izawa, J. Vac. Sci. Technol. B, **35**, 051205 (2017).

[104] K. Yonekura, S. Sakamori, T. Yokoi, N. Fujiwara, and H. Miyatake, *Proceedings of 19th Dry Process Symposium* (The Institute of Electrical Engineers of Japan, Tokyo, 1997), p. 367.

[105] K. Yonekura,M. Kiritani, S. Sakamori, T. Yokoi, N. Fujiwara, and H. Miyatake, Japan. J. Appl. Phys. **37**, 2314 (1998).

[106] K. Yonekura, T. Katayama, T. Maruyama, N. Fujiwara, and H. Miyatake, *Proceedings of 20th Dry Process Symposium* (The Institute of Electrical Engineers of Japan, Tokyo, 1998), p. 257.

[107] K. Yonekura, T. Katayama, T. Maruyama, N. Fujiwara, and H. Miyatake, J. Vac. Sci. Technol. A **18**, 176 (2000).

[108] S. Soda, T. Shinmura, M. Koyanagi, K. Hane, and S. Samukawa, *Proceedings of 24th Dry Process Symposium* (The Institute of Electrical Engineers of Japan, Tokyo, 2002), p. 281.

[109] Y. Suzuki, T. Shinmura, M. Koyanagi, K. Hane, and S. Samukawa, *Proceedings of 25th Dry Process Symposium* (The Institute of Electrical Engineers of Japan, Tokyo, 2003), p. 265.

[110] T. Shinmura, S. Soda, S. Samukawa, M. Koyanagi, and K. Hane, J. Vac. Sci. Technol. B **20**, 2346 (2002).

[111] T. Shinmura, S. Soda, S. Samukawa, M. Koyanagi, and K. Hane, J. Vac. Sci. Technol. B **22**, 533 (2002).

[112] T. Shinmura, Y. Suzuki, S. Soda, S. Samukawa, M. Koyanagi, and K. Hane, J. Vac. Sci. Technol. A **22**, 433 (2004).

[113] M. Izawa, K. Yokogawa, S. Yamamoto, N. Negishi, Y. Momonoi, K. Tsujimoto, and S. Tachi, *Proceedings of 21st Dry Process Symposium* (The Institute of Electrical Engineers of Japan, Tokyo, 1999), p. 291.

[114] N. Negishi, M. Izawa, K. Yokogawa, Y. Momonoi, T. Yoshida, K. Nakaune, H. Kawahara, M. Kojima, K. Tsujimoto, and S. Tachi, *Proceedings of 22nd Dry Process Symposium* (The Institute of Electrical Engineers of Japan, Tokyo, 2000), p. 31.

[115] K. Yonekura, H. Matsuo, N. Fujiwara, and H. Miyatake, *Proceedings of 23rd Dry Process Symposium* (The Institute of Electrical Engineers of Japan, Tokyo, 2001), p. 285.

[116] M. Miyake, N. Negishi, M. Izawa, K. Yokogawa, M. Oyama, and T. Kanekiyo, *Proceedings of 30th Dry Process Symposium* (Japanese Society of Applied Physics, Tokyo, 2008), p. 275.

[117] M. Miyake, N. Negishi, M. Izawa, K. Yokogawa, M. Oyama, and T. Kanekiyo, Japan. J. Appl. Phys. **48**, 08HE01 (2009).

[118] S. Y. Son, C. H. Shin, Y. J. Kim, G. J. Min, C. J. Kang, and H. K. Cho, *Proceedings of 26th Dry Process Symposium* (The Institute of Electrical Engineers of Japan, Tokyo, 2004), p. 77.

[119] N. Negishi, H. Takesue, M. Sumiya, T. Yoshida, and M. Izawa, *Proceedings of 25th Dry Process Symposium* (The Institute of Electrical Engineers of Japan, Tokyo, 2003), p. 287.

[120] N. Negishi, H. Takesue, M. Sumiya, T. Yoshida, Y. Momonoi, and M. Izawa, J. Vac. Sci. Technol. B **23**, 217 (2005).

[121] S. C. Park, S. Lim, C. H. Shin, G. J. Min, C. J. Kang, H. K. Cho, and J. T. Moon, *Proceedings of 27th Dry Process Symposium* (Japanese Society of Applied Physics, Jeju Korea, 2005), p. 5.

[122] D. Kim, E. Hudson, D. Cooperberg, E. Edelberg, and M. Srinivasan, *Proceedings of 27th Dry Process Symposium* (Japanese Society of Applied Physics, Jeju Korea, 2005), p. 241.

[123] D. Kim, E. Hudson, D. Cooperberg, E. Edelberg, and M. Srinivasan, Thin Solid Film **515**, 4874 (2007).

[124] H. Tanaka, M. Kido, K. Yahashi, M. Oomura, R. Katsumata, M. Kito, Y. Fukuzumi, M. Sato, Y. Nagata, Y. Matsuoka, Y. Iwata, H. Aochi, and A. Nitayama, Symp. VLSI Technol. Dig. Tech. Pap., 2007, p. 14.

[125] Y. Fukuzumi, R. Katsumata, M. Kito, M. Kido, M. Sato, H. Tanaka, Y. Nagata, Y. Matsuoka, Y. Iwata, H. Aochi, and A. Nitayama, IEDM Tech. Dig., 2007, p. 449.

[126] R. Katsumata, M. Kito, Y. Fukuzumi, M. Kido, H. Tanaka, Y. Komori, M. Ishiduki, J. Matsunami, T. Fujiwara, Y. Nagata, Z. Li, Y. Iwata, R. Kirisawa, H. Aochi, and A. Nitayama, Symp. VLSI Technol. Dig. Tech. Pap., 2009, p. 136.

[127] W. Kim, S. Choi, J. Sung, T. Lee, C. Park, H. Ko, J. Jung, I. Yoo, and Y. Park, Symp. VLSI Technol. Dig. Tech. Pap., 2009, p. 188.

[128] H.-T. Lue, T.-H. Hsu, Y.-H. Hsiao, S. P. Hong, M. T. Wu, F. H. Hsu, N. Z. Lien, S.-Y. Wang, J.-Y. Hsieh, L.-W. Yang, T. Yang, K.-C. Chen, K.-Y. Hsieh, and C.-Y. Lu, Symp. VLSI Technol. Dig. Tech. Pap., 2010, p. 131.

[129] C.-P. Chen, H.-T. Lue, K.-P. Chang, Y.-H. Hsiao, C.-C. Hsieh, S.-H. Chen, Y.-H. Shih, K.-Y. Hsieh, T. Yang, K.-C. Chen, and C.-Y. Lu, Symp. VLSI Technol. Dig. Tech. Pap., 2012, p. 91.

[130] J. Jang, H. Kim, W. Cho, H. Cho, J. Kim, S. I. Shim, Y. Jang, J. Jeong, B. Son, D. W. Kim, K. Kim, J. Shim, J. S. Lim, K. Kim, S. Y. Yi, J. Lim, D. Chung, H. Moon, S. Hwang, J. Lee, Y. Son, U. Chung, and W. Lee, Symp. on VLSI Technol. Tech. Dig., pp. 192-193 (2009).

[131] S. Whang, K. Lee, D. Shin, B. Kim, M. Kim, J. Bin, J. Han, S. Kim, B. Lee, Y. Jung, S. Cho, C. Shin, H. Yoo, S. Choi, K. Hong, S. Aritome, S. Park, and S. Hong, IEDM Tech. Dig., 2010, p. 668.

[132] S. H. Chen, H. T. Lue, Y. H. Shih, C. F. Chen, T. H. Hsu, Y. R. Chen, Y. H. Hsiao, S. C. Huang, K. P. Chang, C. C. Hsieh, G. R. Lee, A. T. H. Chuang, C. W. Hu, C. J. Chiu, L. Y. Lin, H. J. Lee, F. N. Tsai, C. C. Yang, T. Yang, and C. Y. Lu, IEDM Tech. Dig., 2012, p. 21.

[133] A. Goda and K. Parat, IEDM Tech. Dig., 2012, p. 13.

[134] H. Lue, T. Hsu, C. Wu, W. Chen, T. Yeh, K. Chang, C. Hsieh, P. Du, Y. Hsiao, Y. Jiang, G. Lee, R. Lo, Y. Su, C. Huang, S. Lai, L. Liang, C. Chen, M. Hung, C. Hu, C. Chiu, and C. Lu, IEDM

Tech. Dig., 2015, p. 44.
[135] K. Parat and C. Dennison, IEDM Tech. Dig., 2015, p. 48.
[136] M. A. Vyvoda, H. Lee, M. V. Malyshev, F. P. Klemens, M. Cerullo, V. M. Donnelly, D. B. Graves, A. Kornblit, and J. T. C. Lee, J. Vac. Sci. Technol. A 16 [6], 3247 (1998).
[137] N. R. Rueger, J. J. Beulens, M. Schaepkens, M. F. Doemling, J. M. Mirza, T. E. F. M. Standaert, and G. S. Oehrlein, J. Vac. Sci. Technol. A 15 [4], 1881 (1997).
[138] D. R. Sparks, J. Electrochem. Soc. 139 [6], 1736 (1992).
[139] Z. Yang, F. H. Hsu, L. Y. Lin, H. J. Lee, N. T. Lian, T. Yang, K. C. Chen, and C. Y. Lu, Advanced Semiconductor Manufacturing Conf. (ASMC), 2013, p. 24.
[140] T. Iwase, K. Yokogawa, T. Arase, A. Hirata, M. Mori, Symp. on SPIE Advanced Lithography Technical Summary, 2015, p. 160.
[141] C. M. Huard et al., J. Vac. Sci. Technol. A 35 (5), 05C301 (2017).

2. Demonstration of High-Aspect-Ratio Multilayer Etching in HBr/CH_3F-based Gas Plasmas with N_2 Gas Addition

2.1 Introduction

The integration of semiconductor devices for the next-generation nodes of logic and memory presents enormous challenges for etching; current planar flash memory devices in particular face critical scaling limitations.[1-3] Three-dimensional (3D) NAND device fabrication has been improved in manufacturing fabs for the flash memory market by perpendicular integration.[4-8] A 3D NAND device structure was realized by fabricating holes in stacked layers in which polycrystalline silicon (poly-Si) forming electrodes and a SiO_2 insulator were alternately deposited.[9-14]

In 3D NAND fabrication, it is difficult to form extremely high-aspect-ratio holes through over 30 stacked film layers with both a vertical profile and high throughput. By using, for example, a known technology, we can apply a cyclic process in which etching SiO_2 with fluorocarbon-based gas is alternated with etching poly-Si with HBr gas.[15-18] However, this alternating process has a disadvantage in terms of throughput because a multiple-step process needs additional time for residual gases to be exhausted and for pressure to stabilize before the next etching step. Thus, a single-step etching process under unique conditions could be a promising technology for obtaining a high throughput, although a novel process and hardware must be developed in the future to fully realize this process. In our previous study, one piece of hardware, an etching reactor that can etch both poly-Si and SiO_2 materials, was developed.[19]

In this paper, we report on the development of an etching process for fabricating vertical holes through poly-Si/SiO_2 stacks for 3D-NAND technology. A gas mixture of HBr and fluorocarbon was used for obtaining quite similar poly-Si and SiO_2 etching rates to realize a single-step etching process. The material composition on the surface was estimated using a simulation program to investigate gas chemistry. The composition was also analyzed by XPS to confirm the simulation results. Finally, the obtained etching profile was evaluated to reveal the etching process.

2.2 Experimental procedure

Stacked films with a hole pattern were fabricated for profile evaluation. Figure 1 shows a cross-sectional SEM image and a schematic image of a sample for profile evaluation. Eight pairs of 50-nm-thick poly-Si and SiO_2 layers were alternately deposited on a Si substrate. An 800-nm-thick amorphous carbon layer (ACL) was deposited as an etching mask on the poly-Si/SiO_2 stacks, and 50-nm-thick SiON was deposited as a mask for the 800-nm-thick ACL. 50-nm-diameter holes were patterned in a 120-nm-thick resist film coated on the SiON layer by the electron beam lithography method.

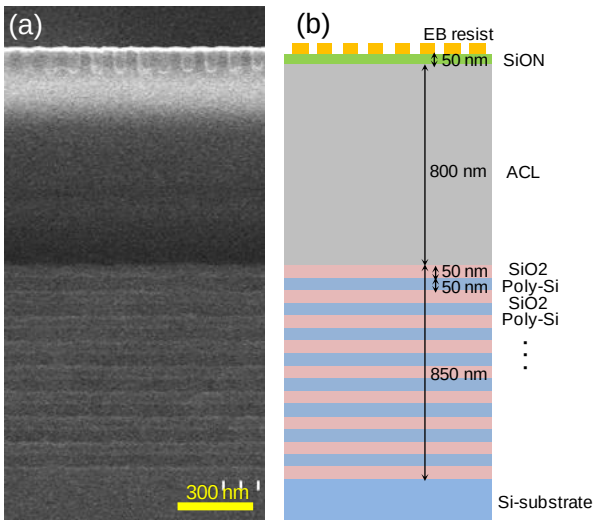

Fig. 1. (a) Cross-sectional SEM image, (b) schematic image of etching profile evaluation sample.

The stacked film samples were processed using a parallel-plate etching reactor supplied with 200 MHz VHF power to generate HBr/fluorocarbon-based gas plasma. Chamber wall sputtering and plasma diffusion can be suppressed by a 200 MHz discharge effect.[20, 21] Figure 2 shows a schematic of the reactor. The gas inlet under the upper electrode in the reactor was made of a dielectric material that can withstand a corrosive gas. The VHF source power and wafer bias power were applied at 1000 and 1200 W, respectively. The process pressure was controlled at 6.0 Pa. The wafer temperature was controlled on an electrostatic chuck stage between 10 to 60°C using a circulator system. The sample for profile evaluation were divided into 20-mm-square pieces and pasted with grease on 300 mm wafers coated with a photoresist (PR). In an ancillary experiment, PR

was selected as the base wafer for coupon evaluation in terms of etching rate and profile. The carbon by-product during ACL mask etching might be similar to carbon in PR.

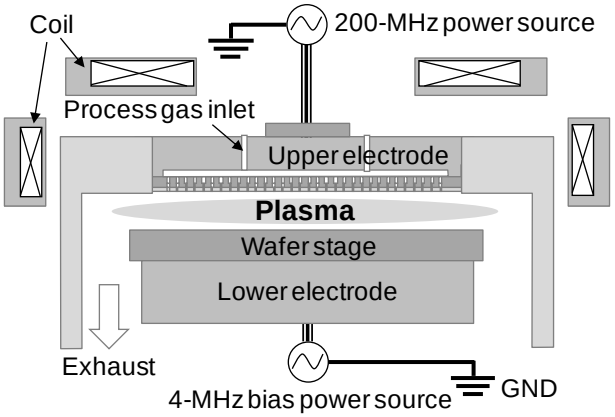

Fig. 2. Schematic of parallel-plate etching reactor. The reactor has a 200 MHz VHF plasma source and a 4 MHz wafer bias generator. The gas inlet in the upper electrode is made of a dielectric material that withstands corrosive gas.

For processing, cross-sectional images were obtained by field-emission SEM (Hitachi S-5200). Etching rate was evaluated using blanket wafers deposited with poly-Si, SiO_2, or PR. Film thickness was measured using an optical film-thickness meter (Nanometrics Nanospec 6100). The composition of the sample surface was analyzed by XPS. 20-mm-square coupons of poly-Si, SiO_2, and PR were pasted on the PR-coated 300 mm wafers. These samples were processed in the reactor under the same conditions as the profile evaluation ones. The surface composition was estimated by peak deconvolution of XPS spectra.

The equilibrium composition was simulated using the software “HSC chemistry” (HSC) made by Outotec Research Oy. to investigate the possible materials produced when several gas species were mixed. HSC can calculate the composition of equilibrium state materials by the Gibbs energy minimization method. The following were the initial conditions: pressure, 6 Pa; temperature, 25°C; and mol numbers of HBr and fluorocarbon, 13 and 19 kmol, respectively. Note that there were ions and radicals besides gas molecules in the etching reactor because part of the mixture of gases was discharged at the 200 MHz VHF power. Therefore, HSC might not completely simulate an actual situation; however, the HSC results could be used to determine the materials that tended to be generated.

2.3 Results and discussion

2.3.1 Gas mixing for continuous etching process

Figure 3 shows the dependence of the poly-Si and SiO_2 etching rates (ERs) on the HBr to fluorocarbon gas mixing ratio at a wafer temperature of 60°C. The total gas-flow rate was set to be constant at 300 ml/min. Poly-Si ER increased when the HBr ratio was high, and SiO_2 ER increased when the fluorocarbon ratio was high because fluorocarbon radicals might have impeded the etching of poly-Si. This result indicates that the ERs of poly-Si and SiO_2 can be made almost equal when the HBr ratio is 0.40.

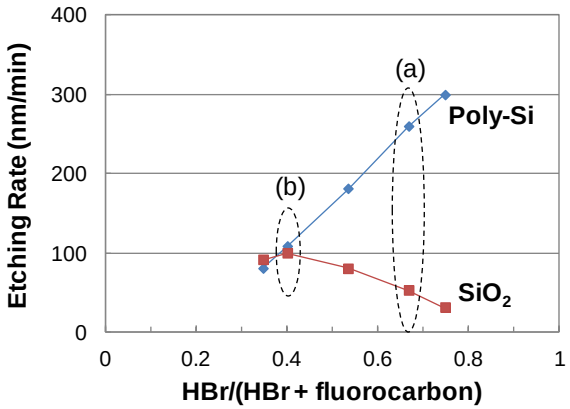

Fig. 3. Dependence of poly-Si and SiO_2 etching rates on HBr and fluorocarbon gas mixing ratio. (a) and (b) indicate HBr mixing ratios of 0.67 and 0.40, respectively.

Next, the relationship between the etching profile of the poly-Si/SiO_2 stacks and the poly-Si and SiO_2 ERs was investigated (shown in Fig. 4). When an HBr ratio of 0.67 was applied, side etching progressed in the poly-Si layer because the poly-Si ER is higher than that of SiO_2. However, a smooth side wall was obtained when an HBr ratio of 0.40 was applied, but the bottom profile was tapered. The tapering might have been caused by excessive amount of carbon(C)-based polymers sticking onto the side wall, which inhibits spontaneous etching because HBr/fluorocarbon plasma could have generated a C_xF_y and/or C_zH_u (here, x, y, z, u are integers) polymer. Generally, the sticking of C-based polymers is controlled by addiing O_2 gas for high-aspect-ratio-contact (HARC) etching, but O_2 addition decreases the etching selectivity of an ACL mask. According to previous studies, if a C-based polymer formed $C_xN_yF_zH_u$ by combining with nitrogen (N) and

hydrogen (H), a carbon on a surface can be easily removed by high volatility of by-product, e.g. HCN.[22, 23] A vertical profile may be obtained by bottom etching progression without side etching progression because the sticking $C_xN_yF_zH_u$ polymer may act as a protective film.

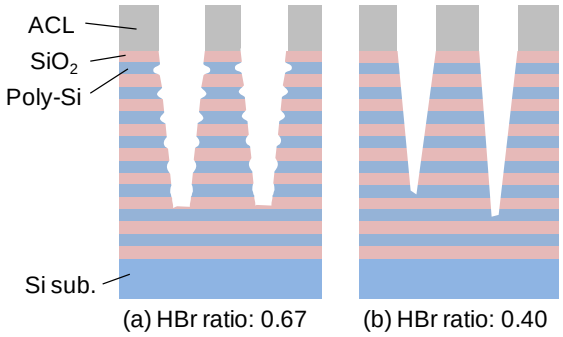

Fig. 4. Schematic of cross-sectional etching profile. Holes were fabricated in poly-Si/SiO_2 stacks when the (a) HBr mixing ratios were 0.67 (b) and 0.40.

2.3.2 Equilibrium simulation with additional gas

We simulated chemical equilibrium by using HSC to determine a combination of N and H that would result in their stable existence on the surface by gas addition. It was found that N_2 gas addition may result in the generation of an ammonium salt. Figure 5 shows the simulation result for the N_2 gas amount dependence on material concentration at a temperature of 25°C. The concentration of ammonium bromine (NH_4Br) increased as HBr and methane (CH_4) decreased after N_2 flow addition. It is promising that N and H existed stably on the surface because ammonium bromine is solid at room temperature. Figure 6 shows the simulation result for the temperature dependence on material concentration with N_2 addition. The figure shows that ammonium bromine tended to be produced at a low temperature. The concentration of ammonium bromine decreased as the temperature increased, while a steady state existed at approximately 20 to 50°C.

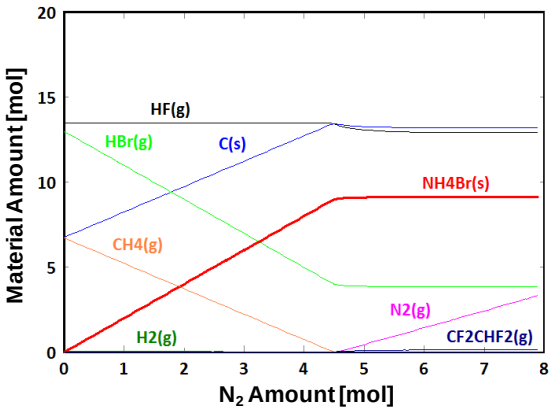

Fig. 5. N_2 gas amount dependence on material amount calculated by chemical equilibrium simulation. The temperature was 25°C and the pressure was 6.0 Pa. (g) and (s) indicate vapor phase and solid phase, respectively.

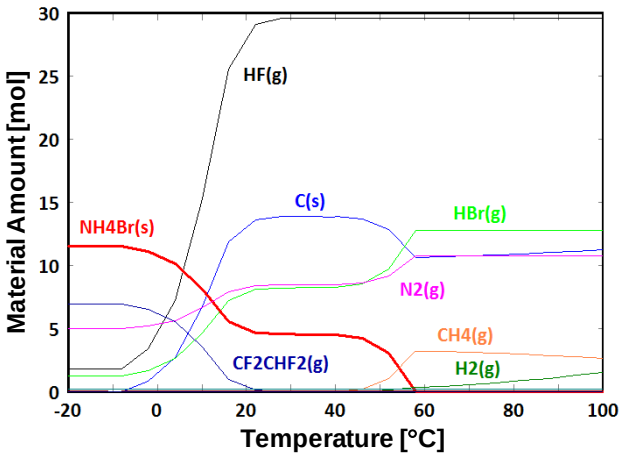

Fig. 6. Temperature dependence on material amount with N_2 addition calculated by chemical equilibrium simulation. (g) and (s) indicate the vapor phase and solid phase, respectively.

2.3.3 Surface composition dependence on-wafer temperature

The surface compositions of the by-products or a mixing layer processed at a high wafer temperature of 60°C and a low wafer temperature of 20°C were examined by XPS analysis. First, the samples were processed without applying a wafer bias to separate molecular or radical adsorption from ion-assisted reaction. XPS narrow scan spectra of N 1s and Br 3d peaks were measured to determine the chemical bonding of elements on the surface.

Figure 7 shows the relationship between wafer temperature and XPS spectra. N 1s spectra were deconvoluted into two contributions, one due to N-C nitrogen (detected at 399.8 eV) and the other to N-H nitrogen (detected at 401.3 eV).[24, 25] Br 3d spectra were deconvoluted into two contributions, one due to Br or Br^- bromine (detected at 68.8 eV) and the other to Br-C bromine (detected at 70.5 eV).[26] The intensity of the Br or Br^- peaks and N-H peak increased at the low wafer temperature of 20°C. By comparing between results of the chemical equilibrium simulation and the XPS analysis without wafer bias, we found that these results corresponded roughly. It is reasonable to suppose that the concentrations of N-H and Br on the surface at a low wafer temperature were caused by the formation of ammonium bromine. Therefore, these results indicate that N, H, and Br can exist stably on the surface at a low wafer temperature.

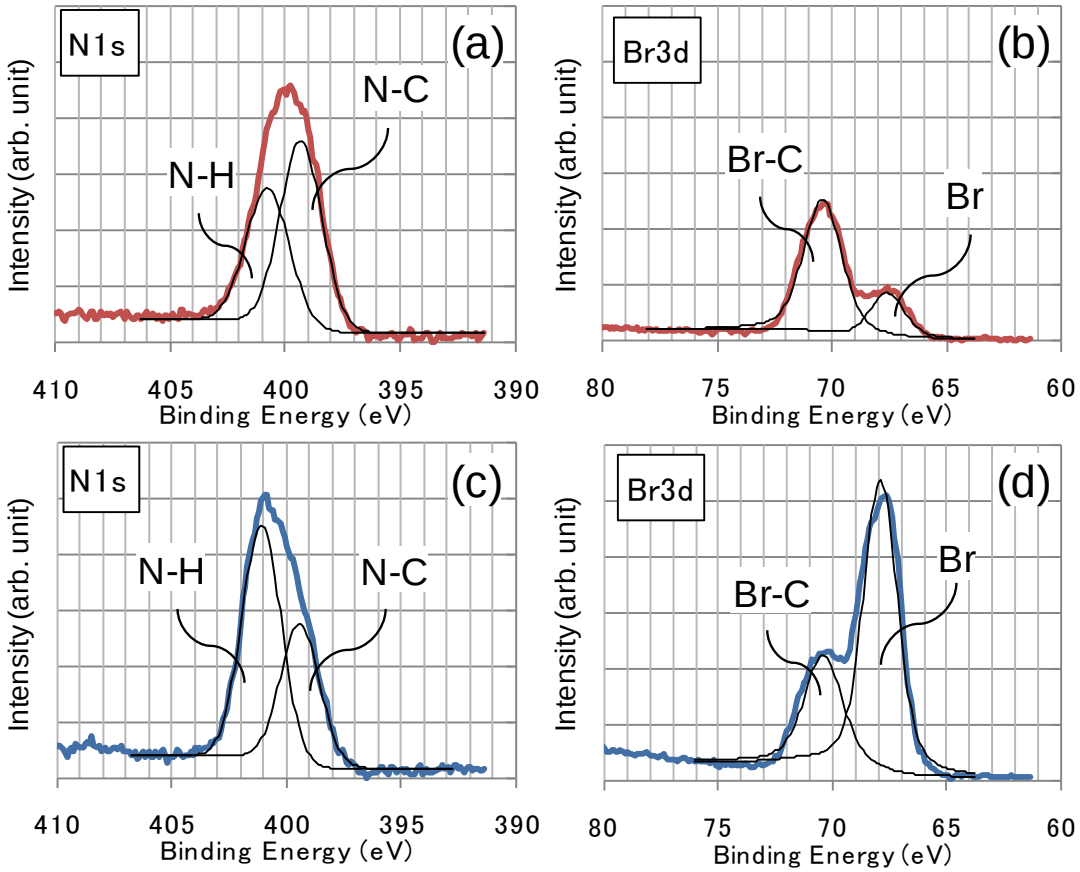

Fig. 7. XPS narrow scan using poly-Si sample without applying wafer bias. (a) N 1s peak at wafer temperature of 60°C, (b) Br 3d peak at 60°C, (c) N 1s peak at 20°C, and (d) Br 3d peak at 20°C. These spectra were deconvoluted (shown as black solid curved line).

Next, high-energy ions were irradiated by applying a wafer bias to confirm whether N, H, and Br are volatilized by chemical reaction on the surface. Figure 8 shows the XPS spectra of N 1s and Br 3d peaks when a wafer bias was applied at a wafer temperature of 20°C. The Br and N-H peaks almost disappeared when high-energy ions were irradiated. Here, the C-based polymer thicknesses at wafer temperatures of 20 and 60°C, which were estimated from the C 1s peak intensity of the XPS spectra, were 2.2 and 2.5 nm, respectively. Therefore, N, H, and Br might have been volatilized with the C-based polymer by high-energy-ion irradiation.

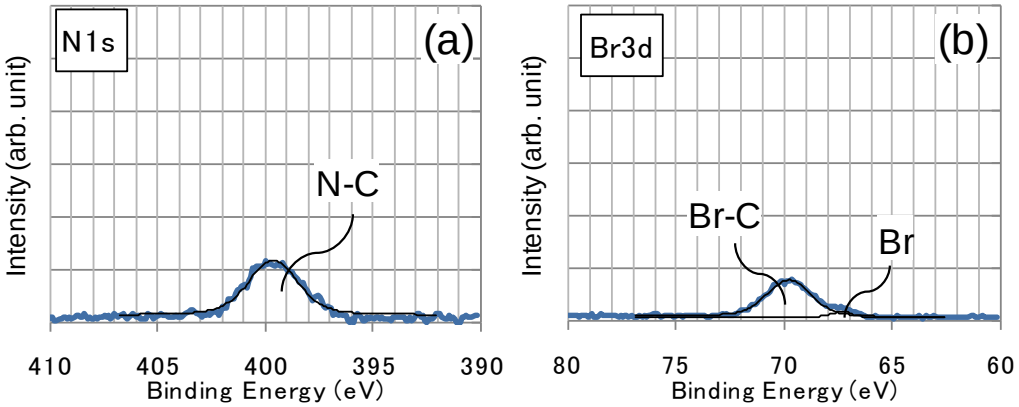

Fig. 8. XPS narrow scan using poly-Si sample with wafer bias applied. (a) N 1s peak, (b) Br 3d peak at wafer temperature of 20°C. These spectra were deconvoluted (shown as black solid curved line).

2.3.4 Etching profile evaluation

We evaluated the etching profiles of the poly-Si/SiO_2 stacks at several wafer temperatures by equilibrium simulation and surface composition analysis. Figure 9 shows cross-sectional SEM images demonstrating the wafer temperature dependence on the etching profile of the stacks. The stacks were etched by N_2/HBr/fluorocarbon plasma through an ACL hole mask. When a wafer temperature of 60°C and 300 s of processing time were applied, the bottom profile of the holes was tapered because there was a large amount of the C-based polymer sticking. However, when a wafer temperature of 20°C and 300 s of processing time were applied, the etching rate was increased owing to the C-based polymer being reduced by existing N, H, and Br. Furthermore, the hole bottom profile differed depending on the wafer temperature; the profile at 20°C showed a flat

bottom, and that at 60°C showed a tapered bottom. By adjusting the wafer temperature to 10°C and processing time to 400 s, a 1.2-μm-depth vertical hole profile with an aspect ratio of 24 was obtained.

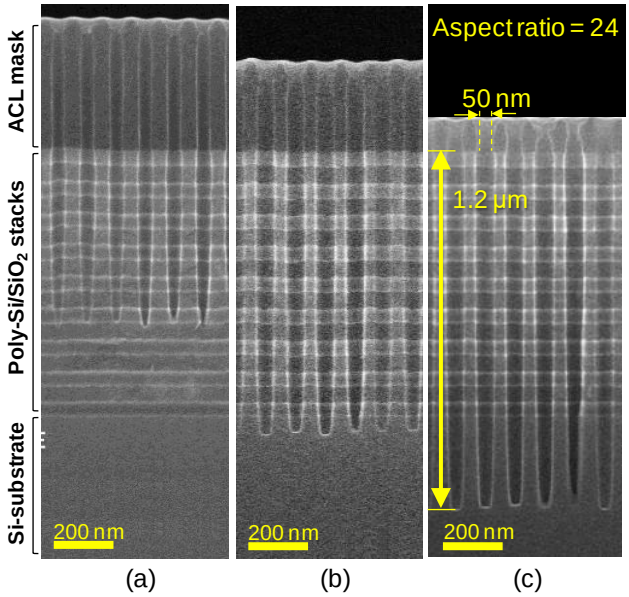

Fig. 9. Cross-sectional SEM image of poly-Si/SiO_2 stack etching profile. (a) 300 s of etching at wafer temperature of 60°C, (b) 300 s of etching at 20°C, (c) 400 s of etching at 10°C.

2.3.5 Modeling a surface reaction

Anisotropic etching of Si in halogen gas plasma can be realized at a decreased wafer temperature owing to the decreased by-product reactivity on the sidewall.[27-29] "Necking" and "bowing" due to SiO_2 etching under fluorocarbon-based gas plasma can be improved with an increased wafer temperature owing to the optimized carbon sticking.[30] Conversely, it was found that there was a quite different temperature dependence between typical SiO_2 etching and poly-Si/SiO_2 etching with N_2-added HBr/fluorocarbon plasma.

A surface reaction model that depends on the wafer temperature was examined considering the surface composition of by-products or mixing layers. At a high wafer temperature of 60°C, it is assumed that a C-based material (by-product or polymer) was deposited in the etched holes because fluorocarbon/HBr plasma and Si generate C-based materials of a low vapor pressure, such as CH_x, CF_x, CBr_x, and SiC_x. The deposited

carbon might have formed a protective layer at the sidewall and caused the tapering of the bottom. In contrast, at a low wafer temperature of 20°C, N-H and Br existed on the Si surface, as shown in Fig. 7. It is considered that N-H and Br are present in the deposition layer. N-H could have volatilized excessive amount of carbon in the deposition layer that changed to hydrogen cyanide or carbon nitride. Br contained in the deposition layer could have enhanced the etching of Si. The deposited carbon on the sidewall may form a thin protective layer since the sidewall is also exposed by ion irradiation; therefore, it is considered that the vertical profile has been improved. The chemical reaction between Si and Br may not proceed efficiently without a high-energy-ion impact because the activation energy of $SiBr_4$ is higher than that of carbon nitride. The chemical reaction between Si and Br contained in the deposition layer might not proceed efficiently in the sidewall because a low incident-angle ion provides less energy. Conversely, the chemical reactions of Si-Br and C-N might have been enhanced in the hole bottom by a high incident-angle ion; therefore, it is considered that etching rate has been increased. The surface reaction model can explain the temperature dependence on the etching profile. It is reasonable to suppose that the vertical profile is obtained by the formation of a reactive surface reaction layer that contains N, H, and Br at a low wafer temperature.

2.4 Conclusion

We investigated the effect of wafer temperature on the etching profile of high-aspect-ratio holes in poly-Si/SiO_2 stacks by analyzing surface reaction layers. HBr/ fluorocarbon-based gas plasma was used to achieve a single-step etching process to improve the throughput of the process. XPS results revealed that the N-H and Br adsorption on the surface was enhanced at a low wafer temperature of 20°C, which results in a reduced thickness of the C-based layer because N-H enhances the generation of the HCN by-product. The stability of NH_4Br at a lower temperature was also examined by chemical equilibrium simulation. Finally, vertical holes with an aspect ratio of 24 were obtained at a wafer temperature of 10°C using this single-step process.

References

[1] S. Bangsaruntip, G. M. Cohen, A. Majumdar, Y. Zhang, S. U. Engelmann, N. C. M. Fuller, L. M. Gignac, S. Mittal, J. S. Newbury, M. Guillorn, T. Barwicz, L. Sekaric, M. M. Frank, and J. W. Sleight, IEDM Tech. Dig., 2009, p. 297.

[2] A. Veloso, S. Demuynck, M. Ercken, A. M. Goethals, S. Locorotondo, F. Lazzarino, E. Altamirano, C. Huffman, C. Delvaux, B. Baudemprez, T. Vandeweyer, F. Van Roey, C. Baerts, D. Goossens, H. Dekkers, P. Ong, N. Heylen, K. Kellens, H. Volders, A. Hikavyy, C. Vrancken, M. Rakowski, S. Verhaegen, M. Dusa, L. Romijn, C. Pigneret, A. Van Dijk, R. Schreutelkamp, A. Cockburn, V. Gravey, H. Meiling, B. Hultermans, S. Lok, K. Shah, R. Rajagopalan, J. Gelatos, O. Richard, H. Bender, G. Vandenberghe, G. P. Beyer, P. Absil, T. Hoffmann, K. Ronse, and S. Biesemans, IEDM Tech. Dig. , 2009, p. 301.

[3] A. Veloso, A. De Keersgieter, S. Brus, N. Horiguchi, P. P. Absil, and T. Hoffmann, Jpn. J. Appl. Phys. **50**, 04DC16 (2011).

[4] H. Tanaka, M. Kido, K. Yahashi, M. Oomura, R. Katsumata, M. Kito, Y. Fukuzumi, M. Sato, Y. Nagata, Y. Matsuoka, Y. Iwata, H. Aochi, and A. Nitayama, Symp. on VLSI Technology Digest of Technical Papers, 2007, p. 14.

[5] R. Katsumata, M. Kito, Y. Fukuzumi, M. Kido, H. Tanaka, Y. Komori, M. Ishiduki, J. Matsunami, T. Fujiwara, Y. Nagata, Z. Li, Y. Iwata, R. Kirisawa, H. Aochi, and A. Nitayama, Proc. Symp. VLSI Technol., 2009, p. 136.

[6] Y. Kim, J.-G. Yun, S. H. Park, W. Kim, J. Y. Seo, M. Kang, K.-C. Ryoo, J.-H. Oh, J.-H. Lee, H. Shin, and B.-G. Park, IEEE Trans. Electron Devices **59** [1], 35 (2011).

[7] E. Choi and S. Park, IEDM Tech. Dig., pp. 211-214 (2012).

[8] Y. Hsiao, H. Lue, W. Chen, B. Tsui, K. Hsieh, and C. Lu, IEEE Electron Devices Lett. **36** [10], 1015 (2015).

[9] H. T. Lue, T. H. Hsu, Y. H. Hsiao, S. P. Hong, M. T. Wu, F. H. Hsu, N. Z. Lien, S. Y. Wang, J. Y. Hsieh, L. W. Yang, T. Yang, K. C. Chen, K. Y. Hsieh, and C. Y. Lu, Symp. on VLSI Technology Digest of Technical Papers, 2010, p. 131.

[10] S. Whang, K. Lee, D. Shin, B. Kim, M. Kim, J. Bin, J. Han, S. Kim, B. Lee, Y. Jung, S. Cho, C. Shin, H. Yoo, S. Choi, K. Hong, S. Aritome, S. Park, and S. Hong, IEDM Tech. Dig., 2010, p. 668.

[11] S. H. Chen, H. T. Lue, Y. H. Shih, C. F. Chen, T. H. Hsu, Y. R. Chen, Y. H. Hsiao, S. C. Huang, K. P. Chang, C. C. Hsieh, G. R. Lee, A. T. H. Chuang, C. W. Hu, C. J. Chiu, L. Y. Lin, H. J. Lee, F. N. Tsai, C. C. Yang, T. Yang, and C. Y. Lu, IEDM Tech. Dig., 2012, p. 21.

[12] A. Goda and K. Parat, IEDM Tech. Dig., 2012, p. 13.

[13] H. Lue, T. Hsu, C. Wu, W. Chen, T. Yeh, K. Chang, C. Hsieh, P. Du, Y. Hsiao, Y. Jiang, G. Lee, R. Lo, Y. Su, C. Huang, S. Lai, L. Liang, C. Chen, M. Hung, C. Hu, C. Chiu, and C. Lu, IEDM Tech. Dig., 2015, p. 44.

[14] K. Parat and C. Dennison, IEDM Tech. Dig., 2015, p. 48.
[15] M. A. Vyvoda, H. Lee, M. V. Malyshev, F. P. Klemens, M. Cerullo, V. M. Donnelly, D. B. Graves, A. Kornblit, and J. T. C. Lee, J. Vac. Sci. Technol. A **16** [6], 3247 (1998).
[16] N. R. Rueger, J. J. Beulens, M. Schaepkens, M. F. Doemling, J. M. Mirza, T. E. F. M. Standaert, and G. S. Oehrlein, J. Vac. Sci. Technol. A **15** [4], 1881 (1997).
[17] D. R. Sparks, J. Electrochem. Soc. **139** [6], 1736 (1992).
[18] Z. Yang, F. H. Hsu, L. Y. Lin, H. J. Lee, N. T. Lian, T. Yang, K. C. Chen, and C. Y. Lu, Advanced Semiconductor Manufacturing Conf. (ASMC), 2013, p. 24.
[19] T. Iwase, K. Yokogawa, T. Arase, A. Hirata, M. Mori, Symp. on SPIE Advanced Lithography Technical Summary, 2015, p. 160.
[20] K. Yokogawa, K. Maeda, H. Kobayashi, T. Kanekiyo, and M. Izawa, Proc. 7th Int. Conf. Microelectronics and Interfaces, 2006.
[21] K. Yokogawa, K. Maeda, and M. Izawa, Jpn. J. Appl. Phys. **47**, 6854 (2008).
[22] H. Nagai, S. Takashima, M. Hiramatsu, M. Hori, and T. Goto, J. Appl. Phys. **91**, 2615 (2002).
[23] M. Ooka and S. Yokoyama, Jpn. J. Appl. Phys. **44**, 6476 (2005).
[24] K. Ogata, J. Fernando D. Chubaci, and F. Fujimoto, J. Appl. Phys. **76**, 3791 (1994).
[25] S. Bourbigot, M. Le Bras, L. Gengembre, and R. Delobel, Applied Surface Science **81**, 299 (1994).
[26] AC Brieva, C Jäger, F Huisken, L Šiller, and YV Butenko, Carbon **47**, 2812 (2009).
[27] S. Tachi, K. Tsujimoto, S. Arai, and T. Kure, J. Vac. Sci. Technol. A **9**, 796 (1991).
[28] M. Haverlag, G. S. Oehrlein, and D. Vender, J. Vac. Sci. Technol. B **12**, 96 (1994).
[29] B. Wu, A. Kumar, and S. Pamarthy, J. Appl. Phys. **108**, 051101 (2010).
[30] H. Abe, M. Yoneda, and N. Fujiwara, Jpn. J. Appl. Phys. 47, 1435 (2008).

3. Effect of Temperature on Composition of Deposition Layer in $HBr/N_2/CH_3F$-based Gas Plasmas

3.1 Introduction

Semiconductor device architecture has been changing from being planar to being three-dimensional (3D) because the integration of semiconductor devices has faced a scaling limitation. 3D NAND flash architecture stacks memory cells in an integrated device perpendicularly. Such devices as bit-cost scalable (BiCS) [1-3] and vertical-gate NAND (VG-NAND) [4-6] structures can reduce production costs per memory bit. A 3D NAND flash structure can be achieved by fabricating holes in stacked layers in which polycrystalline silicon (poly-Si) forming electrodes and silicon dioxide (SiO_2) insulators are alternately deposited.[7-11] In the 3D NAND fabrication process, holes with extremely high aspect ratio (> 50) are fabricated through more than 30 stacked film layers with both a high throughput and a vertical profile. A cyclic process, for example, can be used for stacked layer etching, in which etching SiO_2 with fluorocarbon-based gas is alternately performed with etching poly-Si with HBr gas.[12-15] However, this process has a disadvantage in terms of throughput because it requires an additional time to exhaust residual gases and stabilize the pressure before the next etching step. Thus, a single-step etching process under unique conditions could be a promising technology for obtaining a high throughput.

Our previous work demonstrated that a single-step etching process could be achieved by using HBr/N_2/fluorocarbon-based gas plasma to create a vertical hole profile in a poly-Si/SiO_2 stack.[16, 17] HBr and fluorocarbon gas were mixed to uniform etching rates of both poly-Si and SiO_2 to obtain smooth side walls in the holes.[14, 18-21] Furthermore, nitrogen gas was added and the wafer temperature was adjusted to obtain the vertical hole profile. However, a surface reaction mechanism under HBr/N_2/fluorocarbon-based gas plasma has not been investigated yet. A deposition film consisting of a fluorocarbon polymer formed when ions were not irradiated, and a mixing layer (2-3 nm thickness) containing carbon, fluorine, nitrogen, bromine, and substrate material formed under ion bombardment. By XPS analysis, both nitrogen and bromine adsorption increased in the deposition film at a wafer temperature of 20°C as compared

with those at 60°C.[22-24] Increasing the amounts of nitrogen and bromine is possibly a key to investigating the surface reaction mechanism.

In this study, the effects of wafer temperature on etching rate and surface composition were investigated to clarify the surface reaction mechanism under HBr/N_2/fluorocarbon-based gas plasma for developing a process to fabricate 3D NAND devices. Both the etching rates of poly-Si and SiO_2 that depend on-wafer temperature were evaluated under HBr/N_2/fluorocarbon-based gas, fluorocarbon/N_2 mixture gas, and HBr/N_2 mixture gas to separate any gas chemistry effects. To analyze the temperature dependence of surface composition in detail, both thermal desorption spectroscopy (TDS) and laser-sputtered neutral mass spectrometry (laser-SNMS) observations were applied to the deposition films on Si surfaces processed at 20 and 60°C.

3.2 Experimental procedure

Figure 1 shows a schematic of a parallel-plate-type etching reactor. The reactor has a 200 MHz plasma source generator and a 4 MHz wafer bias generator. A gas inlet in the upper electrode is made of a dielectric material to withstand corrosive gases. The coils generate a magnetic field to control plasma the distribution. Chamber wall sputtering and plasma diffusion can be suppressed by using a 200 MHz discharge effect.[25, 26] The process conditions used were as follows. The VHF source and wafer bias powers were set to 1.0 and 1.2 kW, respectively. The process pressure was controlled to 6.0 Pa. The wafer temperature was maintained on an electrostatic chuck stage between 10 and 60 °C using a circulator system. Plasma was generated using HBr/N_2/fluorocarbon-based gas; the generated plasma is the same as that used in the etching process of poly-Si/SiO_2 stacks. Blanket wafers of Si substrates with a poly-Si thin film or a thermally oxidized SiO_2 thin film were used as evaluation samples.

The etching rate was calculated on the basis of the film thicknesses obtained before and after plasma processing. The film thicknesses were measured by using an optical film-thickness meter (Nanometrics: NanoSpec6100). The surface composition was analyzed by TDS (ESCO: EMD-WA1000S/W) and laser-SNMS (Toyama: FILMER). TDS was used to detect desorption gas molecules from the deposition film on the samples. The temperature increase rate of TDS was set to 30°C/min. Laser-SNMS was applied to directly measure parent molecule ions without decomposing materials on a surface.[27, 28]

Laser-SNMS delivers primary ions onto a substrate as a beam, ionizing the flaked neutral particles with a pulsed laser, and separating the particles by mass using a time-of-flight method. A dose amount of 1×10^{12} ions/cm^2 of the primary ion Ga^+ was used. Compared with those observed in the method of detecting secondary ions, the signal intensity is high and the matrix effect is small. Therefore, laser-SNMS is suitable for the mass detection of parent molecular ions.

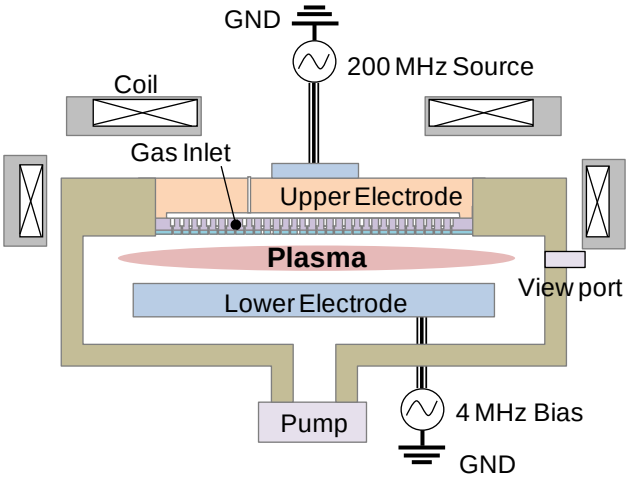

Fig. 1. Schematic of parallel-plate-type etching reactor. The reactor has a 200 MHz plasma source generator and a 4 MHz wafer bias generator. The gas inlet in the upper electrode is made of a dielectric material to withstand corrosive gas. Coils generate a magnetic field to control the plasma distribution.

3.3 Results and discussion

3.3.1 Temperature dependence of etching rate

The effects of the wafer temperature on the etching rate of blanket wafers were investigated to clarify the etching mechanism. Figure 2 shows the wafer temperature dependences of the poly-Si and SiO_2 etching rates under HBr/N_2/fluorocarbon-based gas plasma. The etching rates normalized at 60°C. The temperature dependences indicate that the etching rates of poly-Si and SiO_2 increase as the wafer temperature decreases. Therefore, an increase in the etching depth of hole patterns in our previous work is consistent with increases in poly-Si and SiO_2 etching rates at low temperatures.

Figures 3(a) and 3(b) show the temperature dependences of the poly-Si and SiO_2

etching rates under fluorocarbon/N_2 and HBr/N_2 mixture gas plasmas, respectively. Process conditions such as gas pressure, total flow rate, source power, and bias power are the same as those in Fig. 2. Figure 3(a) shows that the poly-Si etching rate slightly increases and the SiO_2 etching rate clearly increases as the temperature decreases under fluorocarbon/N_2 mixture gas plasma. Generally, the sticking probability of atoms, molecules, and radicals in the gas phase is one of the causes of the temperature dependence of the etching rate because the sticking probability increases as temperatures decrease.

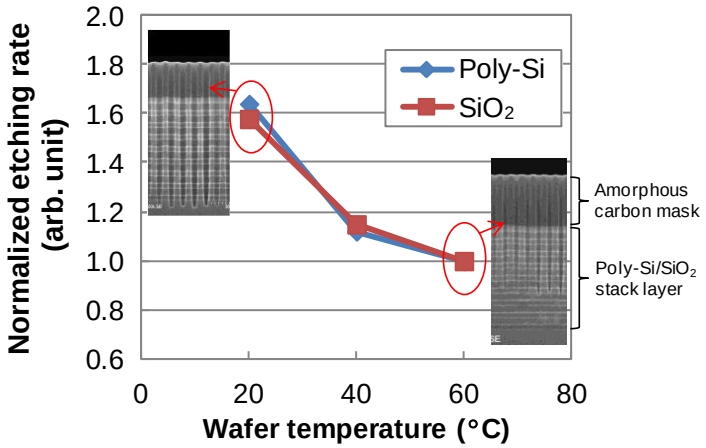

Fig. 2. Temperature dependences of poly-Si and SiO_2 etching rates under HBr/N_2/fluorocarbon-based gas plasma with applied wafer bias. Etching rates are normalized at 60°C.

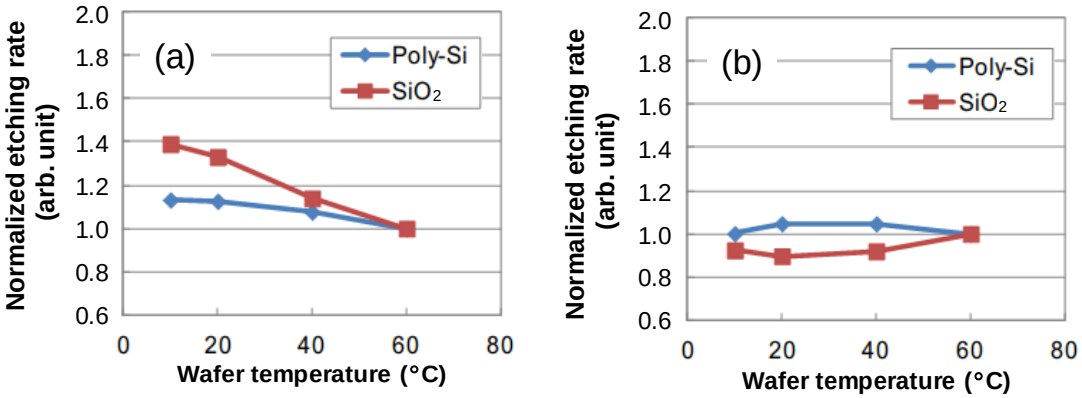

Fig. 3. Temperature dependences of poly-Si and SiO_2 etching rate under (a) fluorocarbon/N_2 and (b) HBr/N_2 gas plasmas with applied wafer bias. Etching rates are normalized at 60°C.

Under for consistency fluorocarbon/N_2 mixture gas plasma, a fluorocarbon polymer film, which acts as an etchant when high-energy ions are bombarded, is deposited on a poly-Si or SiO_2 surface.[13] The increase in SiO_2 etching rate is possibly due to the increase in the amount of the etchant used, since the amount of deposited fluorocarbon polymer increases at low temperatures.[29] Conversely, the poly-Si etching rate hardly increases because carbon in the fluorocarbon polymer is not volatilized owing to a reaction where Si and CF_2 become SiF_4 and carbon, respectively. Figure 3(b) shows that both the etching rates of poly-Si and SiO_2 remain approximately constant with the wafer temperature under HBr/N_2 mixture gas plasma. This gas chemistry would generate etchants of HBr, Br, and Br_2. It is assumed that the radicals adsorbed on the poly-Si and SiO_2 surfaces saturate at any temperature when both the poly-Si and SiO_2 etching rates remain approximately constant with the wafer temperature.[30]

As a result of the gas chemistry investigation, the temperature dependence of the SiO_2 etching rate under HBr/N_2/fluorocarbon-based gas plasma could be relevant to the sticking probability of the fluorocarbon polymer. However, the temperature dependence of the poly-Si etching rate under HBr/N_2/fluorocarbon-based gas plasma could be caused by factors besides the sticking probability because the etching rate did not increase at low temperatures. Thus, a surface reaction must be evaluated on the basis of the temperature dependence of surface composition in detail to determine the cause of the temperature dependence of poly-Si etching rate.

3.3.2 Surface composition analysis

The effects of wafer temperature on surface composition were investigated to clarify the etching mechanism. The TDS spectra of multiple mass-to-charge ratios (*m/z*) up to a heating temperature of 400°C are shown in Fig. 4, where a TDS analysis was applied to a silicon surface with a 50-nm-thick deposition film layer formed under HBr/N_2/fluorocarbon-based gas plasma at wafer temperatures of (a) 60 and (b) 20°C. The spectra of *m/z* = 1, 17, 18, 80, and 97 in Fig. 4 contain H, NH_3, H_2O, HBr, and NH_4Br, respectively. In practical terms, *m/z* = 17 contains both NH_3 and OH; therefore, OH was eliminated by estimation from the fragment ratio (0.26) of the H_2O (*m/z* = 18) intensity. Figure 4(a) shows that the signals of *m/z* = 1 (H) and 18 (H_2O) increase gradually, and those of *m/z* = 17 (NH_3) and 80 (HBr) have desorption peaks at about 270 and 330°C,

respectively. The signals of *m/z* = 1 (H), 17 (NH_3), 80 (HBr), and 97 (NH_4Br) show the same desorption peak at approximately 260°C [Fig. 4(b)]. However, the signal of *m/z* = 80 (HBr) shows a second peak at about 330°C. A peak in the signal of *m/z* = 97 (NH_4Br) is shown in Fig. 4(b); in contrast, a distinct peak in the signal of *m/z* = 97 is not shown in Fig. 4(a). Furthermore, the peaks of NH_3 and HBr observed as the fragments of NH_4Br are shown in Fig. 4(b); thus, it is reasonable to suppose that NH_4Br is contained in the deposition layer.

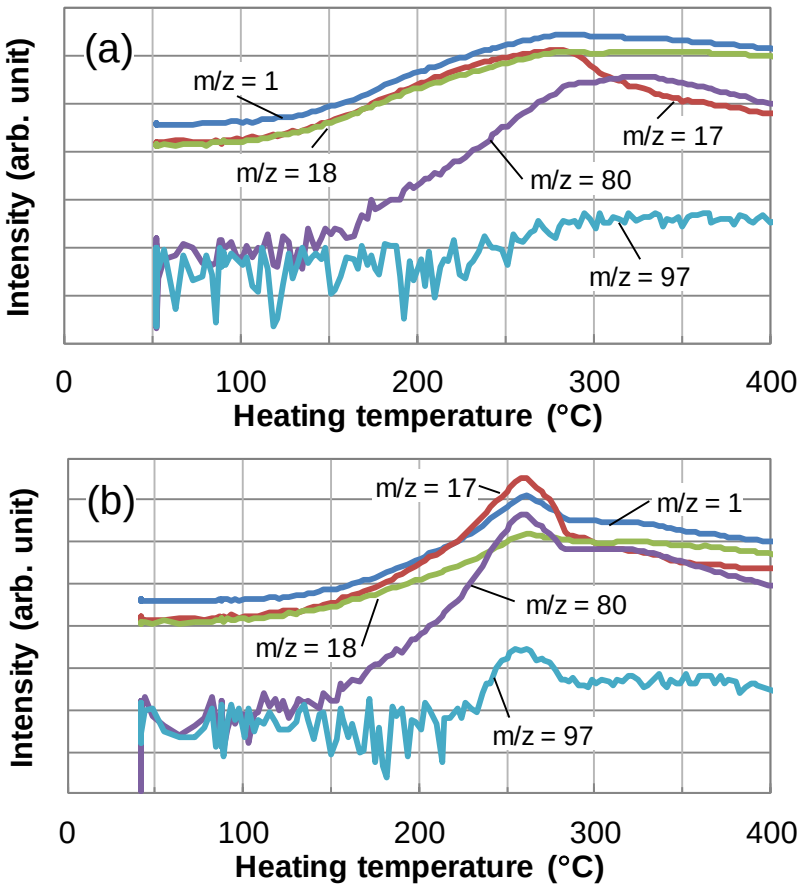

Fig. 4. TDS spectrum of deposition film on silicon surface. The deposition film was formed under HBr/N_2/fluorocarbon-based gas plasma with wafer temperatures of (a) 60°C and (b) 20°C.

Figure 5 shows the positive-ion laser-SNMS spectrum of the deposition film layer on a silicon surface. Deposition film layers were formed under HBr/N_2/fluorocarbon-based gas plasma at wafer temperatures of (a) 60 and (b) 20°C. To compare the wafer temperatures while plasma process, *m/z* = 18, 35, 107, 109, 115, and 117 were observed

in the deposition film of 20°C. The signals of *m/z* = 18 and 35 originated from NH_4^+ and $N_2H_7^+$, respectively, those of *m/z* = 107 and 109 from Si-Br^+, and those of *m/z* = 115 and 117 from $(NH_4)_2Br^+$. Therefore, it was clarified that ammonium bromide is present in the deposition film, and that its composition is $(NH_4)_2Br$. The positive ions NH_4^+ and $N_2H_7^+$ might be fragments of $(NH_4)_2Br$ considering the TDS results.

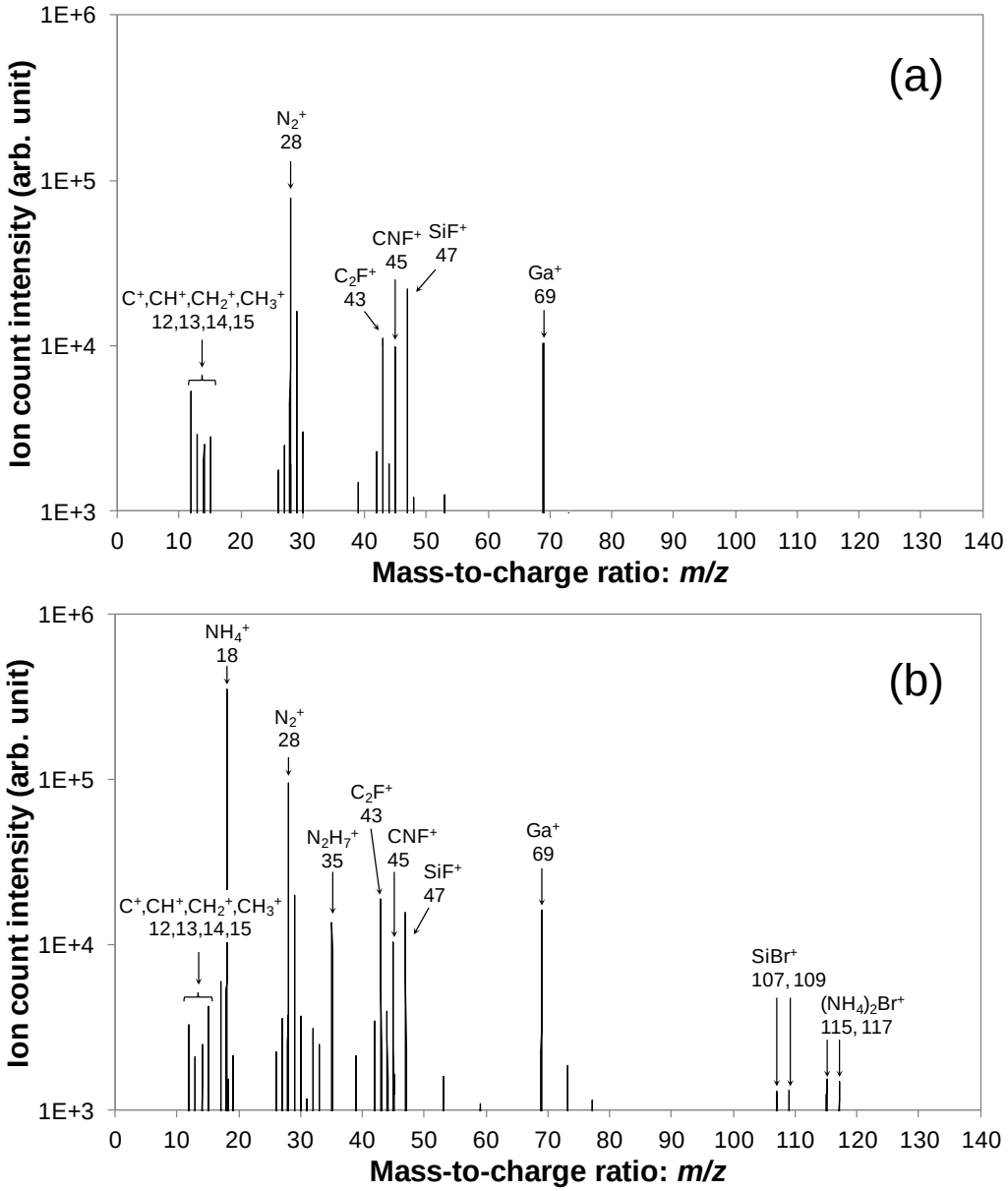

Fig. 5. Positive-ion laser-SNMS spectrum of deposition film on silicon surface. The deposition film was formed under HBr/N_2/fluorocarbon-based gas plasma with wafer temperatures of (a) 60 and (b) 20°C.

To investigate the deposition film composition in detail, the laser-SNMS two-dimensional (2D) images of the deposition film formed at 20°C on a silicon surface were analyzed. Figure 6 shows the laser-SNMS 2D images of *m/z* = 1 (H^-), 18 (NH_4^+), 19 (F^-), 26 (CN^-), 79 (Br^-), and 115 [$(NH_4)_2Br^+$]. A number of grains with diameter of 1-5 μm formed on the Si surface. The negative ions F^- and CN^- were distributed all over the surface except in the grains [Fig. 6(c) and 6(d)], where as the negative ions H^- and Br^- were distributed all over the surface at large numbers in the grains [Fig. 6(a) and 6(e)]. The positive ions NH_4^+ and $(NH_4)_2Br^+$ were distributed only in the grains [Fig. 6(b) and 6(f)]. It was confirmed by SEM observations that the grains increased in size as well as in number after being exposed to air. The grains should be condensed by atmospheric moisture because ammonium bromide has hygroscopic properties at room temperature. Thus, ammonium bromide does not form the condensed particles before air exposure. The results of the laser-SNMS 2D image analysis and SEM observation indicate that the deposition film consisted of a mixture of C, H, N, F, and Br, and $(NH_4)_2Br$ molecules.

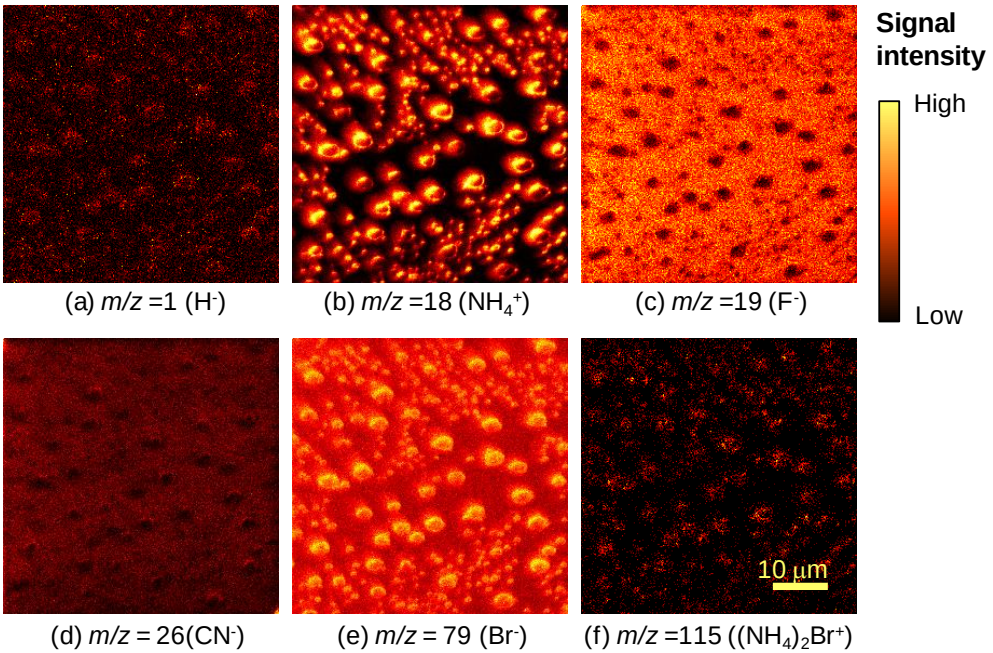

Fig. 6. Laser-SNMS images of deposition film on silicon surface. The deposition film was formed under HBr/N_2/fluorocarbon-based gas plasma with a wafer temperature of 20°C.

The presence of solid-phase ammonium bromide determined by chemical equilibrium simulation in our previous work corresponded to the result of the surface composition analysis in this study.[17] Figure 7 shows the schematic fluorocarbon polymer deposition films formed at wafer temperatures of (a) 60 and (b) 20°C. When the wafer temperature is 60°C, a carbon-based fluorocarbon polymer deposition film on the Si surface randomly contains H, N, and Br [Fig. 7(a)]. When the wafer temperature is 20°C, the deposition film consists of ammonium bromide $(NH_4)_2Br$ in addition to the carbon-based fluorocarbon polymer shown at 60°C [Fig. 7(b)]. Atoms and molecules in the etching reactor constantly repeat adsorption and desorption on a surface. N, H, and Br that adsorbed on the surface were possibly fixed in the deposition film by the formation of ammonium bromide before desorption from the surface. Therefore, increases in the atomic concentrations of N, H, and Br in the deposition film at 20°C were caused by ammonium bromide formation. If the atomic concentrations of N and H increase in the fluorocarbon polymer as a deposition film, the carbon amount on a surface would decrease when ions are irradiated by applying wafer bias because N and H react with carbon to volatilize as HCN.[31, 32] Br in the deposition film could possibly increase the poly-Si etching rate because Br and Si react to volatilize as $SiBr_x$. According to the above results, the presence of N, H, and Br on a surface caused by the formation of ammonium bromide is key to increasing the etching rate at low wafer temperatures under HBr/N_2/fluorocarbon-based gas plasma.

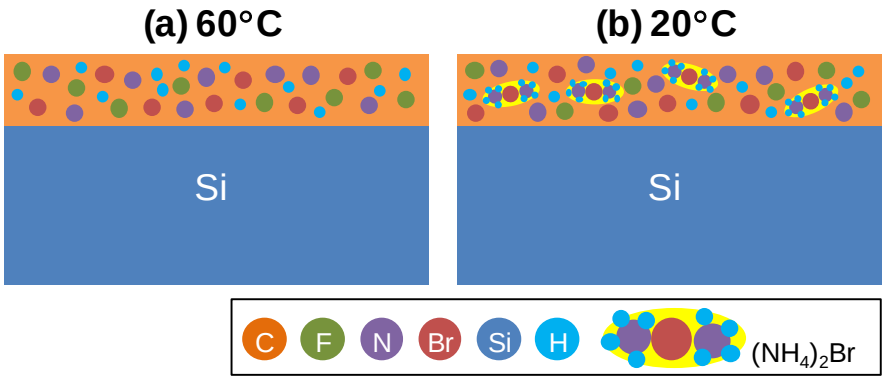

Fig. 7. Schematics of fluorocarbon polymer deposition films formed at wafer temperatures of (a) 60 and (b) 20°C without wafer bias.

3.4 Conclusion

The effects of wafer temperature on etching rate and surface composition were investigated to clarify the surface reaction mechanism under HBr/N_2/fluorocarbon-based gas plasma for developing a process for 3D NAND flash memory. Both the etching rates of poly-Si and SiO_2 using blanket wafers increased as temperatures decreased from 60 to 20°C. The gas chemistry effect on the etching rate was investigated by comparing process gas combinations such as fluorocarbon/N_2 and HBr/N_2 mixtures. One of the causes of temperature dependence is the sticking probability of fluorocarbon polymers because the SiO_2 etching rate increased as the temperature decreased under fluorocarbon/N_2 mixture gas plasma. However, the temperature dependence of poly-Si etching was omit different from that of SiO_2 etching. Under HBr/N_2/fluorocarbon-based gas plasma with a wafer temperature of 20°C, an ammonium bromide composition of $(NH_4)_2Br$ was observed in a deposition film that consisted of a C, H, N, F, and Br mixture by TDS and laser-SNMS analyses. N, H, and Br were fixed to the surface by the formation of ammonium bromide. Therefore, an increase in poly-Si etching rate at low temperatures was possibly caused by the volatilization of silicon and carbon with increased amounts of N, H, and Br. The proposed surface reaction mechanism based on the HBr/N_2/fluorocarbon-based gas plasma process will be a promising technology for fabricating next-generation 3D NAND flash memory devices.

References

[1] H. Tanaka, M. Kido, K. Yahashi, M. Oomura, R. Katsumata, M. Kito, Y. Fukuzumi, M. Sato, Y. Nagata, Y. Matsuoka, Y. Iwata, H. Aochi, and A. Nitayama, Symp. VLSI Technology Dig. Tech. Pap., 2007, p. 14.

[2] Y. Fukuzumi, R. Katsumata, M. Kito, M. Kido, M. Sato, H. Tanaka, Y. Nagata, Y. Matsuoka, Y. Iwata, H. Aochi, and A. Nitayama, IEDM Tech. Dig., 2007, p. 449.

[3] R. Katsumata, M. Kito, Y. Fukuzumi, M. Kido, H. Tanaka, Y. Komori, M. Ishiduki, J. Matsunami, T. Fujiwara, Y. Nagata, Z. Li, Y. Iwata, R. Kirisawa, H. Aochi, and A. Nitayama, Symp. VLSI Technology Dig. Tech. Pap., 2009, p. 136.

[4] W. Kim, S. Choi, J. Sung, T. Lee, C. Park, H. Ko, J. Jung, I. Yoo, and Y. Park, Symp. VLSI Technology Dig. Tech. Pap., 2009, p. 188.

[5] H.-T. Lue, T.-H. Hsu, Y.-H. Hsiao, S. P. Hong, M. T. Wu, F. H. Hsu, N. Z. Lien, S.-Y. Wang, J.-Y. Hsieh, L.-W. Yang, T. Yang, K.-C. Chen, K.-Y. Hsieh, and C.-Y. Lu, Symp. VLSI Technology Dig. Tech. Pap., 2010, p. 131.

[6] C-P. Chen, H-T. Lue, K-P. Chang, Y-H. Hsiao, C-C. Hsieh, S-H. Chen, Y-H. Shih, K-Y. Hsieh, T. Yang, K-C. Chen, and C-Y. Lu, Symp. VLSI Technology Dig. Tech. Pap., 2012, p. 91.

[7] S. Whang, K. Lee, D. Shin, B. Kim, M. Kim, J. Bin, J. Han, S. Kim, B. Lee, Y. Jung, S. Cho, C. Shin, H. Yoo, S. Choi, K. Hong, S. Aritome, S. Park, and S. Hong, IEDM Tech. Dig., 2010, p. 668.

[8] S. H. Chen, H. T. Lue, Y. H. Shih, C. F. Chen, T. H. Hsu, Y. R. Chen, Y. H. Hsiao, S. C. Huang, K. P. Chang, C. C. Hsieh, G. R. Lee, A. T. H. Chuang, C. W. Hu, C. J. Chiu, L. Y. Lin, H. J. Lee, F. N. Tsai, C. C. Yang, T. Yang, and C. Y. Lu, IEDM Tech. Dig., 2012, p. 21.

[9] A. Goda and K. Parat, IEDM Tech. Dig., 2012, p. 13.

[10] H. Lue, T. Hsu, C. Wu, W. Chen, T. Yeh, K. Chang, C. Hsieh, P. Du, Y. Hsiao, Y. Jiang, G. Lee, R. Lo, Y. Su, C. Huang, S. Lai, L. Liang, C. Chen, M. Hung, C. Hu, C. Chiu, and C. Lu, IEDM Tech. Dig., 2015, p. 44.

[11] K. Parat and C. Dennison, IEDM Tech. Dig., 2015, p. 48.

[12] M. A. Vyvoda, H. Lee, M. V. Malyshev, F. P. Klemens, M. Cerullo, V. M. Donnelly, D. B. Graves, A. Kornblit, and J. T. C. Lee, J. Vac. Sci. Technol. A **16**, 3247 (1998).

[13] N. R. Rueger, J. J. Beulens, M. Schaepkens, M. F. Doemling, J. M. Mirza, T. E. F. M. Standaert, and G. S. Oehrlein, J. Vac. Sci. Technol. A **15**, 1881 (1997).

[14] D. R. Sparks, J. Electrochem. Soc. **139**, 1736 (1992).

[15] Z. Yang, F.-H. Hsu, L. Y. Lin, H.-J. Lee, N.-T. Lian, T. Yang, K.-C. Chen, and C.-Y. Lu, Advanced Semiconductor Manufacturing Conf. (ASMC), 2013, p. 24.

[16] T. Iwase, M. Matsui, K. Yokogawa, T. Arase, and M. Mori, *Proc.* Int. Symp. Dry Process, 2015, p. 47.

[17] T. Iwase, M. Matsui, K. Yokogawa, T. Arase, and M. Mori, Jpn. J. Appl. Phys. **55**, 06HB02

(2016).
[18] J. K. Jung and W. J. Lee, Jpn. J. Appl. Phys. **40**, 1408 (2001).
[19] L. Vallier, J. Foucher, X. Detter, E. Pargon, O. Joubert, G. Cunge, and T. Lill, J. Vac. Sci. Technol. B **21**, 904 (2003).
[20] M. Kim, N. K. Min, S. J. Yun, H. W. Lee, A. M. Efremov, and K. H. Kwon, ETRI J. **30**, 383 (2008).
[21] Y. H. Ham, A. Efremov, H. W. Lee, S. J. Yun, N. K. Min, K. Kim, and K. H. Kwon, Jpn. J. Appl. Phys. **49**, 08JB03 (2010)
[22] C. W. Garland and C. F. Yarnell, J. Chem. Phys. **44**, 1112 (1966).
[23] C. G. de Kruif, J. Chem. Phys. **77**, 6247 (1982).
[24] D. Tomida, K. Suzuki, and C. Yokoyama, J. Chem. Eng. Data **55**, 341 (2010).
[25] K. Yokogawa, K. Maeda, H. Kobayashi, T. Kanekiyo, and M. Izawa, Proc. 7th Int. Conf. Microelectronics and Interfaces, 2006, 0940-10.
[26] K. Yokogawa, K. Maeda, and M. Izawa, Jpn. J. Appl. Phys. **47**, 6854 (2008).
[27] A. Schnieders, R. Möllers, M. Terhorst, H. ‐ G. Cramer, E. Niehuis and A. Benninghoven, J. Vac. Sci. Technol. B **14**, 2712 (1996).
[28] T. Ishikawa, T. Kashiwagi, T Sakamoto, K. Misawa, M. Fujii, M. Hachiya, H. Noda, and K. Endo, J. Surf. Sci. Jpn. **35**, 383 (2014) [in Japanese].
[29] C. Chu, T. Ahn, J. Kim, S. Jeong, and J. Moon, J. Vac. Sci. Technol. B **18**, 2763 (2000).
[30] S. A. Vitale, H. Chae, and H. H. Sawin, J. Vac. Sci. Technol. A **19**, 2197 (2001).
[31] H. Nagai, S. Takashima, M. Hiramatsu, M. Hori, and T. Goto, J. Appl. Phys. **91**, 2615 (2002).
[32] M. Ooka and S. Yokoyama, Jpn. J. Appl. Phys. **44**, 6476 (2005).

4. Eliminating Dependence of Hole Depth on Aspect Ratio by Forming Ammonium Bromide in HBr/CH_3F-based Gas Plasmas

4.1 Introduction

To overcome scaling limitations, the structure of NAND flash memories has evolved from planar to three-dimensional (3D). As for the architecture of 3D NAND flash, memory cells are stacked perpendicularly in an integrated device. 3D NAND devices such as bit-cost scalable (BiCS)[1-3], vertical-gate NAND (VG-NAND)[4-6], and terabit-cell-array transistor (TCAT)[7] technologies can reduce production costs per memory bit by using a single deep-etching process. These stacked devices are typically composed of alternating layers of SiN (or polycrystalline-Si) and SiO_2.[8-12] It is therefore essential to develop deep, high-aspect-ratio (HAR) etching technology for fabricating multilayer stacks of SiN/SiO_2 and poly-Si/SiO_2. Generally, different materials are etched by using different etching technologies. For example, poly-Si and SiO_2 are etched by using halogen and fluorocarbon-based gases, respectively, in a specific etching reactor. Therefore, hardware and processes for etching different materials simultaneously should be developed.[13]

In our previous works, one-step deep etching with HBr/N_2/fluorocarbon-based gas plasma was performed to fabricate poly-Si/SiO_2 stacks.[14-17] The HBr and fluorocarbon-based gases were mixed to achieve uniform etching rates for both poly-Si and SiO_2 and thus obtain smooth side walls in the etched holes.[18-22] Furthermore, nitrogen gas was added to the etching gas, and the substrate temperature was adjusted to obtain a vertical hole profile. A film consisting of a fluorocarbon polymer was deposited on the substrate when the substrate was not bombarded with ions from the plasma, and a mixing layer (2−3 nm thick) containing carbon, fluorine, nitrogen, bromine, and substrate material formed when the substrate was bombarded with ions. By TDS and time-of-flight secondary ion mass spectrometry (TOF-SIMS), it was confirmed that ammonium bromide (NH_4Br) is present in the deposition film at a substrate temperature of 20 °C. The increase in poly-Si etching rate at a lower temperature was possibly caused by increased amounts of nitrogen, hydrogen, and bromine attached to the substrate surface with the formation of NH_4Br.

To obtain a higher bit density in 3D NAND, the aspect ratio defined as the ratio of hole diameter to depth is continuously increased, and deep holes with aspect ratios of 100

or higher will be required in the future. However, etching rate decreases as aspect ratio increases, and in extreme cases, etching stops. It is therefore critical to investigate the etching mechanism in deep holes to overcome the limit on etching depth. One approach to investigating this mechanism is to evaluate changes in the composition of the etched surfaces of the holes. Conventionally, the surface composition is analyzed by using a blanket wafer or micro/macro-cavity method to simulate a reaction inside a real structure.[23, 24] However, the compositional change in high-aspect-ratio hole patterns has hardly been directly observed.

In this study, the surface composition inside deep holes etched in SiN/SiO_2 stacks and silicon layers formed under HBr/N_2/fluorocarbon-based gas plasma was focused. First, the relationship between the etching rate and the gas composition during the fabrication of vertical holes in SiN/SiO_2 stacks was evaluated. Then, the temperature dependence of the cross-sectional profile of the holes was evaluated. Simultaneously, the surface composition inside the deep holes was observed directly by TOF-SIMS with high spatial resolution and sensitivity. Finally, the etching mechanism was investigated by analyzing the cross-sectional profile and surface composition of the SiN/SiO_2 stacks.

4.2 Experimental procedure

Stacked films were fabricated with a hole pattern, and their profile was evaluated. A schematic image of a sample fabricated film is shown in Fig. 1. Eight pairs of 50-nm-thick SiN and SiO_2 layers were alternately deposited on a silicon substrate. A carbon layer was deposited as an etching mask on the SiN/SiO_2 stacks, and a SiON layer was deposited as an anti-reflective layer. Holes with diameters of 50 to 100 nm were patterned in a resist film coated on the SiON layer by electron beam lithography. The SiON and carbon layers were etched as a hard mask for etching the SiN/SiO_2 stacks, which were etched using the plasma generated by HBr/N_2/fluorocarbon-based gas in a parallel-plate plasma reactor (shown schematically in Fig. 2). 20-mm-square coupons of stacked film samples were pasted on photoresist-coated 300 mm wafers.

In the reactor used to etch the sample stacked films, plasma was generated by a 200 MHz power source, and a RF bias was applied to the lower electrode by a 4 MHz power source. The plasma distribution was controlled by a magnetic field generated by the coils

around the reactor.[25, 26] The samples were etched on the blanket silicon wafer in the reactor at a pressure of 6.0 Pa under HBr/N_2/fluorocarbon-based gas plasma generated with a source power of 1000 W. The energy of the ions incident onto the sample was controlled by applying a RF bias power of 1200 W. The temperature of the sample (set on an electrostatic chuck stage) was maintained between 20 and 80 °C by using a circulator system.

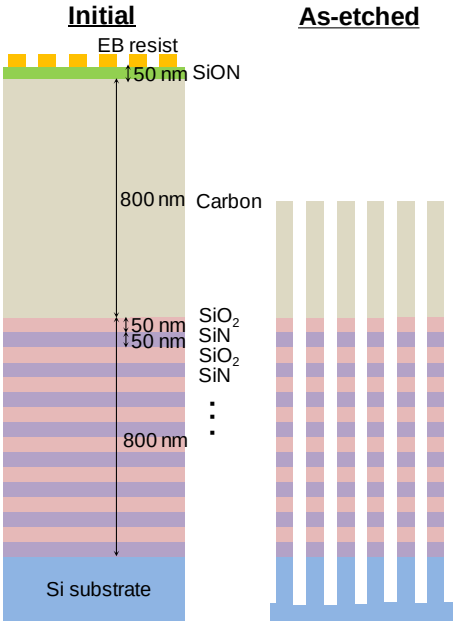

Fig. 1. Schematic images of initial sample and sample as etched for evaluating surface composition.

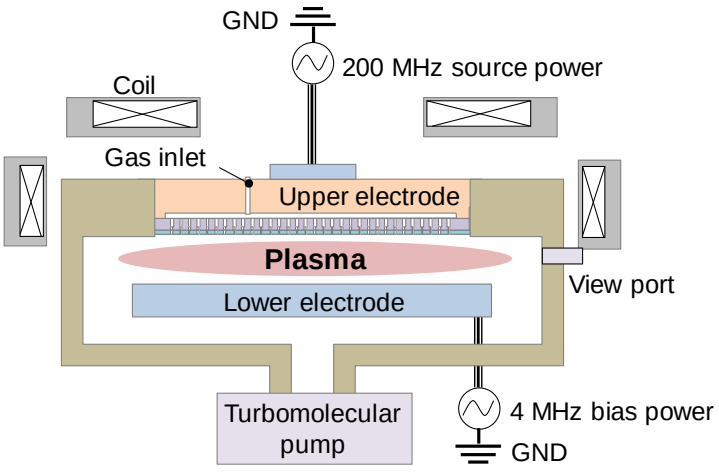

Fig. 2. Schematic of parallel-plate etching reactor. The reactor has a 200 MHz VHF plasma source and a 4 MHz wafer bias generator. The gas inlet in the upper electrode is made of dielectric material that withstands corrosive gas.

Etching rate was calculated on the basis of film thickness obtained before and after plasma processing. Film thickness was measured by using an optical film-thickness meter. The samples, which had hole patterns after etching, were cleaved so that the inner walls of the holes could be analyzed. A cross-sectional profile was observed by field-emission scanning electron microscopy. The surface composition was analyzed at a high spatial resolution by TOF-SIMS (Toyama, FILMER).[27, 28] Positive gallium ions (Ga^+) were used as the primary ions at a dose of 1×10^{12} ions/cm^2. The mass of secondary ions sputtered from inside the walls of the holes was detected and mapped in two dimensions.

4.3 Results and discussion

4.3.1 Temperature dependence of etching rate

To etch the SiN and SiO_2 films simultaneously at a uniform etching rate, the etching selectivity of each material was investigated. It was previously shown that the etching selectivity of poly-Si and SiO_2 can be controlled by adjusting the mixture ratio of HBr and fluorocarbon gas.[15] That selectivity control is possible because the reactivities of poly-Si and SiO_2 differ under HBr and fluorocarbon gas plasma, respectively. Since SiN and SiO_2 have different bond energies and volatilities of by-products, it is assumed that their etching selectivity changes similarly to that of poly-Si/SiO_2 at a certain mixture ratio of HBr and fluorocarbon gas. The dependence of the etching rates of various materials on the HBr/fluorocarbon gas mixture ratio is plotted in Fig. 3. According to this plot, as the HBr ratio decreases, the etching rate of SiN changes slightly, but that of SiO_2 increases significantly. Moreover, the etching selectivity is closest to 1 when HBr/(HBr + fluorocarbon) equals 0.4.

The temperature dependence of etching rate was investigated as follows. It was previously shown that NH_4Br tends to be formed when the substrate temperature is lower than 20°C.[15] When NH_4Br is present on the substrate, as shown in the following reaction formulas, it acts as an etchant for Si, SiO_2, and SiN.

$$NH_4Br(s) + Si(s) \rightarrow SiBr_4(g)\uparrow + NH_3(g)\uparrow \quad (1)$$

$$NH_4Br(s) + SiO_2(s) \rightarrow SiBr_4(g)\uparrow + H_2O(g)\uparrow + N_2(g)\uparrow \quad (2)$$

$$NH_4Br(s) + Si_3N_4(s) \rightarrow SiBr_4(g)\uparrow + NH_3(g)\uparrow + N_2(g)\uparrow \quad (3)$$

The dependence of etching rate on substrate temperature is plotted in Fig. 4 when gas flow was set to HBr/N_2/fluorocarbon = 32/25/43. The plot shows that etching rate increases with decreasing temperature in the temperature range of 20 to 60 °C for all four materials. The temperature dependence of etching rate under HBr/fluorocarbon-based gas plasma excluding N_2 obtained in the previous study is different from the result in Fig. 4.[17] The increase in SiO_2 etching rate under HBr/fluorocarbon-based gas plasma at low temperatures is linear and smaller than that in Fig. 4. It is assumed that etching rate increases at low temperatures because the deposition rate of the CH_xF_y polymer as an etchant increases and/or the formation rate of NH_4Br as an etchant increases.

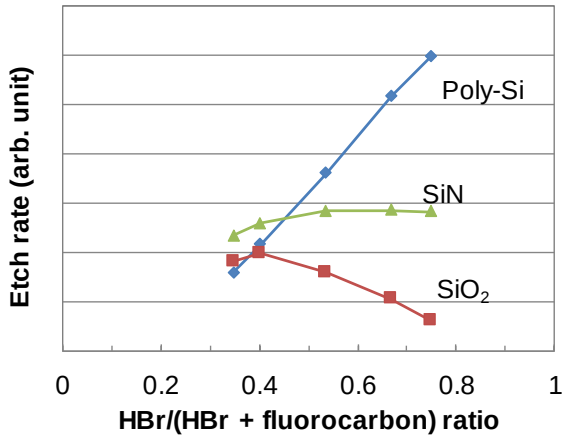

Fig. 3. Dependence of HBr/fluorocarbon gas mixing ratio on etching rates of poly-Si, SiN, and SiO_2 films. Etching rates were evaluated by using blanket wafers.

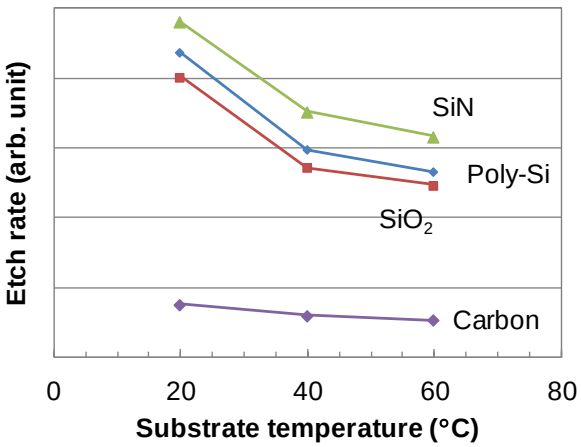

Fig. 4. Dependence of substrate temperature on etching rate of poly-Si, SiN, SiO_2, and carbon film. Etching rates were evaluated by using blanket wafers.

4.3.2 Temperature dependence of etched-hole profile

Films composed of alternating stacks of SiN and SiO_2 were etched to form HAR holes under uniform etching selectivity. Scanning electron microscope (SEM) images of the cross-sectional shapes of the stacked films in the case of four substrate temperatures but constant processing time are shown in Fig. 5. Holes that penetrate the SiN/SiO_2 stacked films and reach the silicon substrate are formed at substrate temperatures lower than 60 °C. It is clear that the depth of the holes increases with decreasing substrate temperature, and that this result agrees with the temperature dependence of the etching rate. To understand the temperature dependence of the cross-sectional shape more clearly, a sample stacked film was prepared with a uniform hole depth by adjusting the etching time.

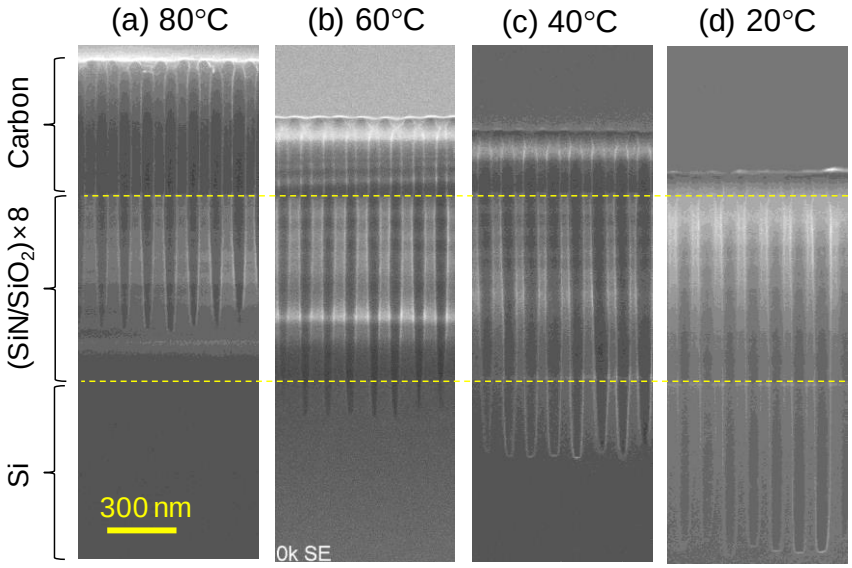

Fig. 5. Cross-sectional SEM images of 50-nm-diameter holes in a SiN/SiO_2 stacked layer. Substrate temperatures during etching were (a) 20, (b) 40, (c) 60, and (d) 80 °C. Etching time fixed on all samples.

SEM images of the cross sections of holes fabricated at substrate temperatures of 60 and 20 °C are shown in Fig. 6. At low temperatures, the etching selectivity of the SiN/SiO_2 stacked films in relation to the carbon mask improved because the amount of remaining mask increased. That is, the effect of increasing etching rate with decreasing temperature is larger in the cases of the SiN and SiO_2 films than in the case of the carbon film. Comparing the bottom shapes of the holes, namely, the etch front, reveals that, in the 60 °C case, the holes have a tapered bottom, whereas in the 20 °C case, they have a

rectangular, flat surface bottom. The result indicating that the bottom shape changes only with the substrate temperature can be considered to be due to fact that the etching of the bottom is controlled by the supply of radicals rather than of ions. Therefore, this result suggests that the lower the substrate temperature, the more radicals as an etchant are transported to the bottom of the holes.

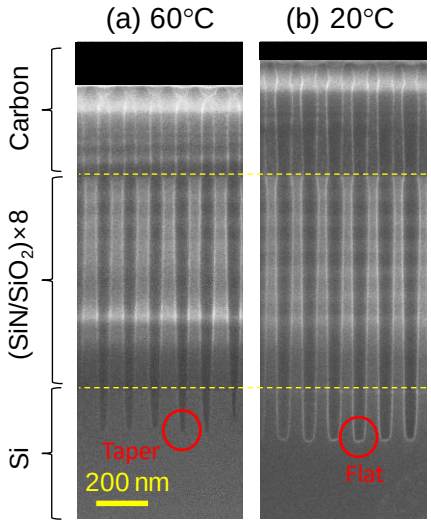

Fig. 6. Cross-sectional SEM images of 50-nm-diameter holes in a SiN/SiO_2 stacked layer. Substrate temperatures were (a) 60 and (b) 20 °C. Etch time was adjusted to obtain uniform hole depth.

4.3.3 Temperature dependence of surface composition inside holes

To investigate whether the composition of the inner wall of the holes changed with substrate temperature in a similar manner as the evaluation using a flat film, cross sections of the holes in SiN/SiO_2 stacked films were observed by TOF-SIMS. Two-dimensional TOF-SIMS images were obtained by plotting the intensity of the detected secondary ions at each mass-to-charge ratio (*m/z*). Cross-sectional SEM images of the holes in SiN/SiO_2 stacked films and the corresponding TOF-SIMS images are shown in Fig. 7. The TOF-SIMS images illustrate negative oxygen ions (O^-) for $m/z = 16$, negative fluorine ions (F^-) for $m/z = 19$, and negative bromine ions (Br^-) for $m/z = 81$. Large numbers of O^- corresponding to the position of the SiN/SiO_2 stacked film were detected, and the dependence of O^- intensity on substrate temperature during etching is not shown. Large numbers of F^- were detected on the silicon substrate because the amount of CH_xF_y

polymer deposited on silicon is larger than those on SiN and SiO_2. Additionally, F^- intensity has almost no dependence on substrate temperature. It is clear that the amount of CH_xF_y polymer deposited does not significantly differ with temperature. On the other hand, Br^- intensity varies greatly with substrate temperature, and higher intensity was detected in whole part of etched holes at 20 °C.

The substrate temperature dependence of Br^- intensity in the hole portion is shown in Fig. 8. Br^- intensity is indicated by the relative value of O^- intensity and is normalized by the cross-sectional area of the hole portion. It is clear that Br^- intensity at 20 °C is one order of magnitude higher than that at 60 °C.

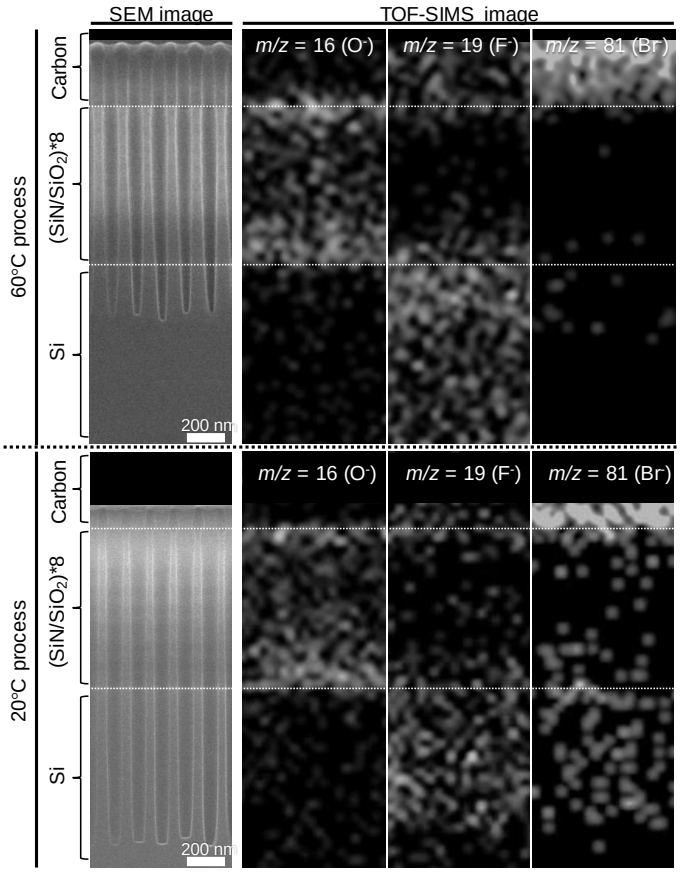

Fig. 7. SEM and TOF-SIMS images of cross-sectional holes etched by HBr/N_2/fluorocarbon plasma at substrate temperatures of 60 and 20 °C. TOF-SIMS images indicate a negative secondary ion (m/z = 16, 19, 81) intensity.

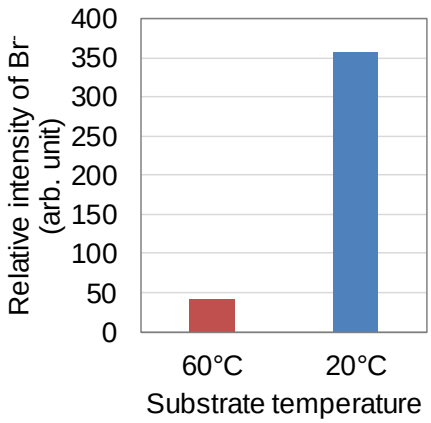

Fig. 8. Relative intensities of Br^- with O^-, which are detected on cross section of etched holes in SiN/SiO_2 stacks at substrate temperatures of 60 and 20 °C. The intensities were normalized by the hole cross-sectional area.

From the results concerning the above-described cross-sectional profiles of the etched holes and the temperature dependence of the surface composition inside the holes, it can be considered that deep holes progress owing to the increased amount of bromine adsorbed as substrate temperature decreases. A previous report investigated the relationship between substrate temperature and silicon trench depth in the case of a simple gas chemistry such as HBr/O_2, and the obtained results revealed that trench depth hardly changed with temperature.[29] Therefore, it is assumed that, in the temperature range of 20 to 60 °C, the dependence of trench depth is not affected by the increase in the sticking coefficient of bromine caused by the decrease in substrate temperature. The results of a previously reported simulation of equilibrium composition revealed that the generation rate of NH_4Br in that temperature range increases with decreasing temperature.[15] It is reasonable to suppose that the increase in the number of Br ions at low temperatures is derived from NH_4Br because the temperature dependence of Br^- intensity in the etched holes determined by cross-sectional analysis agrees with that of the NH_4Br intensity of the deposited film determined by blanket wafer analysis.

4.3.4 Formation process of ammonium bromide

The formation process of ammonium bromide on the surface is considered as follows. It is assumed that nitrogen (N), hydrogen (H), and bromine (Br) are chemisorbed on the

substrate surface and then synthesized into NH_4Br at a constant reaction rate. For example, the following reaction path can be considered:

$$N(g) \rightarrow N(\text{adsorption}), \quad (4)$$

$$N(\text{adsorption}) + H(g) \rightarrow NH(\text{adsorption}), \quad (5)$$

$$NH(\text{adsorption}) + H(g) \rightarrow NH_2(\text{adsorption}), \quad (6)$$

$$NH_2(\text{adsorption}) + H(g) \rightarrow NH_3(\text{adsorption}), \quad (7)$$

$$NH_3(\text{adsorption}) + H(g) \rightarrow NH_4(\text{adsorption}), \quad (8)$$

$$NH_4(\text{adsorption}) + Br(g) \rightarrow NH_4Br(\text{adsorption}). \quad (9)$$

It is thought that either of these reactions limits the rate, and the ease of formation of NH_4Br depends on substrate temperature. When substrate temperature is high, N, H, and Br adsorb only until the adsorption site disappears, whereas when substrate temperature is sufficiently low, NH_4Br is synthesized and more NH_4Br is formed by the newly adsorbed N, H, and Br. Therefore, the amount of NH_4Br formed seems to depend on the amounts of absorbed N, H, and Br. Under the assumption that the amounts of N, H, and Br supplied to the holes are sufficient and the entire surface is covered, the dependence of the amounts of adsorption on the aspect ratio should be very small. Accordingly, the amount of NH_4Br formed is also considered to have a small aspect ratio dependence.

4.3.5 Aspect-ratio-dependent etching

Since NH_4Br is considered to act as an etchant for SiN, SiO_2, and silicon, the dependence of the amount of NH_4Br on aspect ratio might be verified by investigating the dependence of the depth of etched holes on aspect ratio. A cross-sectional SEM image of a sample processed at a substrate temperature of 60 or 20 °C, with a hole diameter of 50 to 90 nm, is shown in Fig. 9. Although all the holes reach the silicon substrate, it is clear that the relationship between hole diameter and depth differs. The relationship between aspect ratio (defined as the ratio of hole diameter to depth) and hole depth is shown in Fig. 10. Clearly, hole depth decreases with increasing aspect ratio at higher substrate temperatures, and the slope of the aspect ratio dependence of hole depth at the substrate temperature of 20 °C is significantly small.

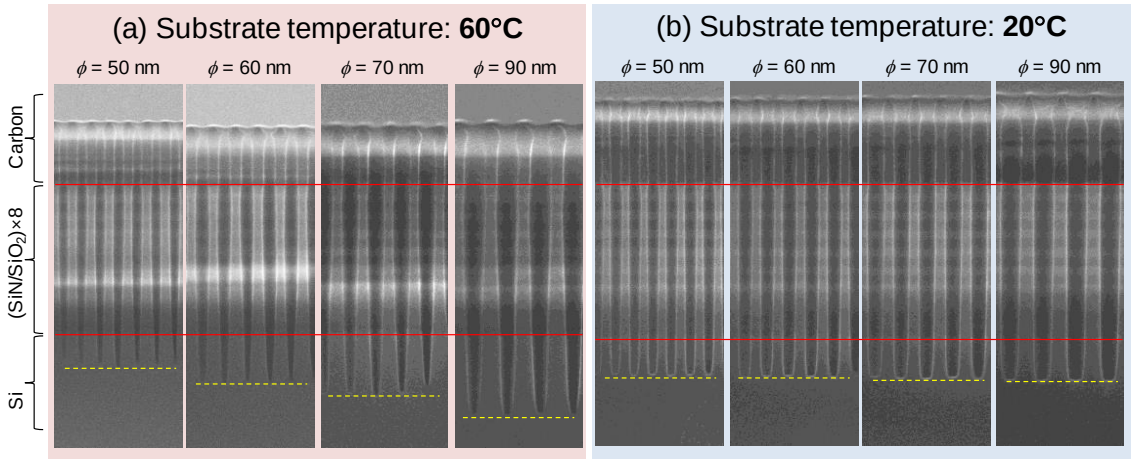

Fig. 9. Cross-sectional SEM images of 50-to-90-nm-diameter holes in a SiN/SiO_2 stacked layer. Substrate temperatures were (a) 60 and (b) 20 °C.

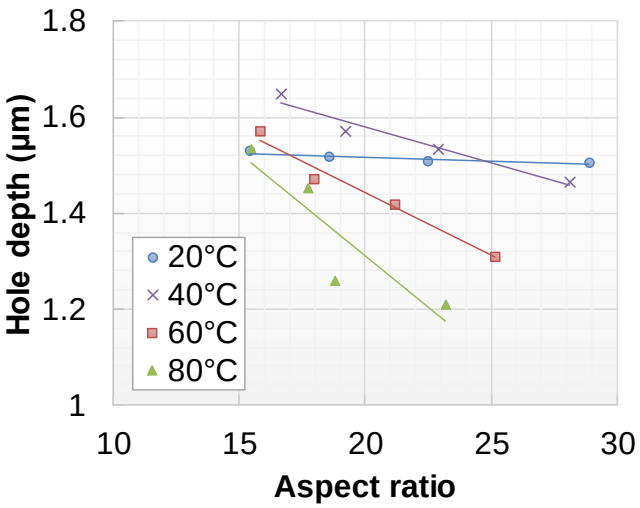

Fig. 10. Dependence of hole depth, defined as (etch depth + mask height), on aspect ratio. The substrate temperature during etching was either 20 or 80 °C.

The etching mechanism in the holes of SiN/SiO_2 stacked samples under the HBr/N_2/fluorocarbon-based plasma used in this study is discussed in the following. Etching reactions on SiN and SiO_2 are promoted by adsorbed radicals of mainly CF_x, CH_xF_y, N, H, Br, and F when ions were irradiated from plasma. CF_x and CH_xF_y radicals accumulate in multiple layers owing to many unpaired electrons. For example, when SiO_2 is etched to fabricate HAR holes by using CF_x/O_2 plasma, etching rate decreases with increasing aspect ratio.[30] The decrease in ion flux to promote etching and the insufficient

supply of radicals as an etchant can be cited as factors governing the decrease in etching rate. For example, the sticking probability of CF_x increases when substrate temperature is low. CF_x as the main etchant adsorbs to the top of the holes because the sticking probability is higher there, making it difficult for CF_x to reach the bottom. Conversely, N, H, Br, and F radicals are generally adsorbed at the monolayer level.[31-35] Under the assumption that the radical flux is sufficiently large and the surface is completely covered with N, H, Br, and F radicals, it is considered that the amount of radical at the bottom of the holes does not depend on substrate temperature. That is, when substrate temperature is sufficiently low, as for the gas chemistry focused on in this study, it is considered that N, H, and Br supplied to the bottom of the holes are converted to NH_4Br. Since the NH_4Br of an ion-binding molecule allows the multilayer adsorption of the own, the absolute amounts and composition ratios of N, H, and Br on the surface increase with the amount of NH_4Br formed. When the formation rate of NH_4Br is increased at low temperatures, etching rate increases because N, H, and Br promote the etching of SiN/SiO_2. The reaction mechanism for the reduction in the aspect ratio dependence of etching rate at low temperatures differs from that in the case of conventional HAR etching, and it can be considered that the formation of compounds such as ammonium bromide is the key technology for one-step etching for fabricating holes in SiN/SiO_2 stacked films.

4.4 Conclusion

A one-step etching technique for fabricating holes in SiN/SiO_2 stacked films, which is a promising technology for fabricating 3D NAND flash memories by using a HBr/N_2/fluorocarbon-based gas system, was developed, and its surface reaction mechanism was analyzed. To unify the etching selectivities of the SiN and SiO_2 films, the mixing ratio of HBr and fluorocarbon gas was set to HBr/(HBr + fluorocarbon) = 0.4; consequently, an etching selectivity close to one was obtained. It was experimentally found that the etching rates of both the SiN and SiO_2 films increase with decreasing temperature in the range of 20 to 60 °C. Even in the case of the hole etching of the SiN/SiO_2 stacked film, hole depth increased with decreasing substrate temperature, and the bottom of the holes (as the etch front) became flat. The observation of the cross section of the holes in the SiN/SiO_2 stacked film etched at 20 °C by TOF-SIMS indicated that

bromine ion intensity, which is considered to be derived from NH_4Br, is one order of magnitude higher than that at 60 °C. It was also found that the dependence of hole depth on aspect ratio decreases as temperature decreases; in particular, it decreases markedly at the substrate temperature of 20 °C. Since NH_4Br is assumed to be synthesized from chemisorbed nitrogen, hydrogen, and bromine, the amount of NH_4Br formed does not depend on the aspect ratio of the holes; that is, NH_4Br might be transported to the bottom of the holes as an etchant for SiN and SiO_2.

References

[1] H. Tanaka, M. Kido, K. Yahashi, M. Oomura, R. Katsumata, M. Kito, Y. Fukuzumi, M. Sato, Y. Nagata, Y. Matsuoka, Y. Iwata, H. Aochi, and A. Nitayama, Symp. VLSI Technol. Dig. Tech. Pap., 2007, p. 14.

[2] Y. Fukuzumi, R. Katsumata, M. Kito, M. Kido, M. Sato, H. Tanaka, Y. Nagata, Y. Matsuoka, Y. Iwata, H. Aochi, and A. Nitayama, IEDM Tech. Dig., 2007, p. 449.

[3] R. Katsumata, M. Kito, Y. Fukuzumi, M. Kido, H. Tanaka, Y. Komori, M. Ishiduki, J. Matsunami, T. Fujiwara, Y. Nagata, Z. Li, Y. Iwata, R. Kirisawa, H. Aochi, and A. Nitayama, Symp. VLSI Technol. Dig. Tech. Pap., 2009, p. 136.

[4] W. Kim, S. Choi, J. Sung, T. Lee, C. Park, H. Ko, J. Jung, I. Yoo, and Y. Park, Symp. VLSI Technol. Dig. Tech. Pap., 2009, p. 188.

[5] H.-T. Lue, T.-H. Hsu, Y.-H. Hsiao, S. P. Hong, M. T. Wu, F. H. Hsu, N. Z. Lien, S.-Y. Wang, J.-Y. Hsieh, L.-W. Yang, T. Yang, K.-C. Chen, K.-Y. Hsieh, and C.-Y. Lu, Symp. VLSI Technol. Dig. Tech. Pap., 2010, p. 131.

[6] C.-P. Chen, H.-T. Lue, K.-P. Chang, Y.-H. Hsiao, C.-C. Hsieh, S.-H. Chen, Y.-H. Shih, K.-Y. Hsieh, T. Yang, K.-C. Chen, and C.-Y. Lu, Symp. VLSI Technol. Dig. Tech. Pap., 2012, p. 91.

[7] J. Jang, H. Kim, W. Cho, H. Cho, J. Kim, S. I. Shim, Y. Jang, J. Jeong, B. Son, D. W. Kim, K. Kim, J. Shim, J. S. Lim, K. Kim, S. Y. Yi, J. Lim, D. Chung, H. Moon, S. Hwang, J. Lee, Y. Son, U. Chung, and W. Lee, Symp. on VLSI Technol. Tech. Dig., pp. 192-193 (2009).

[8] S. Whang, K. Lee, D. Shin, B. Kim, M. Kim, J. Bin, J. Han, S. Kim, B. Lee, Y. Jung, S. Cho, C. Shin, H. Yoo, S. Choi, K. Hong, S. Aritome, S. Park, and S. Hong, IEDM Tech. Dig., 2010, p. 668.

[9] S. H. Chen, H. T. Lue, Y. H. Shih, C. F. Chen, T. H. Hsu, Y. R. Chen, Y. H. Hsiao, S. C. Huang, K. P. Chang, C. C. Hsieh, G. R. Lee, A. T. H. Chuang, C. W. Hu, C. J. Chiu, L. Y. Lin, H. J. Lee, F. N. Tsai, C. C. Yang, T. Yang, and C. Y. Lu, IEDM Tech. Dig., 2012, p. 21.

[10] A. Goda and K. Parat, IEDM Tech. Dig., 2012, p. 13.

[11] H. Lue, T. Hsu, C. Wu, W. Chen, T. Yeh, K. Chang, C. Hsieh, P. Du, Y. Hsiao, Y. Jiang, G. Lee, R. Lo, Y. Su, C. Huang, S. Lai, L. Liang, C. Chen, M. Hung, C. Hu, C. Chiu, and C. Lu, IEDM Tech. Dig., 2015, p. 44.

[12] K. Parat and C. Dennison, IEDM Tech. Dig., 2015, p. 48.

[13] T. Ichikawa, D. Ichinose, K. Kawabata, and N. Tamaoki, SISPAD proc., 2010, p. 45.

[14] T. Iwase, M. Matsui, K. Yokogawa, T. Arase, and M. Mori., Proc. Int. Symp. Dry Process, 2015, p. 47.

[15] T. Iwase, M. Matsui, K. Yokogawa, T. Arase, and M. Mori, Jpn. J. Appl. Phys. **55**, 06HB02 (2016).

[16] T. Iwase, K. Yokogawa, and M. Mori., Proc. Int. Symp. Dry Process, 2016, p. 197.

[17] T. Iwase, K. Yokogawa, and M. Mori., Jpn. J. Appl. Phys. **56**, 06HB04 (2017).

[18] D. R. Sparks, J. Electrochem. Soc. **139**, 1736 (1992).

[19] J. K. Jung and W. J. Lee, Jpn. J. Appl. Phys. **40**, 1408 (2001).

[20] L. Vallier, J. Foucher, X. Detter, E. Pargon, O. Joubert, G. Cunge, and T. Lill, J. Vac. Sci. Technol. B **21**, 904 (2003).

[21] M. Kim, N. K. Min, S. J. Yun, H. W. Lee, A. M. Efremov, and K. H. Kwon, ETRI J. **30** [3] 383 (2008).

[22] Y. H. Ham, A. Efremov, H. W. Lee, S. J. Yun, N. K. Min, K. Kim, and K. H. Kwon, Jpn. J. Appl. Phys. **49**, 08JB03 (2010).

[23] K. Watanabe and H. Komiyama, J. Electrochem. Soc. **137**, 1222 (1990).

[24] T. Sorita, S. Shiga, K. Ikuta, Y. Egashira, and H. Komiyama, J. Electrochem. Soc. **140**, 2952 (1993).

[25] K. Yokogawa, K. Maeda, H. Kobayashi, T. Kanekiyo, and M. Izawa, Proc. 7th Int. Conf. Microelectronics and Interfaces, 2006, 0940-10.

[26] K. Yokogawa, K. Maeda, and M. Izawa, Jpn. J. Appl. Phys. **47**, 6854 (2008).

[27] A. Schnieders, R. Möllers, M. Terhorst, H.-G. Cramer, E. Niehuis, and A. Benninghoven, J. Vac. Sci. Technol. B **14**, 2712 (1996).

[28] T. Ishikawa, T. Kashiwagi, T Sakamoto, K. Misawa, M. Fujii, M. Hachiya, H. Noda, and K. Endo, Hyomen Kagaku **35**, 383 (2014) [in Japanese].

[29] W. Park, W. Lee, W. Kim, H. Kim, and K. Whang, J. Appl. Phys. **53**, 036502 (2014).

[30] O. Joubert, G. S. Oehrlein, and Y. Zhang., J. Vac. Sci. Technol. A **12**, p. 658 (1994).

[31] T. D. Bestwick and G. S. Oehrlein, J. Vac. Sci. Technol. A **8**, p.1696 (1990).

[32] C. D. Stinespring and A. Freedman, Appl. Phys. Lett. **48**, p.718, (1986).

[33] G. Pennington and C. R. Ashman, Appl. Phys. Lett. **91**, 072106 (2007).

[34] K.-C. Chang, Y. Cao, L. M. Porter, J. Bentley, S. Dhar, L. C. Feldman, and J. R. Williams, J. Appl. Phys. **97**, 104920 (2005).

[35] Y.J. Chabal and K. Raghavachari, Phys. Rev. Lett. **54**, 1055 (1985).

5. Deposition Profile of Ammonium Bromide in HBr/N_2 Gas Plasmas for High-Aspect-Ratio Structure

5.1 Introduction

The structure of NAND flash memory has proceeded from a planar type to a three-dimensional (3-D) type to overcome scaling limitations. A typical 3-D NAND flash memory structure consists of alternately stacked multilayers of Si_3N_4 (or polycrystalline-Si) and SiO_2.[1-5] Architectures of 3-D NANDs, such as bit-cost scalable (BiCS) [6-8], vertical-gate (VG) NAND [9-11], and terabit-cell-array transistor (TCAT) [12] offer the potential for a lower bit cost because numerous stacked multi-layers can be etched by using a single deep-etching process. The number of the stacked multi-layers increases with the bit density of 3-D NANDs. Therefore, it is essential to develop a deep, high-aspect-ratio etching technology for multi-layers of Si_3N_4/SiO_2 and poly-Si/SiO_2.

One of the issues for high-aspect-ratio etching of the multi-layers is decreasing the etching rate as the aspect ratio of the holes/trenches increases. That problem is called etch-rate drop. A dominant factor of the etch-rate drop is a decrease in the density of etchant, such as ions and radicals, with an increase in the aspect ratio. Several approaches have been studied to suppress the etch-rate drop.[13] The first approach is to increase the ion energy to compensate for the decrease in the ion flux. The second is to increase the plasma density to increase the flux of the ions and radicals. The third is to decrease the sticking coefficient of the radicals to enhance the transport of the radicals to the bottom of the holes/trenches. The fourth is to control the deposition characteristics to increase the etching efficiency with ion bombardment.

The authors demonstrated controlling the deposition characteristics by using HBr/ fluorocarbon (FC)-based gas chemistries in the microstructure. In our previous work, deep etching with $HBr/N_2/CH_3F$-based gas plasma was successfully demonstrated to fabricate the holes in poly-Si/SiO_2 stacks.[14–24] The vertical and deep hole profile was obtained by a combination of N_2 addition and the adjustment of the substrate temperature to under 20 °C. To understand the mechanism of the deep etching in our $HBr/N_2/CH_3F$-based gas chemistry, the surface composition was analyzed using blanket wafers and pattern samples. X-ray photoelectron spectroscopy analysis indicated that FC-based

deposition is formed on the sidewalls of the holes. The FC-based deposition consists of ammonium bromide (NH_4Br) at a substrate temperature of 20 °C using thermal desorption spectroscopy and time-of-flight secondary ion mass spectrometry analyses.

The NH_4Br can affect the deposition characteristic for high-aspect-ratio etching, as described above. In this study, a formation mechanism of NH_4Br in high-aspect-ratio structure of macro cavities was investigated. In the case where $HBr/N_2/CH_3F$-based gas chemistry is used, the same as the etching condition for the pattern sample, it is supposed to form a deposition that consists of such as FC and NH_4Br in the cavities. However, it is difficult to separate the deposition of mixed materials into the thickness of NH_4Br. Therefore, only N_2/HBr gas chemistry was used for NH_4Br deposition formation to eliminate the influence of FC deposition. The deposition profile of NH_4Br was compared with that of a calculated FC to evaluate how deep the etchant radical flux reaches in micro-hole structures. Furthermore, a model of NH_4Br formation at the surface was proposed to address a mechanism to enable NH_4Br to reach deeply.

5.2 Experimental procedure

In our previous work, HBr/N_2/FC-based gas was used to fabricate the holes in poly-Si/SiO_2 stacks.[14] To remove the contribution of FC gas, the N_2/HBr gas was used to form the NH_4Br deposition in this work. The NH_4Br deposition was formed by plasma in a parallel-plate plasma reactor (shown schematically in Fig. 1). The plasma was generated with a 200-MHz power source and the distribution of plasma was controlled by a magnetic field induced by coils.[25, 26] Process parameters for NH_4Br deposition are shown in Table I. The process pressure was set to 1.0 Pa. The temperature of the sample (set on an electrostatic chuck stage) was maintained at 20°C by using a circulator system.

Gas flow rate (ml/min)			Pressure (Pa)	Source-RF (W)	Wafer-RF (W)	Stage temperature (°C)	Time (s)
HBr	N_2	Ar					
200	50	50	1.0	1000	0	20	600

Table I . Process parameters for NH_4Br deposition.

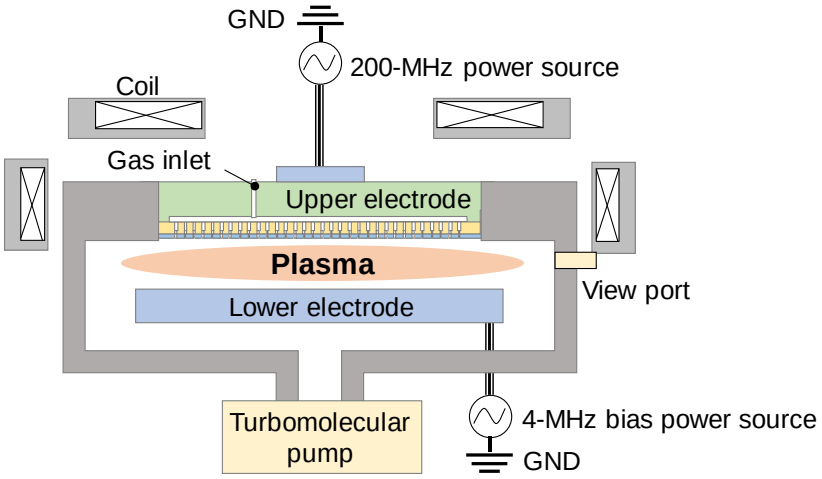

Fig. 1. Schematic of parallel-plate type etching reactor. Reactor uses a 200-MHz power source and 4-MHz bias power source. Gas inlet in upper electrode is made of a dielectric material to withstand corrosive gas.

To investigate the NH_4Br formation (deposition) profile, a macro-cavity structure is used for reproducing micro holes.[27] The macro-cavity method is used for predicting the deposition rate distribution in the vertical micro holes from that in the lateral macro-cavity structure shown in Fig. 2. The cavity consists of a silicon top plate and a spacer with thickness of 0.8 mm on a silicon substrate. The aspect ratio in the cavity is defined as the ratio of the spacer height (w) to the distance from the opening (x). The thickness of the deposition film was measured using SEM. The distribution of the deposition rate in the cavity was evaluated using the dependence of the thickness on the distance from the opening.

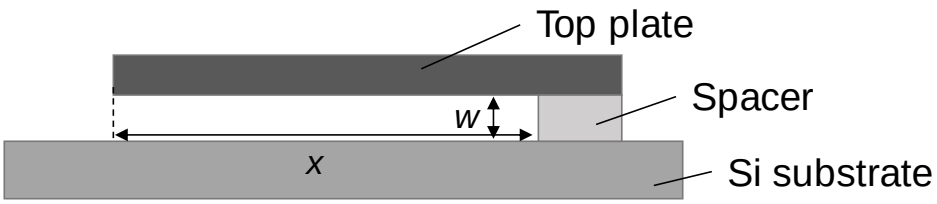

Fig. 2. Schematic of cavity sample consisting of a silicon top plate, spacer, and substrate. Aspect ratio in the cavity is defined as a ratio of spacer height (w) to distance from cavity opening (x).

Figure 3 shows a typical cross-sectional SEM image of a deposition on a silicon substrate in the cavity after N_2/HBr plasma irradiation, from which we obtained the deposition thickness. As shown in Fig. 3, the fluctuation of deposition thickness is within about 10%.

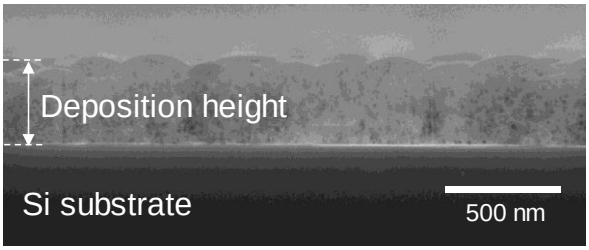

Fig. 3. Typical cross-sectional SEM image of the inside of a cavity on top of a Si substrate after N_2/HBr plasma irradiation.

Generally, the deposition rate distribution ($F(x)$) using the macro-cavity method is represented by the following equations [27]:

$$F(x) = C_1 \mathrm{e}^{ax} + C_2 \mathrm{e}^{-ax} \quad (1)$$

$$a = \sqrt{\frac{S_\mathrm{c} v_\mathrm{t}}{2wD}} \quad (2)$$

where C_1 and C_2 are constants, S_c is the sticking coefficient of radicals, v_t is the thermal velocity of radicals, and D is the diffusion coefficient of radicals. Equations (1) and (2) represent the process in which radicals formed in the gas phase are diffused in the cavity and adsorbed on the silicon substrate with a constant sticking coefficient such as FC deposition. As a result, the deposition rate decays exponentially with the distance from the cavity opening as shown in Eq. (1) in this model.

5.3 Results and discussion

5.3.1 Temperature dependence of ammonium bromide deposition

Figure 4 shows the stage temperature dependence of the NH_4Br deposition rate at the position of 2.0 mm from the opening inside the macro cavity. The deposition rate monotonically decreases with increasing the stage temperature. Generally, ammonium bromide decomposes to ammonia and HBr when heated at elevated temperatures.[28] Furthermore, vapor pressure increases to over 1.0 Pa when the temperature is 50°C by

extrapolation of a previous work.[29] Therefore, decrease of NH4Br deposition rate at elevated temperatures suggests the decompose of the material.

In the macro cavity, there was no deposition on top plate. This indicates that the top plate has a high enough temperature to decrease the deposition rate because the plasma heats up the top plate, which floats thermally. Therefore, it is assumed that NH_4Br reflects without adhering to the top plate in following calculation of the formation model of NH_4Br.

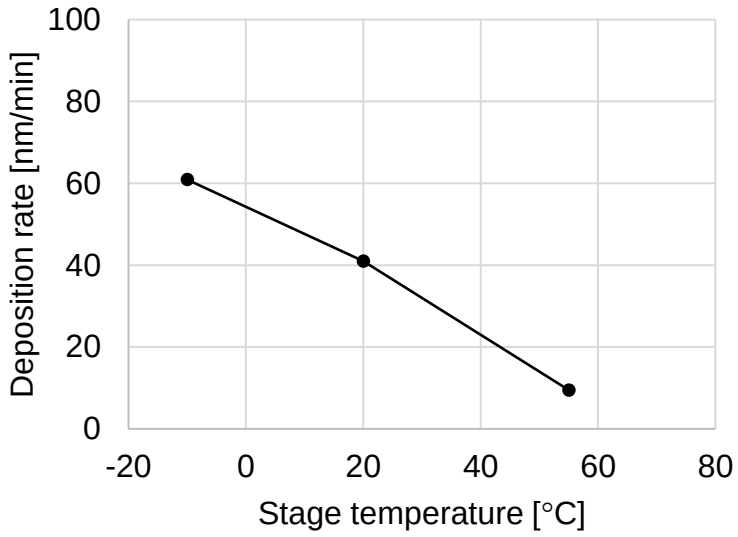

Fig. 4. Dependence of the NH_4Br deposition rate on stage temperature at the position of 2 mm from the opening inside the macro cavity.

5.3.2 Deposition rate distribution in the macro cavity

The NH_4Br deposition rate at a substrate temperature of 20°C on the distance from the cavity opening (x), which is normalized when $x = 0$, is plotted with dots in Fig. 5. The deposition rate decayed as the distance from the cavity opening increased. Because FC gas is widely used for high-aspect-ratio etching, we compared the decay curve of the NH_4Br deposition rate with that of the FC deposition rates formed by CF_2 radicals, which were calculated using Eqs. (1) and (2), to confirm the advantage of NH_4Br.

The solid lines in Fig. 5 show FC deposition rates as functions of x calculated from Eqs. (1) and (2) by assuming sticking coefficients (S_c) of 0.01 and 0.07 for CF_2 because S_c of CF_2 radicals is reported as 0.01–0.07.[28, 29] As a result of comparing the experimental

value of the NH_4Br deposition rate and the theoretical value of the FC deposition rate, the decay of deposition rate is less in NH_4Br than in the case of FCs deposited by CF_2 radical with $S_c = 0.07$. In the case of FCs deposited by CF_2 radical with $S_c = 0.01$, the decay of deposition rate is more in NH_4Br from x = 0–50 mm, however, the decay of the NH_4Br deposition rate is less when $x > 50$ mm.

These results suggest that NH_4Br is transferred more easily than FC even with S_c = 0.01 into a high-aspect-ratio structure over 60 because x = 50 mm corresponds to an aspect ratio of 60 in our cavity structure. A mechanism of the NH_4Br deposition that reaches into a deeper position is discussed in the next section.

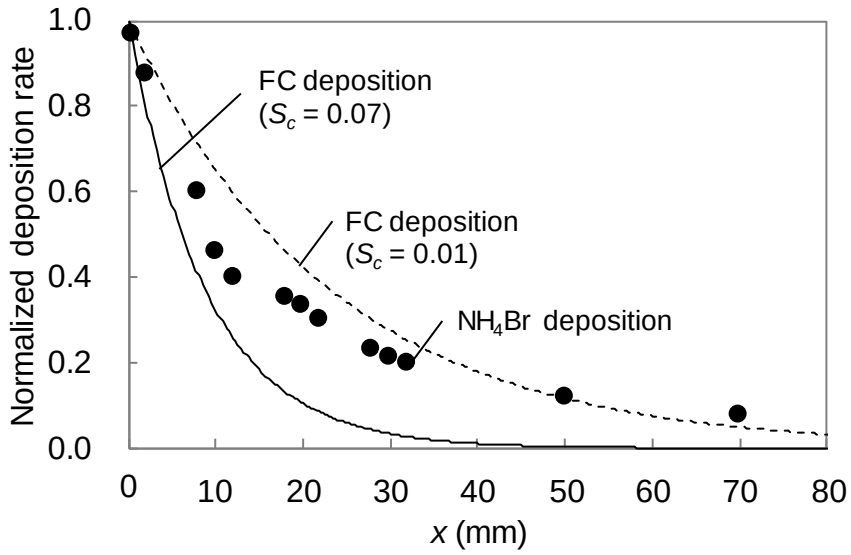

Fig. 5. Relationship between x and deposition rate. Circle dots indicate obtained NH_4Br deposition rate. Solid and dashed lines indicate theoretical FC deposition rate for S_c of 0.01 and 0.07, respectively.

5.3.3 Formation model for ammonium bromide on solid surface

To discuss the formation mechanism of NH_4Br, a deposition model of the NH_4Br is constructed. Considering the gas chemistries, the following dissociation reaction can occur in the plasma.

$$N_2 + e \rightarrow 2N + e \quad (3)$$

$$HBr + e \rightarrow H + Br + e \quad (4)$$

As represented in Eqs. (3) and (4), N_2 and HBr are dissociated into N, H, and Br by

collision with electrons in the plasma. Then, the following reaction is expected to occur with the dissociated radicals and the molecules.

$$N + HBr + 3H \rightarrow NH_4Br \quad (5)$$

As shown in Eq. (5), in the formation reactions of NH_4Br, four radicals and one molecule collide and combine to form a compound. Two possible processes to form the compounds are considered when the reactions in Eqs. (3)–(5) occur. One is the process where NH_4Br formed in the gas phase directly sticks and is deposited in the cavity (model A). The other is that N, H, and HBr are separately transferred into the cavity and encounter each other on the solid surface to form NH_4Br (model B). The models A and B are schematically shown in Fig. 6(a) and (b), respectively.

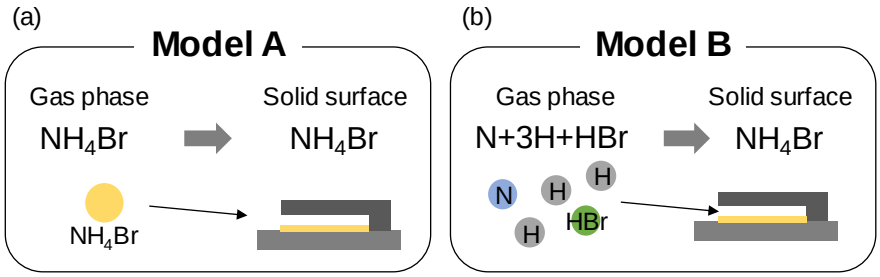

Fig. 6. Model schematics of NH_4Br formation (a) formed in the gas phase and (b) combined on a surface in cavity.

Next, we discuss the dependence of the NH_4Br deposition rate on x in models A and B. The deposition rate of NH_4Br depends on densities of the molecules or radicals at the surface of the substrate, namely, NH_4Br molecule density in model A and a product of the densities of five species (N, 3H, HBr) in model B. The densities are proportional to their concentrations in the gas phase. The deposition rate can be obtained from the dependence of the concentration on x in model A. In the case of model B, we calculated concentrations of the radicals as functions of x with the concentrations at $x = 0$ as initial values, and then we obtained the deposition rate from the product of the calculated concentrations. Considering the reaction rate equation and conservation of mass during the reactions, concentrations of N radicals, H radicals, and HBr molecule dependence on x are represented by the following equations (in which details are described in the appendix section):

$$wD_{\mathrm{N}}\frac{\mathrm{d}^2 n_{\mathrm{N}}}{\mathrm{d}x^2} = Kn_{\mathrm{N}}n_{\mathrm{HBr}}{n_{\mathrm{H}}}^3, \tag{6}$$

$$wD_{\mathrm{HBr}}\frac{\mathrm{d}^2 n_{\mathrm{HBr}}}{\mathrm{d}x^2} = Kn_{\mathrm{N}}n_{\mathrm{HBr}}{n_{\mathrm{H}}}^3, \tag{7}$$

$$wD_{\mathrm{H}}\frac{\mathrm{d}^2 n_{\mathrm{H}}}{\mathrm{d}x^2} = 3Kn_{\mathrm{N}}n_{\mathrm{HBr}}{n_{\mathrm{H}}}^3, \tag{8}$$

where D_{N}, D_{HBr}, and D_{H} denote the diffusion coefficient of N, HBr, and H in Ar gas, respectively, n_{N}, n_{HBr}, and n_{H} denote the concentration of N, HBr, and H in the gas phase, respectively, and K denotes the proportionality constant. Concentrations of radical and molecule dependence on x represented by Eqs. (6)–(8) were derived by assuming the combined total of five species.

Similarly, in the case of model A where NH_4Br deposition is formed on a solid surface by using only NH_4Br molecules, concentration of NH_4Br molecules (n_{NH4Br}) dependence on x is represented by the following equation:

$$wD_{\mathrm{NH_4Br}}\frac{\mathrm{d}^2 n_{\mathrm{NH_4Br}}}{\mathrm{d}x^2} = Kn_{\mathrm{NH_4Br}} \tag{9}$$

where $D_{\mathrm{NH_4Br}}$ denotes the diffusion coefficient of NH_4Br molecules in Ar gas. Equation (9) can be analytically solved, and its solution corresponds to Eqs. (1) and (2). Since the derived Eq. (9) is equivalent to Eq. (1) of model A, it indicates that Eqs. (6)–(8) of model B are an extension of model A shown in Eq. (1). The derived models and the experimental result are compared in the next section.

5.3.4 Comparing NH_4Br formation model with experimental result

The simultaneous partial differential Eqs. (6)–(8) can be solved numerically by the finite element method. For the boundary conditions, n_{N}, n_{HBr}, and n_{H} are given as initial values at the cavity opening, and $\mathrm{d}n_{\mathrm{N}}/\mathrm{d}x = 0$, $\mathrm{d}n_{\mathrm{HBr}}/\mathrm{d}x = 0$, and $\mathrm{d}n_{\mathrm{H}}/\mathrm{d}x = 0$ are given as deviation of concentration at the deepest part of the cavity. The diffusion coefficients which are calculated by referred formulas are set to $D_{\mathrm{N}} = 4.46\ \mathrm{m}^2/\mathrm{s}$, $D_{\mathrm{HBr}} = 1.99\ \mathrm{m}^2/\mathrm{s}$, and $D_{\mathrm{H}} = 19.1\ \mathrm{m}^2/\mathrm{s}$.[32] The initial values of n_{N}, n_{HBr}, and n_{H} are represented by the following equations:

$$n = \frac{p}{k_B T}, \tag{10}$$

$$p_{\mathrm{N}} = P\frac{2\alpha_{\mathrm{N}}[\text{Flow rate of } \mathrm{N_2}]}{[\text{Total flow rate}]}, \tag{11}$$

$$p_{\mathrm{HBr}} = P\frac{(1-\alpha_{\mathrm{H}})[\text{Flow rate of HBr}]}{[\text{Total flow rate}]}, \tag{12}$$

$$p_{\mathrm{H}} = P\frac{\alpha_{\mathrm{H}}[\text{Flow rate of HBr}]}{[\text{Total flow rate}]} \tag{13}$$

where p denotes the partial pressure of each atom and molecule, P denotes the total pressure, k_B denotes Boltzmann constant, T denotes the gas temperature, and α denotes dissociation degree. The α is defined as $\alpha_{\mathrm{N}} = 2\mathrm{N}/(\mathrm{N}_2 + 2\mathrm{N})$ and $\alpha_{\mathrm{H}} = \mathrm{H}/(\mathrm{HBr} + \mathrm{H})$. Considering that the capacitively coupled plasma using in this study have lower dissociation degree in general, α_{N} and α_{H} are assumed to 0.5%.[33, 34] Gas temperature is assumed to 300 K due to low-temperature plasma. By the calculation of Eqs. (10)–(13), initial values of n_{N}, n_{HBr}, and n_{H} are given as $n_{\mathrm{N}} = 4.37 \times 10^{17}\ \mathrm{m}^{-3}$, $n_{\mathrm{HBr}} = 1.75 \times 10^{20}\ \mathrm{m}^{-3}$, and $n_{\mathrm{H}} = 8.62 \times 10^{17}\ \mathrm{m}^{-3}$. The $n_{\mathrm{N}}{n_{\mathrm{HBr}}}{n_{\mathrm{H}}}^3$ dependence on x obtained from Eqs. (6)–(8) represents the distribution of the NH_4Br deposition rate in the cavity.

Figure 7 shows the NH_4Br deposition rate dependence as an experimental result on *x* in the cavity as a dot plot. For the results by Eqs. (6)–(8) for model B, the decay curve of $n_{\mathrm{N}}{n_{\mathrm{HBr}}}{n_{\mathrm{H}}}^3$ was calculated by fitting it with the proportionality constant *K* as a parameter. The decay curve of $n_{\mathrm{N}}{n_{\mathrm{HBr}}}{n_{\mathrm{H}}}^3$ is indicated by the solid line. Comparing model A to B, the decay curve of the NH_4Br deposition rate fitted with S_c as a parameter in Eq. (1) is indicated by a dotted line. When the correlation coefficient R^2 is obtained, $R^2 = 0.85$ in the case of model A, while $R^2 = 0.99$ in the case of model B. As a result, it is confirmed that model B shows a good agreement with the experimental result. In addition, when the process pressure is 1.0 Pa, a collision frequency of radicals of N, H, and Br dissociated by N_2 and HBr is low enough to generate NH_4Br in the gas phase because of their long mean-free path of about 70 mm. Therefore, it is reasonable to state that model B is a formation model of NH_4Br compared with model A.

Model B indicates the importance that the deposition is formed as a compound from radicals and molecules of numerous types to make the deposition rate less likely to decay at deeper positions in the cavity. Furthermore, Eqs. (6)–(8) indicate that the deposition tends to reach a deeper position in the cavity as the proportionality constant *K* correlating to the reaction rate decreases.

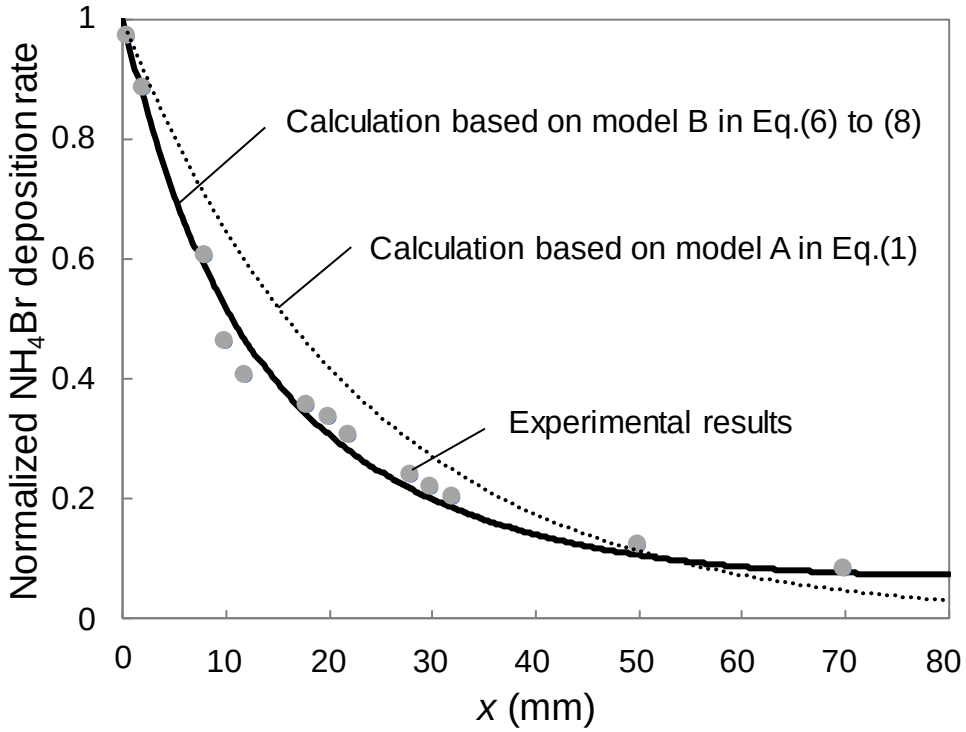

Fig. 7. Relationship between x and normalized NH_4Br deposition rate. Plots are experimental results. Solid line is the result of calculations based on surface reaction formation model in Eqs. (6)–(8). Dashed line is the result of calculations based on conventional model in Eq. (1).

5.4 Conclusion

For the high-aspect-ratio etching process that is a key technology in 3-D NAND fabrication, the deposition profile of NH_4Br that affects etching characteristics was investigated. The deposition profile (rate distribution) was evaluated while deep holes were imitated using a macro-cavity structure to investigate how deeply the NH_4Br formed in etched holes. A pure NH_4Br deposition was formed in the cavity using plasma irradiation with N_2/HBr gas chemistry at a pressure of 1.0 Pa and a substrate temperature of 20°C. In comparison with the theoretical deposition rate distribution of FC film by CF_2 radical (sticking coefficient = 0.01), which is popular in high-aspect-ratio etching, it is revealed that the deposition rate of NH_4Br became larger than that of FC deposition at x > 50 mm, which corresponds to an aspect ratio over 60. To clarify the experiment, two models were investigated; ammonium bromide forms in the gas phase and on a solid

surface, respectively. It was found that the latter model reasonably clarifies the experiment when comparing the two models. These results indicate that NH_4Br sufficiently reaches the bottom of deep holes; thus, NH_4Br is a promising candidate for the etchant in the high-aspect-ratio process.

Appendix

We explain the method for developing Eqs. (6)–(8). In the reaction of Eq. (5), NH_4Br is formed from an HBr molecule, an N radical, and three H radicals dissociated from N_2 and HBr as shown in Eqs. (3) and (4).

From the rate equation, the formation rate of the compound NH_4Br ($\mathrm{d}C_\mathrm{R}/\mathrm{d}t$) from N, 3H, and HBr is represented by the following equation.

$$\frac{\mathrm{d}C_\mathrm{R}}{\mathrm{d}t} = kC_\mathrm{N}C_\mathrm{B}{C_\mathrm{H}}^3, \tag{14}$$

where C_R, C_N, C_B, and C_H denote the surface densities of NH_4Br, N radicals, HBr gas molecules, and H radicals, and k denotes the reaction rate constant.

From a continuity equation, the concentration in the gas phase (n_N) is represented by the following equation.

$$\frac{\partial n_\mathrm{N}}{\partial t} = -\nabla(n_\mathrm{N}\boldsymbol{v}) = \frac{\mathrm{d}}{\mathrm{d}x}(n_\mathrm{N}v_\mathrm{x}) + \frac{\mathrm{d}}{\mathrm{d}y}(n_\mathrm{N}v_\mathrm{y}), \tag{15}$$

where $\boldsymbol{v}$ denotes the velocity of N radicals in the gas phase. Since the cavity thickness (w) is sufficiently small compared with the mean free path, n_N is integrated in the y direction assuming that it is uniform in the y direction and depends only on the x direction. Therefore, Eq. (15) is represented by the following equation.

$$w\frac{\partial n_\mathrm{N}}{\partial t} = wD_\mathrm{N}\frac{\mathrm{d}^2 n_\mathrm{N}}{\mathrm{d}x^2} + \big(\Gamma_\mathrm{y}(w) - \Gamma_\mathrm{y}(0)\big), \tag{16}$$

where Γ_y denotes radical flux in the y direction, and D_N denotes the diffusion coefficient of N radical in Ar gas. The fluxes of the gas that flows onto the surface at thermal velocity (v_th) are represented by the following equations.

$$\Gamma_\mathrm{y}(0) = -v_\mathrm{th}n_\mathrm{N} + \gamma C_\mathrm{N}, \tag{17}$$

$$\Gamma_\mathrm{y}(w) = v_\mathrm{th}n_\mathrm{N} - \gamma C_\mathrm{N}, \tag{18}$$

where γ denotes the rate constant for desorption that is proportional to C_N. Therefore, Eq. (16) is represented by:

$$w\frac{\partial n_\mathrm{N}}{\partial t} = wD_\mathrm{N}\frac{\mathrm{d}^2 n_\mathrm{N}}{\mathrm{d}x^2} + 2(v_\mathrm{th}n_\mathrm{N} - \gamma C_\mathrm{N}). \tag{19}$$

In consideration of adsorption on the surface ($v_{\mathrm{th}} n_{\mathrm{N}}$), desorption ($-\gamma C_{\mathrm{N}}$), and compound formation ($-k C_{\mathrm{N}} C_{\mathrm{B}} {C_{\mathrm{H}}}^3$), the time derivative of C_{N} is represented by:

$$\frac{\mathrm{d}C_{\mathrm{N}}}{\mathrm{d}t} = n_{\mathrm{N}} v_{\mathrm{th}} - \gamma C_{\mathrm{N}} - k \mathrm{C}_{\mathrm{N}} C_{\mathrm{B}} C_{\mathrm{H}}^3. \tag{20}$$

From Eqs. (19) and (20), the following equation is obtained.

$$w \frac{\partial n_{\mathrm{N}}}{\partial t} = w D_{\mathrm{N}} \frac{\mathrm{d}^2 n_{\mathrm{N}}}{\mathrm{d}x^2} - 2 \left(\frac{\mathrm{d}C_{\mathrm{N}}}{\mathrm{d}t} + k \mathrm{C}_{\mathrm{N}} C_{\mathrm{B}} C_{\mathrm{H}}^3 \right) \tag{21}$$

Here, C_{N} at steady state ($\mathrm{d}/\mathrm{d}t = 0$) is represented by the following equation from Eq. (20).

$$C_{\mathrm{N}} = n_{\mathrm{N}} v_{\mathrm{th}} / (\gamma + k C_{\mathrm{B}} C_{\mathrm{H}}^3) \tag{22}$$

If the desorption rate of N radicals into the gas phase is sufficiently larger than the formation rate of NH_4Br, namely, the condition of $\gamma \gg k C_{\mathrm{B}} C_{\mathrm{H}}^3$ is affected, C_{N} is represented by:

$$C_{\mathrm{N}} = \frac{n_{\mathrm{N}} v_{\mathrm{th}}}{\gamma} = K_{\mathrm{N}} n_{\mathrm{N}}, \tag{23}$$

where K_{N} denotes a proportionality constant. Similarly, surface densities of HBr (C_{B}) and H (C_{H}) are represented by:

$$C_{\mathrm{B}} = K_{\mathrm{B}} n_{\mathrm{B}}, \tag{24}$$

$$C_{\mathrm{H}} = K_{\mathrm{H}} n_{\mathrm{H}}, \tag{25}$$

where K_{B} and K_{H} denote a proportionality constant.

Therefore, Eq. (21) at steady state is represented by:

$$0 = w D_{\mathrm{N}} \frac{\mathrm{d}^2 n_{\mathrm{N}}}{\mathrm{d}x^2} - k K_{\mathrm{N}} K_{\mathrm{B}} {K_{\mathrm{H}}}^3 n_{\mathrm{N}} n_{\mathrm{B}} {n_{\mathrm{H}}}^3 = D_{\mathrm{N}} \frac{\mathrm{d}^2 n_{\mathrm{N}}}{\mathrm{d}x^2} - K n_{\mathrm{N}} n_{\mathrm{B}} {n_{\mathrm{H}}}^3, \tag{26}$$

where K denotes the product of k, K_{N}, K_{B}, and K_{H}. By rearranging Eq. (26), the following equation is obtained.

$$w D_{\mathrm{N}} \frac{\mathrm{d}^2 n_{\mathrm{N}}}{\mathrm{d}x^2} = K n_{\mathrm{N}} n_{\mathrm{B}} {n_{\mathrm{H}}}^3 \tag{27}$$

Similarly, the case of HBr molecules and H radicals is represented by the following equations.

$$w D_{\mathrm{B}} \frac{\mathrm{d}^2 n_{\mathrm{B}}}{\mathrm{d}x^2} = K n_{\mathrm{N}} n_{\mathrm{B}} {n_{\mathrm{H}}}^3, \tag{28}$$

$$w D_{\mathrm{H}} \frac{\mathrm{d}^2 n_{\mathrm{H}}}{\mathrm{d}x^2} = 3 K n_{\mathrm{N}} n_{\mathrm{B}} {n_{\mathrm{H}}}^3. \tag{29}$$

References

[1] S. Whang, K. Lee, D. Shin, B. Kim, M. Kim, J. Bin, J. Han, S. Kim, B. Lee, Y. Jung, S. Cho, C. Shin, H. Yoo, S. Choi, K. Hong, S. Aritome, S. Park, and S. Hong, IEDM Tech. Dig., 2010, p. 668.

[2] S. H. Chen, H. T. Lue, Y. H. Shih, C. F. Chen, T. H. Hsu, Y. R. Chen, Y. H. Hsiao, S. C. Huang, K. P. Chang, C. C. Hsieh, G. R. Lee, A. T. H. Chuang, C. W. Hu, C. J. Chiu, L. Y. Lin, H. J. Lee, F. N. Tsai, C. C. Yang, T. Yang, and C. Y. Lu, IEDM Tech. Dig., 2012, p. 21.

[3] A. Goda and K. Parat, IEDM Tech. Dig., 2012, p. 13.

[4] H. Lue, T. Hsu, C. Wu, W. Chen, T. Yeh, K. Chang, C. Hsieh, P. Du, Y. Hsiao, Y. Jiang, G. Lee, R. Lo, Y. Su, C. Huang, S. Lai, L. Liang, C. Chen, M. Hung, C. Hu, C. Chiu, and C. Lu, IEDM Tech. Dig., 2015, p. 44.

[5] K. Parat and C. Dennison, IEDM Tech. Dig., 2015, p. 48.

[6] H. Tanaka, M. Kido, K. Yahashi, M. Oomura, R. Katsumata, M. Kito, Y. Fukuzumi, M. Sato, Y. Nagata, Y. Matsuoka, Y. Iwata, H. Aochi, and A. Nitayama, Symp. VLSI Technol. Dig. Tech. Pap., 2007, p. 14.

[7] Y. Fukuzumi, R. Katsumata, M. Kito, M. Kido, M. Sato, H. Tanaka, Y. Nagata, Y. Matsuoka, Y. Iwata, H. Aochi, and A. Nitayama, IEDM Tech. Dig., 2007, p. 449.

[8] R. Katsumata, M. Kito, Y. Fukuzumi, M. Kido, H. Tanaka, Y. Komori, M. Ishiduki, J. Matsunami, T. Fujiwara, Y. Nagata, Z. Li, Y. Iwata, R. Kirisawa, H. Aochi, and A. Nitayama, Symp. VLSI Technol. Dig. Tech. Pap., 2009, p. 136.

[9] W. Kim, S. Choi, J. Sung, T. Lee, C. Park, H. Ko, J. Jung, I. Yoo, and Y. Park, Symp. VLSI Technol. Dig. Tech. Pap., 2009, p. 188.

[10] H.-T. Lue, T.-H. Hsu, Y.-H. Hsiao, S. P. Hong, M. T. Wu, F. H. Hsu, N. Z. Lien, S.-Y. Wang, J.-Y. Hsieh, L.-W. Yang, T. Yang, K.-C. Chen, K.-Y. Hsieh, and C.-Y. Lu, Symp. VLSI Technol. Dig. Tech. Pap., 2010, p. 131.

[11] C.-P. Chen, H.-T. Lue, K.-P. Chang, Y.-H. Hsiao, C.-C. Hsieh, S.-H. Chen, Y.-H. Shih, K.-Y. Hsieh, T. Yang, K.-C. Chen, and C.-Y. Lu, Symp. VLSI Technol. Dig. Tech. Pap., 2012, p. 91.

[12] J. Jang, H. Kim, W. Cho, H. Cho, J. Kim, S. I. Shim, Y. Jang, J. Jeong, B. Son, D. W. Kim, K. Kim, J. Shim, J. S. Lim, K. Kim, S. Y. Yi, J. Lim, D. Chung, H. Moon, S. Hwang, J. Lee, Y. Son, U. Chung, and W. Lee, Symp. on VLSI Technol. Tech. Dig., pp. 192-193 (2009).

[13] C. M. Huard et al., J. Vac. Sci. Technol. A **35** (5), 05C301 (2017).

[14] T. Iwase, M. Matsui, K. Yokogawa, T. Arase, and M. Mori., Proc. Int. Symp. Dry Process, 2015, p. 47.

[15] T. Iwase, M. Matsui, K. Yokogawa, T. Arase, and M. Mori, Jpn. J. Appl. Phys. **55**, 06HB02 (2016).

[16] T. Iwase, K. Yokogawa, and M. Mori., Proc. Int. Symp. Dry Process, 2016, p. 197.

[17] T. Iwase, K. Yokogawa, and M. Mori., Jpn. J. Appl. Phys. **56**, 06HB04 (2017).

[18] T. Iwase, K. Yokogawa, and M. Mori., Proc. Int. Symp. Dry Process, 2017, p. 209.

[19] T. Iwase, K. Yokogawa, and M. Mori., Jpn. J. Appl. Phys. **57**, 06JC03 (2018).

[20] D. R. Sparks, J. Electrochem. Soc. **139**, 1736 (1992).

[21] J. K. Jung and W. J. Lee, Jpn. J. Appl. Phys. **40**, 1408 (2001).

[22] L. Vallier, J. Foucher, X. Detter, E. Pargon, O. Joubert, G. Cunge, and T. Lill, J. Vac. Sci. Technol. B **21**, 904 (2003).

[23] M. Kim, N. K. Min, S. J. Yun, H. W. Lee, A. M. Efremov, and K. H. Kwon, ETRI J. **30** [3] 383 (2008).

[24] Y. H. Ham, A. Efremov, H. W. Lee, S. J. Yun, N. K. Min, K. Kim, and K. H. Kwon, Jpn. J. Appl. Phys. **49**, 08JB03 (2010).

[25] K. Yokogawa, K. Maeda, H. Kobayashi, T. Kanekiyo, and M. Izawa, Proc. 7th Int. Conf. Microelectronics and Interfaces, 2006, 0940-10.

[26] K. Yokogawa, K. Maeda, and M. Izawa, Jpn. J. Appl. Phys. **47**, 6854 (2008).

[27] K. Watanabe and H Komiyama., J. Electrochem. Soc., 137(4), 1222 (1990).

[28] P. Patnaik, Handbook of Inorganic Chemicals, McGraw-Hill, 2002.

[29] C. L. Yaws, Handbook of Vapor Pressure: Volume 4: Inorganic Compounds and Elements, 1995.

[30] G.S. Oehrlein, H.M. Anderson, and J.L. Cecchi, Final report for the Sept. 1997 - Jan. 2000 period of Contract No. DE-FG02-97ER54445. Fundamental science of high-density fluorocarbon plasmas. United States: N. p., 2001. Web. doi:10.2172/810328.

[31] L. Zheng, L. Ling, X. Hua, G. S. Oehrlein, and E. A. Hudson, J. Vac. Sci. Technol. A, Vol. 23, No. 4, (2005).

[32] R. C. Reid, J. M. Prausnitz, B. E. Poling, The properties of gases and liquids (1987).

[33] N. Kang, F. Gaboriau, S. G. Oh and A. Ricard, Plasma Sources Sci. Technol. 20, 045015 (2011).

[34] A. K. Srivastava, T. Ohashi, and V. M. Donnelly, J. Vac. Sci. Technol. A, 33, 041301 (2015).

6. Conclusion

This dissertation addressed the potential of stacked layer etching for fabricating high-aspect-ratio (HAR) holes by using a plasma containing nitrogen, hydrogen bromide, and fluorocarbon gas aimed at the development of a process for fabricating 3D NAND flash devices.

First, the etching of polycrystalline silicon (poly-Si)/SiO_2 stacks by using a VHF plasma source was studied. One critical goal is achieving both a vertical profile and high throughput for multiple-stack etching. While the conventional process consists of multiple steps for each stacked layer, in this study, HBr/fluorocarbon-based gas chemistry was investigated to achieve a single-step etching process that reduces processing time. Analysis of the dependence of the surface composition on the wafer temperature led to improvement of both the etching profile and rate at low temperatures. The etching mechanism was examined considering the composition of the surface reaction layer. XPS analysis revealed that the adsorption of N-H and Br was enhanced at low temperatures, resulting in a reduced carbon-based-polymer thickness and enhanced Si etching. Finally, a vertical profile was obtained as a result of the formation of a thin and reactive surface reaction layer at a low wafer temperature.

Next, the effects of wafer temperature on the etching rate and surface composition were investigated to clarify the surface reaction mechanism under HBr/N_2/fluorocarbon-based gas plasma. The etching rates of both poly-Si and SiO_2 were found to increase at a wafer temperature of 20°C as compared with those at 60°C. Comparison of the gas combinations of fluorocarbon/N_2 and HBr/N_2 mixtures indicated that the temperature dependence of the SiO_2 etching rate on the HBr to fluorocarbon gas mixing ratio is relevant to the sticking probability of fluorocarbon polymers. To determine the cause of the temperature dependence, the surface composition was evaluated by thermal desorption spectroscopy and laser-sputtered-neutral-mass-spectrometry analyses. Ammonium bromide was identified in the deposition film at a wafer temperature of 20°C. The observed increase in the poly-Si etching rate at lower temperatures was possibly caused by increased amounts of nitrogen, hydrogen, and bromine fixed to the surface by the formation of ammonium bromide.

Then, the reaction mechanism during etching to fabricate deep holes in SiN/SiO_2

stacks using an HBr/N_2/fluorocarbon-based gas plasma was investigated. To etch SiN and SiO_2 films simultaneously, the HBr/fluorocarbon gas mixture ratio was controlled to achieve etching selectivity closest to one. Deep holes were formed in the SiN/SiO_2 stacks by one-step etching at several temperatures. The surface composition of a cross section of the holes was analyzed by time-of-flight secondary ion mass spectrometry. With low-temperature etching, bromine ions (considered to be derived from NH_4Br) were detected throughout the holes. The dependence of the hole depth on the aspect ratio was found to decrease as the substrate temperature decreased, and it became significantly weaker at a temperature of 20 °C. This indicates that the formation of NH_4Br supplies SiN/SiO_2 etchant to the bottom of the holes. This finding will make it possible to alleviate the decrease in the etching rate due to a high aspect ratio.

Next, the deposition profile of ammonium bromide in N_2/HBr plasmas was evaluated as a function of the depth in a macro-cavity structure for the HAR etching process. The macro-cavities reproduce deep holes in 3D NAND structures. The profile was compared with the calculated results for fluorocarbon in CF_2 radicals. The decay in the ammonium bromide deposition was smaller than that of fluorocarbon at depths greater than 50 mm in the cavity. A 50-mm depth corresponds to an aspect ratio of 60. To clarify the results, two models were investigated: ammonium bromide forms in the gas phase and on a solid surface. The latter model clarified the results reasonably well compared with the former model. These results indicate that ammonium bromide sufficiently reaches the bottom of deep holes in 3D NAND HAR structures.

While the major trend in the development of HAR etch technologies is ion-energy enhancement, etchant supply is also an important issue. Its importance will grow along with the development of 3D NAND technology. This dissertation should contribute to the investigation of HAR etching.

List of publications

Original papers

1. **Role of surface-reaction layer in HBr/fluorocarbon-based plasma with nitrogen addition formed by high-aspect-ratio etching of polycrystalline silicon and SiO_2 stacks**

   Jpn. J. Appl Phys. **55** 06HB02 (2016)

   Taku Iwase, Miyako Matsui, Kenetsu Yokogawa, Takao Arase, and Masahito Mori

2. **Effect of temperature on deposition layer formation in HBr/N_2/fluorocarbon-based plasma**

   Jpn. J. Appl Phys. **56** 06HB04 (2017)

   Taku Iwase, Kenetsu Yokogawa, and Masahito Mori

3. **Eliminating dependence of hole depth on aspect ratio by forming ammonium bromide during plasma etching of deep holes in silicon nitride and silicon dioxide**

   Jpn. J. Appl Phys. **57** 06JC03 (2018)

   Taku Iwase, Kenetsu Yokogawa, and Masahito Mori

4. **Deposition profile of ammonium bromide in N_2/HBr plasmas for high-aspect-ratio multilayer etching**

   Jpn. J. Appl Phys. **58** SEEB04 (2019)

   Taku Iwase, Naoyuki Kofuji, Kenetsu Yokogawa, and Masahito Mori

International conferences

1. **Etching Characteristic of Magnetic VHF Plasma for High-Aspect-Ratio Silicon-etch**

   SPIE Advanced Lithography (2015/2/22)

   Taku Iwase, Kenetsu Yokogawa, Takao Arase, Akira Hirata, and Masahito Mori

2. **Role of surface-reaction-layer formed by high-aspect-ratio etching of poly-Si/SiO_2 stacks**

   The 37th International Symposium on Dry Process (2015/11/5)

   Taku Iwase, Miyako Matsui, Kenetsu Yokogawa, Takao Arase, and Masahito Mori

3. **Effect of temperature on mixing layer in HBr/N_2/fluorocarbon-based plasma**

The 38th International Symposium on Dry Process (2016/11/21)

Taku Iwase, Kenetsu Yokogawa, and Masahito Mori

4. **Direct composition analysis using TOF-SIMS for the surface of deep etched hole in SiN/SiO_2 stacks**

   The 39th International Symposium on Dry Process (2017/11/16)

   Taku Iwase, Kenetsu Yokogawa, and Masahito Mori

5. **Deposition Profile of Ammonium Bromide in High-Aspect-Ratio Structure for Multilayer Etching**

   The 40th International Symposium on Dry Process (2018/11/13)

   Taku Iwase, Kenetsu Yokogawa, and Masahito Mori

6. **High Aspect Ratio Etching**

   The 40th International Symposium on Dry Process (2018/11/13)

   Taku Iwase

Domestic conferences (in Japanese)

1. **高アスペクトシリコン加工に対応した有磁場 VHF プラズマのエッチング特性**

   第 75 回応用物理学会秋季学術講演会（2014/9/19）

   岩瀬 拓、森本 忠雄、横川 賢悦、荒瀬 高男、平田 昭、森 政士

2. **多結晶 Si/SiO_2 多層膜の高アスペクト比加工における表面反応層の役割**

   第 189 回応用物理学会シリコンテクノロジー分科会研究会（2016/2/19）

   岩瀬 拓、松井　都、横川 賢悦、荒瀬 高男、森 政士

3. **SiN/SiO_2 積層深孔加工におけるパターン内壁の表面組成解析**

   第 78 回応用物理学会秋季学術講演会（2017/09/07）

   岩瀬 拓、唐橋 一浩、浜口 智志

4. **積層膜加工に向けた高アスペクト構造内の臭化アンモニウムの堆積分布の解析**

   第 206 回応用物理学会 Si テクノロジー分科会研究集会（2019/2/8）

   岩瀬 拓、小藤　直行、横川 賢悦、森 政士

Acknowledgments

The author, Taku Iwase, wishes to express his deep gratitude to Professor Satoshi Hamaguchi from the Center for Atomic and Molecular Technologies, Osaka University for his instructive guidance and encouragement throughout the present work. The author would like to thank Professor Kazuhiro Karahashi from the Center for Atomic and Molecular Technologies, Osaka University for his insightful comments and suggestions. The author would also like to thank Professor Manabu Tanaka and Professor Ryoichi Nakatani from Osaka University for chairing his dissertation committee.

The author would like to thank Dr. Takeharu Ishikawa, Mr. Takahiro Kashiwagi, Mr. Satoru Nagashima, Mr. Tomoyuki Yamashita, Mr. Jun Nakagawa, and Mr. Katsumi Endo from Toyama Co., Ltd. for providing the TOF-SIMS data. The author wishes to thank Dr. Miyako Matsui from the Research & Development Group, Hitachi, Ltd. for providing the XPS measurement support. The author is deeply grateful to Dr. Naoyuki Kofuji and Dr. Katsuya Miura from the Research & Development Group, Hitachi, Ltd. for their constructive suggestions and extensive discussion. The author thanks Dr. Masaru Kurihara, Dr. Hirotaka Hamamura, and Dr. Takeshi Ohmori from the Research & Development Group, Hitachi, Ltd. for the generous support and encouragement.

The author would like to express gratitude to Mr. Kenetsu Yokogawa, Dr. Masahito Mori, Mr. Takao Arase, Mr. Hayato Watanabe, Mr. Satoshi Terakura, Mr. Shinichi Isozaki, Mr. Takahisa Hashimoto, Mr. Shinya Kawamura, Mr. Akira Hirata, Mr. Yusuke Takegawa, Mr. Hiroyuki Kajifusa, Mr. Tomohiro Takamatsu, and Mr. Tsutomu Iida from the Electronic Device Systems Business Group, Hitachi High-Technologies Corp. for their tremendous support on the experiment. The author wishes to thank Dr. Tomoko Ito from Osaka University and Dr. Hu Li from Tokyo Electron Technology Solutions, Ltd. for their support on the experiment as well. The author thanks Professor Kenji Ishikawa from Nagoya University for the wide-ranging discussion in the introduction section. The author thanks Mr. Mitsuhiro Omura from the Advanced Memory Development Center, Toshiba Memory Corporation for the in-depth discussion on high-aspect-ratio etching.

Finally, I would like to express the deepest appreciation to my family, Mrs. Masako Iwase and Subaru Iwase, for their continuing moral support.

Taku Iwase

July 2019